An Optical Vortex Coherence Filter

by

David Palacios

A Dissertation

Submitted to the Faculty

of the

Worcester Polytechnic Institute

in partial fulfillment of the requirements

for the degree

of

Doctor of Philosophy

in

Physics

by

_____

June 9st, 2004

APPROVED:

_____
Dr. Grover A. Swartzlander Jr., Dissertation Advisor

_____
Dr. Thomas Keil, Committee Member

_____
Dr. Rick Quimby, Committee Member

Abstract

Optical vortices are ubiquitous features of electromagnetic radiation that are often described as a destructive null in a beam of coherent light. Optical vortices may be created by a variety of different methods, one of which is by the use of a diffractive vortex mask, which is a plate of glass that has been etched in a spiral staircase pattern such that the thickness of the mask varies harmonically in the azimuthal direction. Light passing through the mask gains an azimuthal variation in phase due to the index mismatch between the glass substrate and the surrounding medium and thus an optical vortex is created.

There is an implicit assumption that the light is spatially coherent, or in other words, that there is a definite phase relationship between each point in the beam. Optical vortices are not believed to occur in completely incoherent light where the term "phase" no longer holds any meaning. Optical vortices are also poorly understood in partially coherent light where statistics must be used to quantify the phase. The purpose of the research presented in this thesis was to determine how spatial coherence affects the transmission properties of the vortex phase mask.

This research enabled us to create a coherence filtering technique based upon the vortex diffractive mask. In this dissertation I will demonstrate the usefulness of this filtering technique in two specific applications. First in the detection of forward-scattered light, where the un-scattered probe beam may blind a detector making detection of the scattered light extremely difficult. Second, in the enhanced resolution of two nearby

objects, where the signal from one object may be lost in the glare of a brighter

companion. This filtering technique has a wide field of possible applications including

the detection of extra-solar planets, the detection of defects in laser optics, and improved

methods in optical tomography.

In loving memory

of

Knight

(July 4th 1998-May 19th 2004)

He was my best friend during my graduate school experience.

Without his unconditional love this dissertation would never have been possible.

He will be sorely missed and remembered fondly

Acknowledgements

I'd like to thank my dissertation advisor Prof. Grover Swartzlander Jr. whose direction and dedication to perfection helped mold me into the scientist that I am today. He was patient when I struggled and firm when I was lax and for that I thank him considerably. I also thank Prof. Tom Keil and Prof. Rick Quimby for taking the time to read my dissertation and make helpful suggestions.

I would also like to thank a few of the mentors throughout my career, which have helped me grow as a scientist. I'd like to thank Prof. Ryne P. Raffaelle for allowing me to perform research at an undergraduate level in his laboratory. I'd like to thank the Physics Department at the Florida Institute of Technology for inspiring me to learn more. I'd like to thank Prof. George Phillies for advising my GAAN fellowship and providing invaluable advice. I'd like to thank the Physics Department at The Worcester Polytechnic Institute for all its help and understanding through the years. I also thank the Optical Sciences Department at the University of Arizona, for providing a positive research environment where I could excel. I'd like to give special thank to Prof. Arvind Marathay for engaging in many helpful conversations on Coherence Theory.

Contents

Contents

Contents

List of Figures

List of Figures

Chapter 7

Appendix A

Appendix B

Symbols and Abbreviations

DOE   Diffractive optical element

OV   Optical vortex

OVCF   Optical vortex coherence filter

MCF   The mutual coherence function

MSDF   The mutual spectral density function

(x,y) Cartesian transverse coordinates

(x',y') Propagated Cartesian transverse coordinates

(ϕ,r) Cylindrical transverse coordinates

(f_x,f_y) Transverse spatial frequency coordinates

$E()$ The electric field

$A()$ The amplitude of the electric

$\Gamma()$ The mutual coherence function

$\gamma()$ The normalized mutual coherence function

$\chi()$ The cross-correlation function

$P_s()$ The phase function

$f()$ The scattering amplitude

$\Theta()$ The phase of an electromagnetic field

$I()$ The intensity of an electromagnetic field

$Gauss(x,y)$ Gaussian window function

Symbols and Abbreviations

Hann(x,y)	Hanning window function
Rect(x,y)	Rectangular bandpass filter function
Cyl(r)	Cylindrical bandpass filter function
i	$\sqrt{-1}$
()*	Complex conjugate
||	The absolute value
< >	The time average
Re{}	The real part of {}
Im{}	The imaginary part of {}
FT{}	The 2-D Fourier transform
FT^{-1}{}	The inverse 2-D Fourier transform
z	The propagation distance
t	time
τ	time difference
m	The topological charge
$\nabla\phi$	The gradient of the phase
L_c	The transverse coherence length
A_c	The coherence area
k	The wave number
λ	The wavelength of light
λ_0	The wavelength for which a DOE is intended

Symbols and Abbreviations

$\Delta\lambda$	The wavelength mismatch between the wavelength incident on an OVCF and λ_0
Δm	The additional topological charge formed from an OVCF due to $\Delta\lambda$
ω	The angular frequency of a monochromatic beam of light
ν	The temporal frequency of a monochromatic beam of light
w	The 1/e waist size of a Gaussian beam
w_0	The initial waist size of a Gaussian beam
w_v	The vortex core size
β	The ratio of the beam size to the vortex core size
β_{FF}	The far-field value of β
β_0	The value of β at the output of a vortex DOE
d	DOE glass thickness
d_0	The nominal DOE glass thickness
n_s	The refractive index of a DOE
n_0	The index of refraction of the medium surrounding a DOE
z_R	The Rayleigh diffraction length
z_v	The characteristic decay length of β
Λ	The fringe spacing
f_0	The carrier frequency
w_c	The characteristic cutoff size of a window function
f_c	The characteristic cutoff frequency of a bandpass filter
N	The number of steps in a vortex DOE

Symbols and Abbreviations

f	Lens focal length
D	Lens diameter
R_{ap}	The radial aperture size
δP	The power transmitted through an OVCF
P_{tot}	The total beam power incident on an OVCF
r_0	The initial radial position of the fractional vortex at the output of the vortex DOE
ρ	Concentration of scattering particles
ρ_0	The scattering extinction parameter
θ	The scattering angle
θ_d	The diffraction angle
α	Two source separation angle
b	The impact parameter
σ_{sca}	The scattering cross-section
σ_{abs}	The absorption cross-section
σ_{tot}	The total cross-section

1. Introduction

Vortices are a fascinating feature of waves that are found throughout nature. They are known to occur in quantum systems, such as super-fluid helium, superconductivity, and Bose-Einstein condensation [1]. They are also readily identified as whirlpools, hurricanes and tornadoes in classical fluids [2,3]. In systems where a wave description is applicable, the space-time evolution of a wave is governed by its phase front topology. A wave having a helical phase front may be called a "vortex wave" owing to the circulation of momentum around the helix axis [2].

In optics, vortices are characterized by a dark core of destructive interference in a beam of coherent light. The last decade has seen a resurgence of interest in optical vortices [4], owing in part to new potential applications. Optical vortices have been used to enhance laser trapping of low index particles [5], and laser tweezing of biological samples [6,7]. In nonlinear optical systems, optical vortices may induce a waveguide [8], which may be useful as an optical switching technique. Optical vortices have also sparked interest in quantum computing due to their unique wavefront topology [9].

In this thesis we will present a new application of an optical vortex: an optical vortex coherence filter. Vortex waves are known to occur in coherent systems having a well-defined phase, but are ill defined in partially coherent systems where statistics are required to quantify the phase. In the incoherent limit neither the helical phase nor the characteristic "eye" in the intensity profile is observable. This allows us to use an optical vortex to eliminate the coherent light so that incoherent light may be detected.

This thesis covers two main topics: (1) The properties of a partially coherent vortex field and (2) the coherence filtering properties of an optical vortex. There are several methods to embed an optical vortex onto a background beam. These methods include mode-converters [10], computer generated holograms [11-13], and diffractive optical elements [14,15]. In the work presented here we will only describe the use of a diffractive optical element, as it is most pertinent to our coherence filtering technique. Using experimental, numerical, and analytic methods we investigate how an optical vortex field is affected by spatial coherence and also, how we may utilize this in a coherence-filtering scheme.

The chapters in this thesis are organized as follows. A brief history of optical vortices is given with a literature overview in Chapter 2. The creation of an optical vortex by a diffractive optical element is described in Chapter 3. The coherence nulling properties of an optical vortex are discussed in Chapter 4, demonstrating that an optical vortex can null coherent light including polychromatic light for a wide field of applications. The spatial coherence properties of a vortex field are described in Chapter 5, as well as the first experimental observation of a vortex induced correlation singularity. The detection of forward scattered light by a vortex coherence filter is demonstrated in Chapter 6, showing the usefulness of the technique. Finally, the resolution of two nearby objects is explored in Chapter 7, opening the way to new applications in astronomy.

Parts of this thesis contributed to the patent:

Optical Vortex Spatial Filter for Coherent and Incoherent Detection of Electromagnetic Radiation, by Grover A. Swartzlander Jr. and David Palacios, provisional patent application submitted on April 12, 2002.

Also parts of this thesis have been published in or submitted to the following journals:

1. Spatial Correlation Singularity of a Vortex Field, by D.M. Palacios, I.M. Maleev, A.S. Marathay, and G.A. Swartzlander Jr., submitted to Physical Review Letters 10/13/03

2. Observed Scattering into a Dark Optical Vortex Core, by David Palacios, David Rozas, and Grover A. Swartzlander Jr., Phys. Rev. Lett. vol. 88, #10, article # 103902 (2002).

and were presented at the following international conferences:

1. " Optical Vortices in Low Coherence Light" presented at:

    The Optical Society of America Annual Meeting (October 2003)

2. " White Light Optical Vortices" presented at:

The Optical Society of America Annual Meeting (October 2002)

3. "Optical Vortex Diffractive Optical Element-Scattering Application" presented at:

   The Diffractive Optics and Micro-Optics Topical Meeting (June 2002)

4. " Scattering into Darkness" presented at:

   The OSC Industrial Affiliates Workshop (February 2002)

5. " Optical Vortex Detection of Forward-Scattered Light" presented at:

   The Optical Society of America Annual Meeting (October 2001)

6. " An Optical Vortex Spatial Filter" presented at:

   Conference on Lasers and Electro-Optics (May 2001)

2. History

Vortices are a ubiquitous feature of nature that have inspired both admiration and fear from humans since the dawn of time. They appear in early cave drawings where the spiral was used as a symbol for infinity [16]. They also appear in the early mythology of the Greeks, when Odysseus must charter a careful course between the jaws of Scylla and the icy depths of the whirlpool Charybdis in order to find his way home [17]. Although mankind has wondered what secrets may lie inside the "eye" of a vortex since time in memorable, only in recent history have we begun to unravel the mystery of these curious objects.

Vortices appear throughout such diverse fields as fluids, meteorology, cosmology, optics, and quantum mechanics. In fluids, vortices may appear as whirlpools [2], contrails [18], or smoke rings [19]. In meteorology, vortices are easily recognized by the destructive power they unleash in the form of hurricanes and tornadoes [3]. In cosmology, the familiar spiral of our own galaxy is a vortex [20-23]. Also, like the "eye" of a hurricane it is now believed a gravitational singularity, known as a black hole, may exist at the heart of nearly all spiral galaxies [24, 25]. In quantum mechanics they are known to form in Bose-Einstein condensates, superfluids, and superconductors [1]. In optics, they are described as a dark null of destructive interference where the real and imaginary parts of the field are identically zero [4]. The phase around these singular points is spiral shaped and thus, they are called optical vortices [26].

An optical vortex is essentially a phase object and may be described by a phase profile given by:

$$\Theta(r,\phi,z) = m\phi \qquad (2.1)$$

where (r, ϕ, z) are the cylindrical coordinates centered on the vortex, and m is a signed integer known as the topological charge. The topological charge of a defect may be found from the line integral [26]:

$$m = (1/2\pi)\oint \nabla\phi ds \qquad (2.2)$$

where $\nabla\phi$ is the gradient of the phase and ds is a line enclosing the defect. In a single revolution about the vortex core the phase increases by an integer multiple of 2π, and therefore the phase is continuous for all paths that do not cross r=0. At the center of the vortex (r=0) the phase is singular because it has no defined value; this is physically acceptable since the amplitude of the field is zero at this point. An optical vortex is also known as a screw type dislocation since a field with a phase given by Eq.(2.1) would form helical phase fronts as it propagates much like the bore of a screw [27].

Optical vortices were first observed in cylindrically symmetric systems. The familiar TEM*01"doughnut" mode of a laser cavity is an example of an optical vortex [28]. The doughnut mode contains the characteristic dark core of an optical vortex, which has a diameter that is dependent on the wavelength and the diameter of the resonator cavity. This type of vortex does not change its shape as it propagates and therefore is an auto-normal solution to the wave equation. The Laguerre-Gaussian modes [29] are an ortho-normal set of solutions to the wave equation in cylindrical coordinates that may be used to describe optical vortices [30].

Optical vortices are also known to occur spontaneously in resonator cavities. In large area resonator cavities a rich variety of OV patterns have been postulated as well as observed [31-39]. The spontaneous creation and annihilation of OVs as well as the propagation of OV modes have been studied extensively for various resonator cavities [40-46]. In addition, the formation of self-organizing patterns, spatial symmetry breaking, and multi-stable solitons have also been examined in laser cavities [47-51].

Unlike the symmetric systems described above, optical vortices may also occur naturally in unbounded systems. In 1974, Nye and Berry showed in a landmark paper [27] that a wave pulse reflected from a rough surface may contain phase defects which are similar to the ones found in imperfect crystals. By comparing successive optical wavefronts in a similar fashion to successive layers in a crystal, they found that these phase defects take the form of edge, screw, or mixed edge-screw dislocations [52]. It should be emphasized that these findings apply to any coherent wave trains that propagate in different directions and interfere. As a consequence, all that is necessary to create an optical vortex is the interference of three waves [53].

When light scatters from a rough surface a random speckle pattern may form. Zeldo'vich demonstrated that in any given patch of laser speckle there is a finite probability that an optical vortex will be present [54, 55]. He also showed that the formation of higher charged vortices is improbable in speckle fields [56]. In addition to the advances made by Zeldo'vich, Freund et al. predicted that a random Gaussian distribution of optical vortices in speckle may demonstrate unexpected topology

correlations and sign rules [57-70].   By assuming a physical system[1], Freund was able to

prove the "sign principle", which states that there is a high probability that the near

neighbor vortices having opposite charge [60]. He also demonstrated that correlations

exist between numerous near neighbor parameters besides the topological charge,

suggesting the presence of an underlying order to an apparently random wave field

[62-70].

Optical vortices may also occur in nonlinear systems. The spontaneous birth of

OVs from a Gaussian lens effect, were demonstrate in several nonlinear media [71-75].

An initially smooth Gaussian beam of sufficiently high intensity creates a change in the

index of refraction of the nonlinear material inducing a Gaussian lens. The Gaussian

shape of the lens creates aberrations because light from the center of the beam is

defocused away from the center while light at the periphery of the beam is focused

towards the center. Upon propagation the creation and annihilation of vortices may be

observed. Similarly, optical vortices may be created by a cusp diffraction catastrophe

[76]. Where an elliptically shaped beam is transmitted through a nonlinear material. At

the point of a cusp diffraction catastrophe a quadrupole vortex forms [77].

In nonlinear systems, an optical vortex may also form a soliton [78-95].

Swartzlander and Law [78] were the first to experimentally observe an optical vortex

soliton. Meanwhile, Snyder discussed the possibility of self-guided dark nonlinear

modes based on a waveguide analogy [8]. An OV soliton is a (2+1) dimensional robust

---

[1] A physical optical system being one where the wave is single valued at any point in
space.

spatial structure, which propagates without changing its size. They may form in a self-defocusing medium when the effects of diffraction are balanced with the nonlinear refractive index change. OV solitons have been observed in thermal, Kerr, and quadratic nonlinear media. Also the creation, annihilation, and propagation of OV solitons in these media have been extensively examined.

In the OV fields described above the physical parameters associated with the vortex could not be easily controlled. For instance optical vortices either spontaneously appear at random locations or a single vortex appeared at the center of the cavity. In order to understand the physical nature of an OV, we must be able to control the physical parameters that affect the vortex.

An OV may be created in a controlled manor by a variety of different methods. One method is by use of an astigmatic mode converter [10], which converts a Hermitte-Gaussian (HG_{0l}) mode into a Laguerre-Gaussian (LG_{0l}) mode. The LG_{0l} beams are optical vortices with an integer topological charge, $m=l$ [29,30]. An astigmatic mode converter consists of two cylindrical lenses in a spatial filtering configuration which focuses light along only one direction. For convenience we will say the lenses are aligned to focus the light along the x-axis but not along the y-axis. The HG_{0l} beam is then rotated with respect to the z-axis by 45°. With this arrangement the HG_{0l} beam will be converted to an LG_{0l} beam by making use of the 1D Gouy phase shift imparted on the beam as it passes through the focus of the first lens [96, 97]. Unfortunately this method does not allow the user to control the size or shape of the vortex, nor does it allow for control over the number or arrangements of vortices in the beam.

Bazhenov introduced the use of holograms as a more versatile method of vortex creation [11]. An OV hologram may be created by interfering a reference beam with a vortex beam. Vortex holograms have been created using both spherical [11] and plane wave reference beams [12,13]. In the case of a spherical reference beam, a spiral pattern forms in the hologram and the OV is created at the tip of the spiral. When a plane wave reference is used, a forking pattern instead occurs in the hologram and the vortex is created near the tip of the forking fringes. This gave experimenters the ability to control the size, shape, number and arrangement of optical vortices in a laser beam.

An optical vortex may also be created by a diffractive optical element (DOE) [14,15] as well, which we will discuss in greater detail in chapter 3. An optical vortex DOE consists of a plate of glass that is etched in a spiral pattern, such that the thickness of the plate increases in the azimuthal direction. Light transmitted through the glass plate will gain an azimuthal phase variation, which may approximate the screw shaped wavefronts with a phase described by Eq. (2.2). This method, although more expensive than a computer generated hologram, allows the same functionality of a vortex hologram but is also well suited to high powered applications where a hologram may be damaged.

When methods were developed to control the physical parameters that affect an OV, a rich variety of vortex dynamics could be studied. The propagation dynamics of single, dipole, and quadrupole vortices were studied [98-109]. In addition, the propagation of vortex arrays [98, 105] and lattices [109] were also studied. In the works of Roux [98], Idebetouw [101], Rozas [107, 108], it was shown that the shape of the vortex core plays a strong role in the propagation dynamics of an array of vortices.

Optical vortices may be split into two families based upon the amplitude function, which describes the shape of the core region. Optical vortices may be either large core or small core vortices.

Large core vortices, like the doughnut mode of a laser cavity, are auto-normal functions that do not change their shape as they propagate. As a consequence, the ratio of the vortex core size to the beam size remains constant upon propagation. Indebetouw [101] derived closed-form analytic solutions describing the propagation of an arbitrary number of large core vortices embedded in a Gaussian background beam. According to his solutions only vortices of opposite charge will affect each other's propagation dynamics. He found that an array of large core vortices with the same charge will rigidly rotate do to the phase evolution of the background beam. However, neither the presence nor the position of the vortices in the array affected each other's propagation dynamics. He also showed that in the far field the angular displacement of the rotating array of vortices asymptotically approached the Gouy phase shift of 90 degrees [96, 97].

In contrast, small-core vortices, or vortex filaments, may be made arbitrarily small compared to the background beam. Roux [98] and Rozas [99, 107, 108] predicted that small core vortices may exhibit fluid like rotation similar to vortices in liquids. Rozas predicted that a pair of small core optical vortices of the same charge could rotate at a rate proportional to the inverse square of the distance between them [107]. However, these high rotation rates between pairs of small-core vortices could not be sustained upon propagation because the cores of each vortex diffract and overlap. Therefore, in linear media, you will obtain the same results for small core vortices that you would for large

core vortices. Rozas was able to experimentally verify his claims by examining the

rotation of a pair of small core vortices in a nonlinear media [108]. By creating two small

cored OV solitons, he was able to eliminate diffraction and observe the fluid-like rotation

effect.

An OV also carries orbital angular momentum proportional to the topological

charge of the vortex [10, 109-112]. The angular momentum of an OV beam was first

measured by Beijersbergen [10,109]. He measured the rotation of a cylindrical lens

suspended by a fine wire when a vortex is created. In the experiment the cylindrical lens

was part of an astigmatic mode converter used to create an OV as we described above.

The HG_{01} mode transmitted through the mode converter contains no orbital angular

momentum and thus when its converted to a LG_{01} beam, which does contain orbital

angular momentum, the beam lens is rotated to conserve the momentum of the system.

The addition of orbital angular momentum has been explored extensively [11, 110]. Also

the conservation of angular momentum in nonlinear processes has been explored [111].

Recently the spatial distribution of the angular momentum in an OV beam has also been

examined [112].

Up to this point, we have discussed several of the properties of an optical vortex

and how they may be created but we have not discussed how we can detect an OV.

Theoretically, OVs may be located by finding the points where the real and imaginary

parts of the field are simultaneously zero [27]. However this isn't very practical since we

can only directly measure the real part of the field experimentally. Interferometry is a

more practical method for measuring a phase object such as an optical vortex [4]. When

two coherent beams interfere bright and dark fringes occur. The phase structure of the

two beams affects the shape of those fringes. In most interferometric measurement

techniques an object beam contains the phase information we wish to measure, in our

case an optical vortex, and a planar or spherical reference wave is used for comparison.

If the reference wave is curved a spiral will be seen in the circular interference fringes

with the tip of the spiral pointing at the vortex center. If a plane wave reference beam is

used, the vortex will be located at a forking fringe. In the next chapter we will describe

in detail how we may use an interferometer to accurately reproduce the phase profile of a

vortex beam. Although interferometry is the most common technique, several other

methods have been explored using polarization phase maps and sorting methods based on

the angular momentum of the beam.

Optical vortices have been found several applications throughout the years. One

property of an OV that may be exploited for applications is the ability to use an OV

soliton to induce a waveguide [8, 113]. In a self-defocusing nonlinear medium, the low

intensity in the core region of an OV soliton will change the index of refraction very

little. However, if the bright ring surrounding the vortex core is sufficiently intense, a

nonlinear refractive index change can reduce the index of refraction of the surrounding

medium. Thereby inducing a core region with a high index of refraction surrounded by a

cladding region with a low index of refraction. This may find applications in all optical

switching, where it is desirable to control light with light. This effect has been explored

theoretically as well as experimentally [8, 113]. This property was also employed to

create an optical transistor [95], where the intensity of a probe beam could be successfully controlled by the intensity of a pump beam.

Optical vortices have also been explored for use in optical trapping experiments, where small objects may be trapped and manipulated by a focused laser beam. The orbital angular momentum of an OV may be used to increase the trapping efficiency of an optical trap and may also be used to rotate a trapped particle [114]. Optical traps without an OV can only trap particles that have a higher index of refraction than the surrounding material, however, an OV allows one to trap low index particles as well [5]. Gahagan demonstrated the trapping of both high index and low index particles separately and simultaneously by an OV trap [114]. Furthermore, the low intensity core of an OV decreases the damage imparted on a biological sample that is trapped in a focused laser beam [6,7]. This may allow optical traps to find a greater range of use in biological experiments. Recently, Dholokia has explored the use of non-diffracting Bessel beams, which contain an optical vortex at the beam center, as a new type of optical trap [115, 116]. In this type of trap, not only will a particle rotate about its axis as discussed earlier, but also the particle can be made to orbit the center of the beam.

Optical vortices have also been examined for use in optical computing [9]. The topology of OVs may be used to perform mathematical operations. Two OVs with unity topological charge may be added to form a charge two OV and two oppositely charged vortices may be added to obtain zero topological charge. Optical vortices have been explored in composite beams where the phase delay between the two beams may be used to control the number and position of vortices in the composite field [117, 118]. This

may find applications in optical steering techniques, where one may wish to switch a signal between several output ports.

In current research, the presence of vorticity in partially coherent light is being investigated. There are two types of coherence referred to in the literature, spatial and temporal. Temporal coherence refers to how well correlated a single point in a wavefront is at two different times and spatial coherence refers to how uniform the wavefront of a beam of light is at a given instance of time. Coherence theory has its own rich history, which for the sake of brevity, we will not expound upon here. However, a thorough treatment of coherence theory is presented in Appendix A for the interested reader.

Several methods have been introduced recently to explore the formation of vortices in partially coherent systems. One method, called the modal theory of coherence [119], treats a partially coherent beam as an incoherent superposition of coherent modes. Such a method may be used to construct a partially coherent beam containing OVs from the superposition of Laguerre-Gaussian modes or helicoidal modes [120-122]. Partially coherent OV beams have also been explored with a twisted Gaussian-Schell model source [124]. Non-diffracting beams and Bessel correlated beams may also carry optical vortex modes [125- 127]. More recently it has been demonstrated that partially coherent beams may be constructed with a separable phase and such beams may contain phase dislocations [121, 128].

Another method to explore the properties of OVs in partially coherent light is to examine the mutual coherence function (MCF) as we did in this dissertation (see appendix A). The MCF is complex function that can be propagated from an initial plane,

which may contain an OV, to a detection plane of interest. In early works, Wolf et al demonstrated that the MCF itself could contain phase dislocations [129]. Recently, Palacios et al. demonstrated that an OV could induce new types of spatial correlation singularities in a partially coherent beam [130]. Concurrently, spatial correlation vortices were theoretically predicted by Gbur [131, 134] and experimentally measured by Maleev et al [133-135].

In the meantime temporal correlation effects were also being investigated. Gbur predicted that a focused polychromatic beam would exhibit an anomalous spectral effect near a singularity in the focal plane [136, 137]. Popescu used a fiber probe to measure the spectral changes near a singularity in a focused polychromatic beam and was able to experimentally verify the predictions of Gbur [138]. Swartzlander et al. explored the formation of temporal correlation vortices by means of a Fizeau interferometer and he was able to demonstrate they exhibit topological dispersion [139].

These new singularities are not real objects per se because they exist as a feature of the correlation between various points in the beam, however their presence may still affect the properties of the host beam. The coherence properties of an OV have also led to new applications. Swartzlander predicted [140] and Palacios et al. [141] demonstrated that an optical vortex may be used as a filter to detect forward-scattered light. The coherence filtering properties of an OV is the central interest of this dissertation. The exploration of the coherence properties of an OV is a new subject in the field of singular optics, which will hopefully lead to a better understanding of OVs in the future.

3. Optical Vortex Creation

3.1 Introduction

As we have discussed in chapter 2, optical vortices were known to occur naturally in cylindrical beams [28, 29] and in scattered light [27, 52], but it wasn't until 1992 when Bazhenov et al. [11] first demonstrated that optical vortices could be created by a computer generated hologram (CGH) that OV beams were able to be created in a controlled manor [12]. The ability to synthesize optical vortices gave scientists control over the topological charge and the core size of an optical vortex as well as the number and arrangement of optical vortices in a beam of light.

While Bazhenov [11] and Heckenberg et al. [12] were advancing optical vortex creation by means of a CGH, Beijersebergen et al. demonstrated that optical vortices could also be created by means of a diffractive optical element (DOE) [14]. A vortex DOE creates an optical vortex or an arrangement of vortices by imprinting the desired phase structure directly into the beam with an etched plate of glass [15]. Although vortex CGH's are cheaper and easier to produce than a vortex DOE, a CGH is easier to damage under high power and thus are ill suited to optical limiting applications. Therefore in this chapter, we will limit our discussion to OV creation by a DOE as this is the method most relevant to our coherence filtering technique.

As we will show in the next chapter, for coherence filtering applications the most important property associated with an OV is the shape of the core profile. To increase

the rejection of a beam of light we wish to filter, the vortex core must be made larger.

Also if the core is misshapen in some way the light we intend to filter may leak into the

detected signal degrading our results. As has been shown in previous works [142, 143],

the initial phase profile of a vortex beam determines the shape of the propagated vortex

core. Therefore we have also provided a detailed method [146] for retrieving an

accurate phase map of a vortex DOE, which may be used to determine the quality of the

vortex produced.

3.2 A Single Optical Vortex Beam

A single optical vortex in the center of a scalar monochromatic beam propagating

in the z direction may be written in cylindrical coordinates (r, ϕ, z)[4]:

$$E(r, \phi, z, t) = A(r, z)\exp(im\phi)\exp(ikz - i\omega t) \qquad (3.1)$$

where $A(r, z)$ is a circularly symmetric amplitude function, $k=2\pi/\lambda$ is the wave number of

a monochromatic field of wavelength λ, ω is the angular frequency, and m is the

topological charge as defined in chapter 2. The amplitude and phase of a typical vortex

beam are shown in Fig. 3.1. The vortex nature of the field is governed by the phase

factor, $exp(im\phi)$. At a fixed instant of time helical surfaces of constant phase given by

$m\phi-kz$=const are produced for integer values of m. Along the helix axis (r=0) the phase

is undefined and thus this point is known as a phase singularity [27]. The amplitude also

vanishes along the helix axis (r=0) owing to destructive interference in the vicinity of the

vortex core i.e., $A(0, z)$=0 (see Fig. 3.1).

As we have discussed in Chapter 2, optical vortices may be classified as either large-core or small-core depending on the shape of A(r,z). Large core vortices have an amplitude profile that may be described by a Laguerre-Gaussian mode of order m [29, 30]:

$$A(r,z=0) = (r/w_0)^m \exp(-r^2/w_0^2)$$ (3.2)

where w_0 is the beam waist size in the plane z=0. Large core vortices have the property that the ratio of the vortex core size to the beam waist size is a constant. In contrast, small core vortices may be created arbitrarily small when compared to the beam waist size and may be described by an amplitude profile [13],

$$A(r,z=0) = \tanh(r/w_v)\exp(-r^2/w_0^2)$$ (3.3)

where w_v is the vortex core size. The amplitude profiles of a large core and small core vortex are depicted in Fig. 3.2. The ratio of the beam waist size to the vortex core size, $\beta=w_0/w_v$ [13, 99], may be used to determine if a vortex is a large-core or a small-core vortex. For a large core vortex described by Eq. (3.2), $\beta \approx 1$ and for a small core vortex described by Eq.(3.3), $\beta > 1$. As we will show in the next section, the vortex produced by a DOE may be described by a small core vortex with a value of β that decreases upon propagation.

3.3 Vortex Creation by a Diffractive Optical Element

To produce an optical vortex one need only recreate the spiral phase structure discussed in section 3.2. A monochromatic, planar ($m=0$) beam may be given such a

phase structure by transmitting the light through a transparent diffractive phase mask

having a thickness given by,

$$d = d_0 - m\lambda_0 \phi / 2\pi (n_s - n_0)$$
(3.4)

where d_0 is the nominal thickness, λ_0 is the wavelength for which the mask is intended, n_s

is the refractive index of the substrate, and n_0 is the index of refraction of the surrounding

medium. Light transmitted through the mask gains an azimuthally varying phase as

described previously. As a result, a dark core is embedded in the amplitude profile.

The propagation of a beam of light passing through a vortex mask may be

calculated near to the mask ($z < z_R = \pi w_0^2 / 2$), with the Fresnel Equation [144],

$$E(x',y',z) = \frac{\exp(ikz)}{i\lambda z} \exp\left(i\frac{k}{2z}(x'^2 + y'^2)\right)$$
(3.5)
$$\times \int\int_{-\infty}^{\infty} \left\{ E(x,y,z=0)\exp\left(i\frac{k}{2z}(x^2 + y^2)\right) \right\} \exp\left(i\frac{2\pi}{\lambda z}(xx' + yy')\right) dx dy$$

and far from the mask ($z \gg z_R$) with the Fraunhoufer Equation [144],

$$E(x',y',z) = \left(\frac{1}{i\lambda z}\right)\exp\left(ikz + i\frac{k}{2z}(x'^2 + y'^2)\right)$$
$$\times \int\int_{-\infty}^{\infty} E(x,y,z=0)\exp\left(-i\frac{2\pi}{\lambda z}(xx' + yy')\right) dx dy$$
(3.6)

The propagation of a Gaussian beam with a waist size, $w_0 = 100\lambda$, through an ideal vortex

DOE was calculated in the near field of the phase mask ($z = 0.03z_R$) and in the far field of

the mask ($z = 10z_R$) by numerically computing Eq. (3.5) and Eq. (3.6) respectively.

Normalized radial line profiles of the beam amplitude in the near field and far field are

shown in Fig. 3.3. In the near field (Fig. 3.3(a)) the vortex core has a smaller core size to

beam size ratio than in the far field (Fig. 3.3(b)). A least squares fit of the two plots

depicted in Fig. 3.3 to Eq. (3.3) was used to obtain a value of w_v in the near field and the far field. The least square fits suggests that in the near field at $z=0.03z_R$, $\beta=15.6$ and in the far field at $z=10z_R$, $\beta=4.6$.

Radial line plots were generated for different values of z and the line plots were fit to Eq. (3.3) by the method of least squares. The fit values of w_v we obtained were then used to generate a plot β as a function of z (shown in Fig. 3.4). As z was increased the value of β decreased to a constant value in the far field as may be seen in Fig. 3.4. Since the rate of change of β decreased as z was increased, the plot of β vs. z was then fit by the method of least squares to the equation:

$$\beta(z) = \beta_{FF} + \beta' \exp(-z/z_v) \tag{3.7}$$

where β_{FF} is the far-field value of β, $\beta_{FF}+\beta'=\beta_0$; the value of β at the output of the phase mask, and z_v is a characteristic decay length. In Fig. 3.4 the value of β varies rapidly near the mask and approach the constant value of $\beta_{FF}=4.6$ when $z>z_v=0.085z_R$. This effect is easily understood by examining the spatial frequency content of the field as it propagates. Components of the field with higher spatially frequencies propagate at higher angles with respect to the direction of propagation than do components with lower spatial frequencies [144]. Therefore the high spatial frequency content moves to the edge of the beam as it propagates and the vortex core at the center of the beam grows larger in size since high spatial frequencies are required to create a small-core vortex.

An OV DOE may be created by a variety of different methods [14, 15], but the most common method is ion beam lithography. It is very difficult to produce an ideal, smooth varying, phase ramp in practice; therefore, the phase ramp is often approximated

by a spiral staircase pattern composed of N-discrete steps. An N=8 step mask is depicted

in Fig. 3.5. A beam of light transmitted through a discrete stepped mask will gain the

azimuthal phase ramp as discussed above but will also gain phase rips at each step in the

mask. The severity of the distortion to the amplitude profile of a beam is dependent on

the number of steps used to create the spiral structure. The amplitude distortion across a

phase rip may be quantified by calculating the propagation of a field with a phase profile

given by a step function:

$$E(x) = E_0 \exp\left[-i\Delta\theta step(x)\right] \tag{3.8}$$

where x is the coordinate perpendicular to the phase rip normalized by the propagated

beam size, w(z), and $\Delta\theta$ is the size of the phase step located at x=0 (see Fig. 3.6(a)), and

$$step(x) = \begin{cases} 0 & x \leq 0 \\ 1 & x > 0 \end{cases} \tag{3.9}$$

In order to form a harmonic solution the phase of a vortex DOE must increase by $2\pi m$

radians in a single revolution. Therefore as N is increased, $\Delta\phi$ for each step decreases.

We numerically calculated the amplitude profile perpendicular to a phase step in the

plane $z=.03z_R$ for various N stepped m=1 vortex masks (see Fig. 3.6(b). As N is

increased the depth of the amplitude dips decreases approaching the flat profile when no

phase step is present (the N=0 case shown in Fig. 3.6(b)). It is apparent from Fig. 3.6(b),

that the more steps the mask possesses the closer the mask will approximate a smooth

varying phase ramp.

We numerically calculated the amplitude and phase of a beam of light transmitted

through an N=8 stepped vortex DOE by using Eq. (3.5) and Eq. (3.6). We assumed the

field at the input plane of the mask had a Gaussian amplitude profile with a waist size,

$w_0 = 50\lambda$, and a planar phase front. In the near field of the mask ($z = 0.13z_R$), the beam

contains a dark core of destructive interference at $r = 0$ and phase rips along each phase

step of the mask (see Fig. 3.7(a, b)). Far from the mask ($z = 10z_R$), the phase steps of the

mask produce a starburst pattern composed of high spatial frequency components (see

Fig. 3.7(c)) and the phase profile at the center of the beam is a smoothly varying phase

ramp (see Fig. 3.7(d)). Therefore, if necessary we may remove the effects of the phase

rips and obtain a smooth varying phase ramp by passing the OV beam through a low-pass

filter [145]. This will remove the high spatial frequency starburst pattern and reduce the

phase rips associated with it. However this has the effect of increasing the size of the

vortex core since high spatial frequencies are required to produce a small-core vortex

[13].

3.4 Vortex Mask Metrology

An optical vortex produced by a DOE may be misshapen if the mask itself is not

manufactured correctly. This may affect the coherence filtering properties of the vortex

and may lead to spurious results. In order to ascertain if our masks were made correctly,

we needed to create a depth profile of the mask as a function of the mask coordinates (x_m,

y_m). Transmission phase mask metrology may be performed by a variety of different

techniques. In this section we will discuss how we may retrieve an accurate depth profile

of a test object by means of a Fourier transform algorithm performed on an interferogram

of the test object [146].

When light is transmitted through a test object, the thickness of the object produces phase distortions in the beam of light. The phase distortions may be stored in an interferogram by placing the test object in one arm of a Mach-Zehnder interferometer as depicted in Fig. 3.8. Light from a laser beam is split into two paths by a beamsplitter (labeled BS1 in Fig. 3.8). One beam known as the object arm is passed through the object being tested, in our case a vortex DOE located at z=0. The second beam known as the reference arm may be passed through a reference object or may be allowed to propagate freely. In our case we compared the object arm to the reference arm itself with no reference object. The two arms are then reflected from two mirrors (M1 and M2 in Fig. 3.8) and are recombined at a second beamsplitter (labeled BS2 in Fig. 3.8). At the output plane of the second beamsplitter, the electric field may be described as $E_T=E_{obj}+E_{ref}$, where E_{obj} is the field produced by the object arm and E_{ref} is the field produced by the reference arm. An image of the interference pattern produced by the recombination of the beams known as an interferogram may then be captured with an imaging system as depicted in Fig. 3.8.

For simplicity we will assume the light incident on the first beamsplitter is a planar beam with constant amplitude $2E_0$ and we will also assume the first beamsplitter splits the incident light into two equal amplitude beams. The first beam is called the object arm and may be described by,

$$E_{obj} = E_0 \exp\!\left(i\vec{k}\cdot\vec{r}_{obj} - i\Theta(x,y)\right) \qquad (3.10)$$

where $\vec{r}_{obj}$ is the direction E_{obj} is propagating and $\Theta(x,y)$ is the phase information we wish to measure. The second beam is called the reference arm and may be described by,

$$E_{ref} = E_0 \exp\left(i\vec{k} \cdot \vec{r}_{ref}\right) \qquad (3.11)$$

where $\vec{r}_{ref}$ is the direction E_{ref} is propagating. We will also assume $\vec{r}_{obj}$ is directed along

the z-axis and $\vec{r}_{ref}$ is tilted with respect to the z-axis by an angle ψ in the x-z plane (see

Fig. 3.8 (inset)). If the z=0 plane is imaged, the captured interferogram is given by,

$$I(x,y,z=0) = \left|E_{obj}\right|^2 + \left|E_{ref}\right|^2 + 2\,\mathrm{Re}\left\{E_{obj}E_{ref}^*\right\}\cos\left(\frac{2\pi x}{\Lambda} + \Theta(x,y)\right) \qquad (3.12)$$

where $\Lambda=1/\cos\psi$ is the fringe spacing.

A test object placed in the object arm will produce phase distortions in E_{obj}, which

will distort the fringe pattern produced by the interferometer. An interferogram produced

by the interference of an ideal m=1 vortex phase mask and a plane wave reference beam

is shown in Fig. 3.9(a). At the vortex core, a single dark fringe forks into two dark

fringes. This forking pattern is characteristic to singular beams. A beam containing a

vortex of charge m, will have an interferogram that possesses an m+1 prong forked fringe

pattern [ref]. If an N-stepped vortex DOE is used instead, kinks will form in the fringes

at each phase step as shown in Fig. 3.9(b).

In essence the interferogram is able to store the phase information associated with

E_{obj} in the deformation of the fringes. The phase information may be extracted from the

interferogram by a Fourier phase retrieval algorithm [146] if we represent the

interferogram described by Eq. (3.12) as the sum of three terms:

$$I(x,y) = a(x,y) + c(x,y)\exp(i2\pi f_0 x) + c^*(x,y)\exp(-i2\pi f_0 x) \qquad (3.13)$$

The first term, a(x,y) represents the background intensity, $|E_{obj}|^2 + |E_{ref}|^2$. The second term,

c(x,y)exp(i2πf_0x),is a phase shifted complex exponential and

$$c(x,y) = \mathrm{Re}\left\{E_{obj}E_{ref}^{*}\right\}\exp(i\Theta(x,y)) \tag{3.14}$$

contains the desired phase information: $\Theta(x,y)$. Lastly, the third term,

$c^{*}(x,y)\exp(-i2\pi f_0 x)$, is just the complex conjugate of the second term.

A spatial Fourier transform performed on Eq. (3.13) leads to the spectrum:

$$I(f_x,f_y) = A(f_x,f_y)+C(f_x - f_0,f_y)+C^{*}(f_x + f_0,f_y) \tag{3.15}$$

Like the interferogram, the spectrum is also the sum of three terms and is graphically

depicted in Fig. 3.10(a). The first term $A(f_x,f_y)$ is the spectrum of the background signal

$a(x,y)$. The second term, $C(f_x-f_0,f_y)$ is the spectrum of the second term in Eq. (3.13), and

is centered at the carrier frequency f_0. The shift of the second term in the spectrum to

frequency f_0 occurs because of the shifting property of a Fourier transform, which states

that a phase-shifted signal is shifted in frequency space. The third term in the spectrum,

$C^{*}(f_x+f_0,f_y)$, is the complex conjugate of the second term in the spectrum and is centered

at $-f_0$, again due to the shifting property of a Fourier transform.

To retrieve the desired phase information, we first band-pass filter the term,

$C(f_x-f_0,f_y)$. Information inside the band-pass (dashed box in Fig. 3.10(a) is kept and

information outside of it is discarded. A shift of the remaining spectrum by $-f_0$ produces

the spectrum $C(f_x,f_y)$ as shown in Fig. 3.10(b). An inverse Fourier transform may be used

to retrieve $c(x,y)$ given by Eq. (3.14). The desired phase map may then be extracted by

performing two mathematical operations on $c(x,y)$:

$$\Theta(x,y) = \mathrm{Re}\left\{\ln(c(x,y))\right\} \tag{3.16}$$

where ln() denotes a natural logarithm.

Several issues may arise while producing the phase map described by Eq. (3.16) and we will address a few of them briefly. To perform a numerical Fourier transform on an interferogram the interferogram should have dimensional sizes that are a represented by 2^n pixels in order to optimize a Fast-Fourier transform algorithm. This may be achieved by padding the interferogram with zeros. Zero padding may also be used to increase the resolution in Fourier space, which is given by 1/X, where X is the dimensional size of the interferogram being processed.

In order to increase the amount of phase information in Fourier space it is best to preprocess the interferogram described by Eq. (3.12), by multiplying the interferogram with a Gaussian window:

$$\text{Gauss(x,y)} = \exp(-(x^2 + y^2)/w_c^2) \tag{3.17}$$

where w_c is the characteristic cutoff size of the window. As an alternative we could also use a Hanning window [145]:

$$\text{Hann(x,y)} = \cos(\pi x/2w_c)\cos(\pi y/2w_c) \tag{3.18}$$

This function doesn't attenuate as much of the transmitted interferogram as a Gaussian function would and this is sometimes a desirable feature. Whichever function is used, the spectrum will be broadened and the extracted phase may be more accurately measured. It is also desirable to align the fringes of the interferogram to be perpendicular with the direction we wish to shift the spectrum in this case the x direction. If we then truncate the interferogram in the x-direction at equal intensity fringes on either side, then we may eliminate the effects of having a finite sized interferogram.

After the spectrum is produced the term $C(f_x - f_0, f_y)$ needs to be filtered from the rest of the spectrum. Many different band-pass filters are available for use, the simplest of which, are the Rect(x,y) function [ref]:

$$rect(f_x, f_y) = \begin{cases} 1 & -f_c \leq f_x \leq +f_c \text{ and } -f_c \leq f_y \leq +f_c \\ 0 & \text{otherwise} \end{cases} \tag{3.19}$$

and the Cyl(r) function [ref]:

$$cyl(f_x, f_y) = \begin{cases} 1 & 0 \leq \sqrt{f_x^2 + f_y^2} \leq f_c \\ 0 & \text{otherwise} \end{cases} \tag{3.20}$$

However the sharp cut at the edge of these filters may cause undesirable distortions to the phase information. In order to decrease this effect it is often desirable to filter with a soft aperture, which gradually decreases the spectrum to zero outside the filter window. A Gaussian window or Hanning window, described by Eq. (3.17) and (3.18) respectively may also be used in frequency space to perform band-pass filtering, where the coordinates (x,y) are now given by the spatial frequency coordinates (f_x, f_y) and w_c is instead given by f_c. The low-pass filters we have discussed above are depicted in Fig. 3.11, with general coordinates (x,y) which may be either spatial or frequency coordinates depending upon the application.

Using the algorithm and filtering techniques discussed above we retrieved the phase profiles from both numerically and experimentally generated interferograms. The interferogram and retrieved phase profiles of numerically generated ideal and N=8 stepped vortex DOEs are shown in Fig. 3.12. In the ideal case the phase map is accurately reproduced and in the N=8 stepped mask DOE case, the mask is reproduced

with a small amount of blurring across each phase step. This occurs because the band-pass filter has cutoff some of the high spatial frequency content of the beam, which causes edges to become less distinct. Both types of phase masks had a retrieved phase with a small amount of noise along the branch cut in the phase. This occurred because numerical noise is introduced by quantizing the intensity pattern of the interferogram. This causes the phase to oscillate about the branch cut between 0 and 2π.

An experimentally created interferogram and the retrieved phase profile of a vortex DOE with N=8 discrete steps are shown in Fig. 3.13. In this case the mask was designed to produce an m=1 vortex at a wavelength of 850nm [147] and the laser light used in the Mach-Zehnder interferometer had a wavelength of 633 nm. The experimental interferogram also shows the oscillations about the branch cut since it is inherent in the numerical technique we used. The phase mask depicted in Fig. 3.13 had a defect on its surface, but we were unable to determine from an image of the surface if the defect was a scratch or a piece of debris on the surface. However in the recreated phase profile we can now see that the defect is a divot in the surface with a chunk of debris located nearby. After careful inspection of several masks using the mask metrology method outlined above, we concluded that our vortex DOEs were made within the specifications given to us from Honeywell [147] and would not produce significant deviations in the core profile of a vortex.

3.5 Conclusions

In conclusion, we have demonstrated that an optical vortex may be produced by a diffractive optical element. We have also shown that the small-core vortices produced by such a method have a beam-to-core-size ratio, β, that decreases upon propagation exponentially, approaching a constant value in the far field. The diffractive masks we used had N-discrete steps which created large phase rips along each phase steps edge, which distorted the phase and amplitude of the propagated field. However, the phase rips are composed primarily of high spatial frequency components, which may be filtered out by a low-pass spatial filter. We have also demonstrated that the phase map of a vortex diffractive optical element may be retrieved from an interferogram by the method of a Fourier fringe pattern tomography.
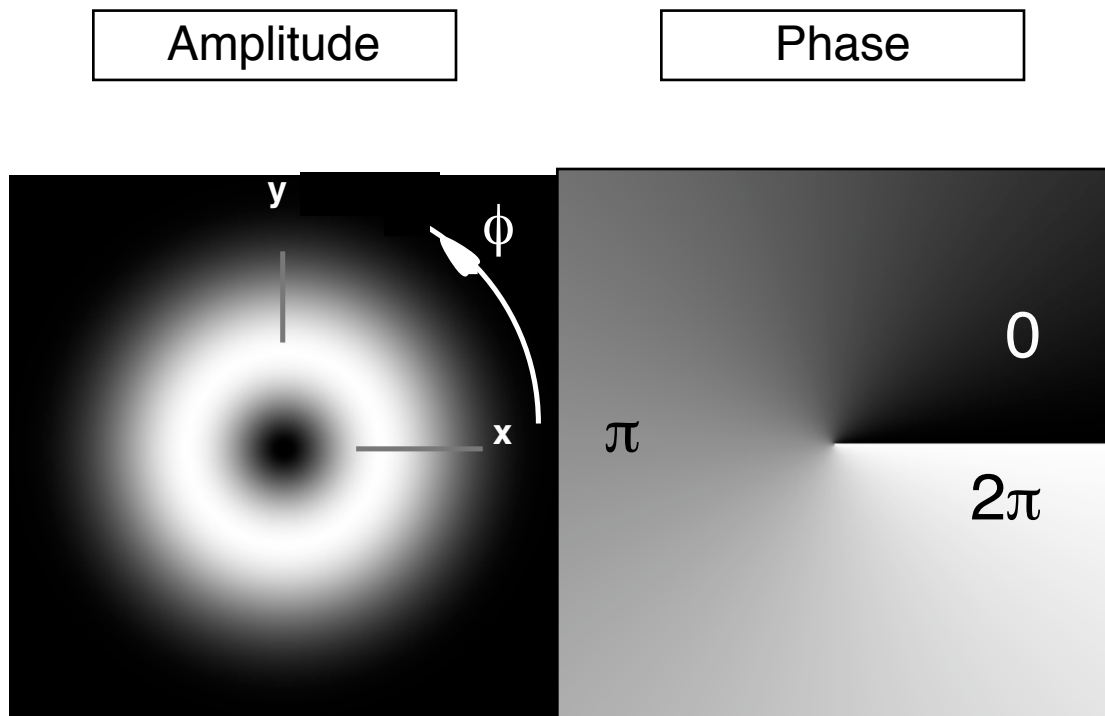
FIG. 3.1   The amplitude and phase profiles of an m=+1 optical vortex. At x=y=0 a

dark null of destructive interference known as the vortex core forms at a phase

singularity. The phase varies from 0-2π radians in a single revolution about the vortex
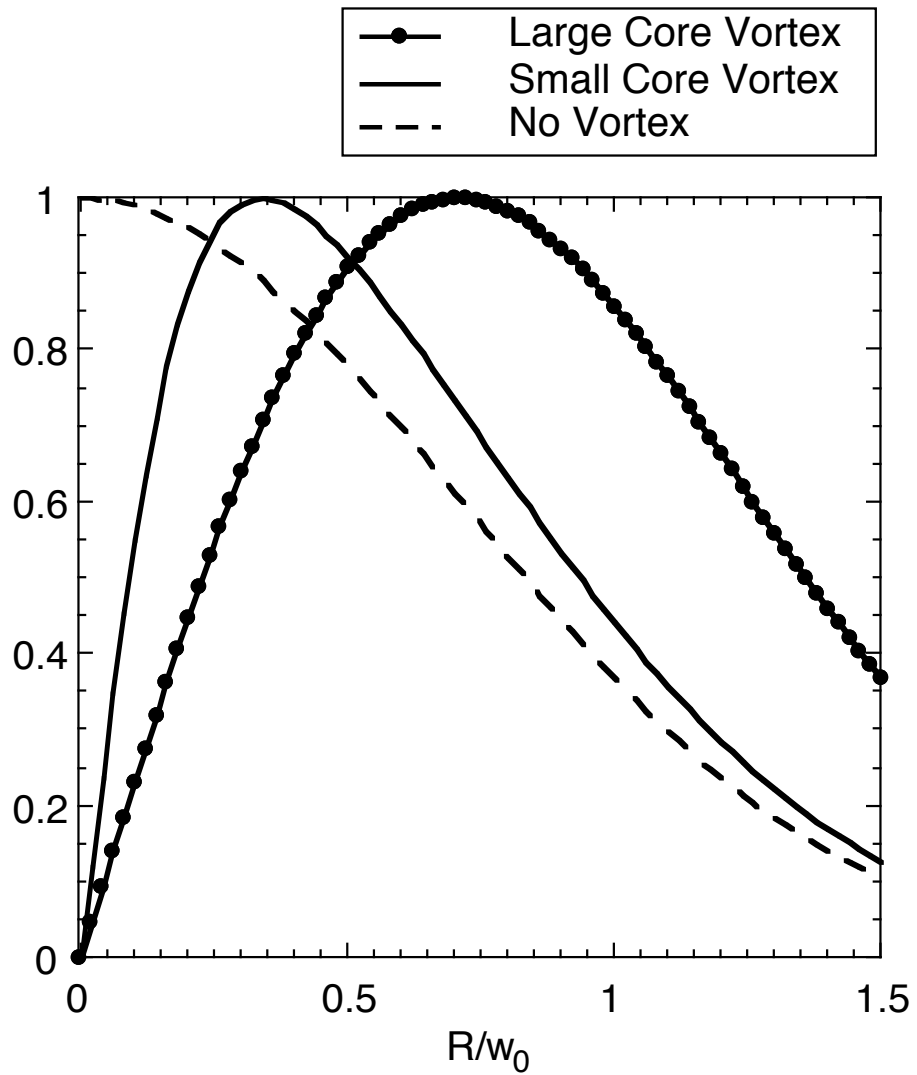
core.

FIG. 3.2   A comparison of amplitude profiles for large core (solid curve with dots)

and small core vortex beams (solid curve). A Gaussian beam (dashed curve) is also

shown for comparison. The small core vortex has a smaller tighter core as compared to

the large core vortex.
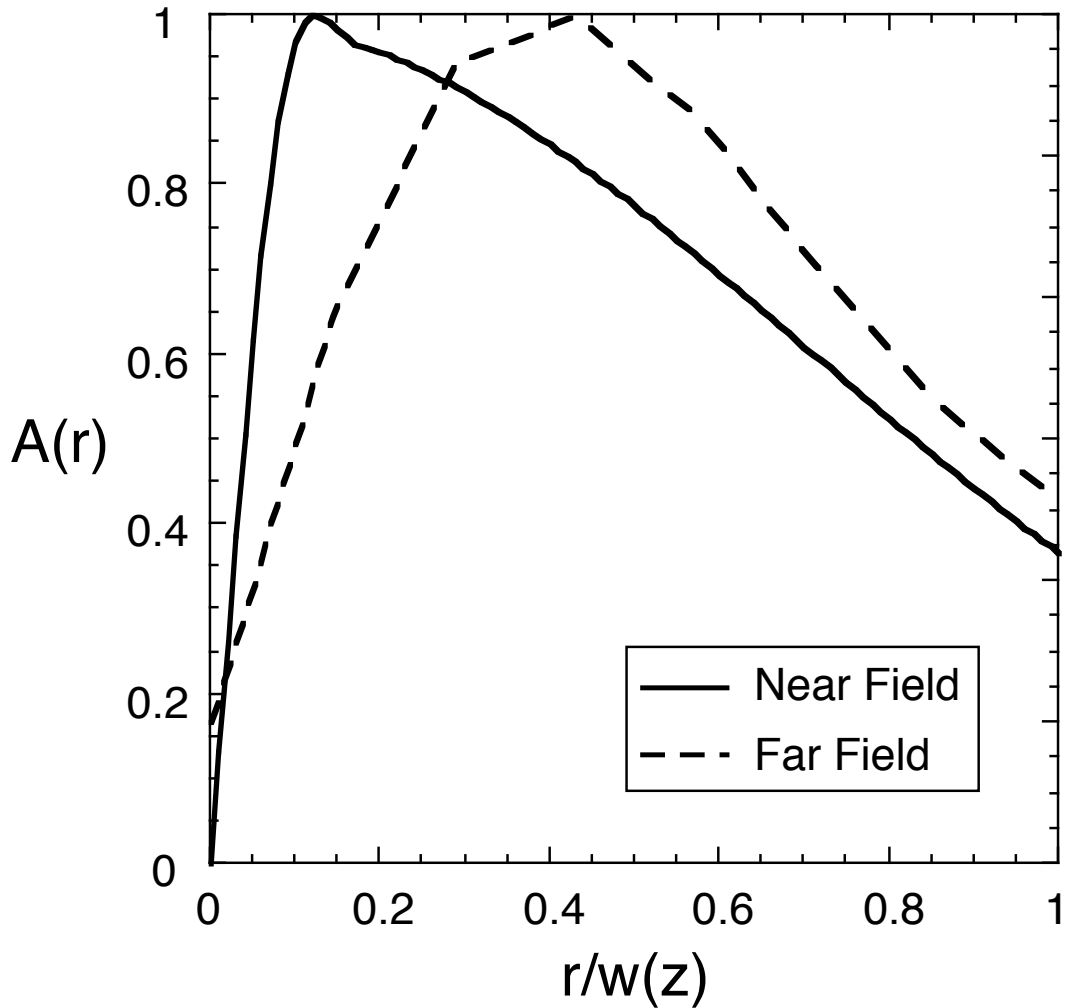
FIG. 3.3   A comparison of the near field (solid curve) and far field (dashed curve) profiles of a vortex beam produced by an ideal vortex DOE. The near field profile was measured at $z=.03z_R$ and the far field profile was measured at $z=100z_R$. In order to easily compare the two curves, the radial coordinate, r, of the near field curve was normalized by $w(z=.03z_R)$ and the radial coordinate of the far field curve was normalized by $w(z=100z_R)$.
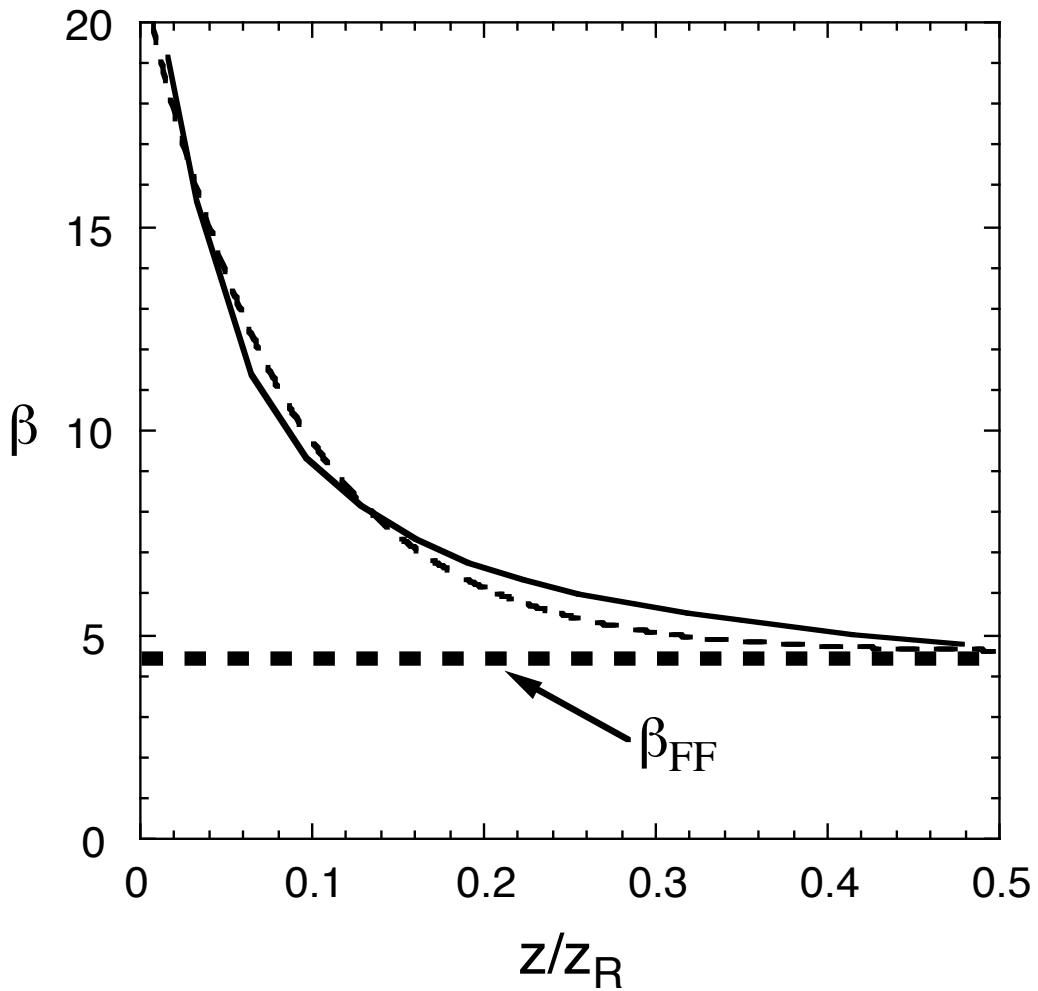
FIG. 3.4   A plot of the vortex core-to-beam-size ratio, β, as a function of the propagation distance z (solid curve). A least squares fit (dashed curve) reveals that β decays exponentially to a constant value of β_{FF}=4.6 with a decay length z_v=.085z_R.
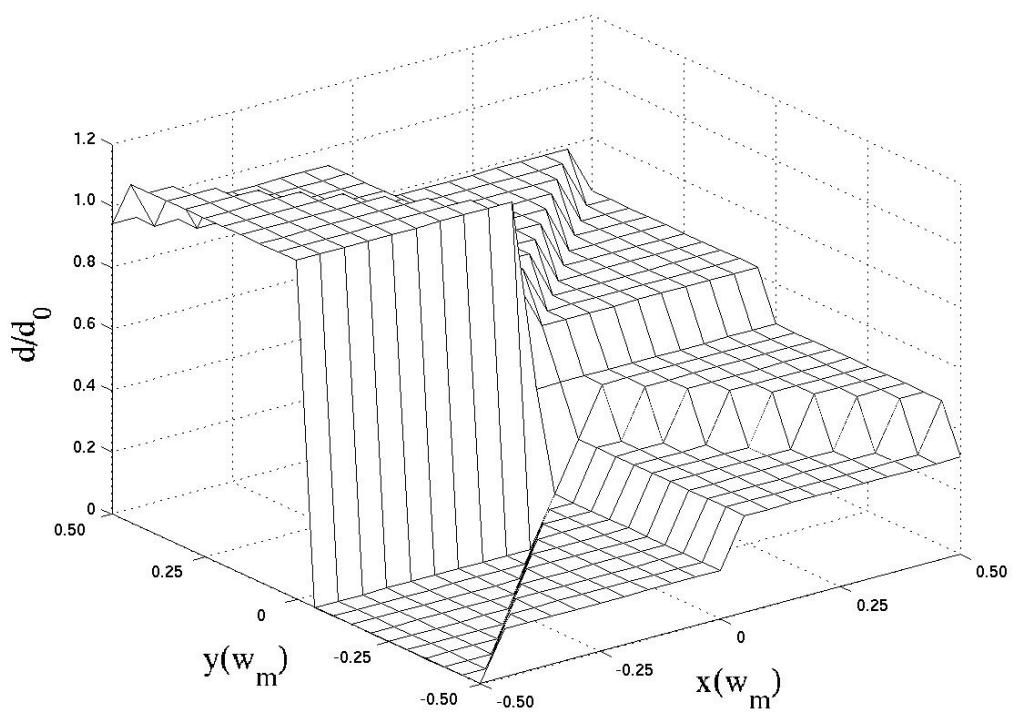
FIG. 3.5   A 3D plot of a discrete N=8 vortex DOE of dimensional size (w_m x w_m)

and total thickness, $d_0=\lambda_0/(n_s-n_0)$. In a revolution around the positive azimuthal direction,

each step increases in thickness from the previous one. This creates a spiral staircase

pattern etched into the glass.
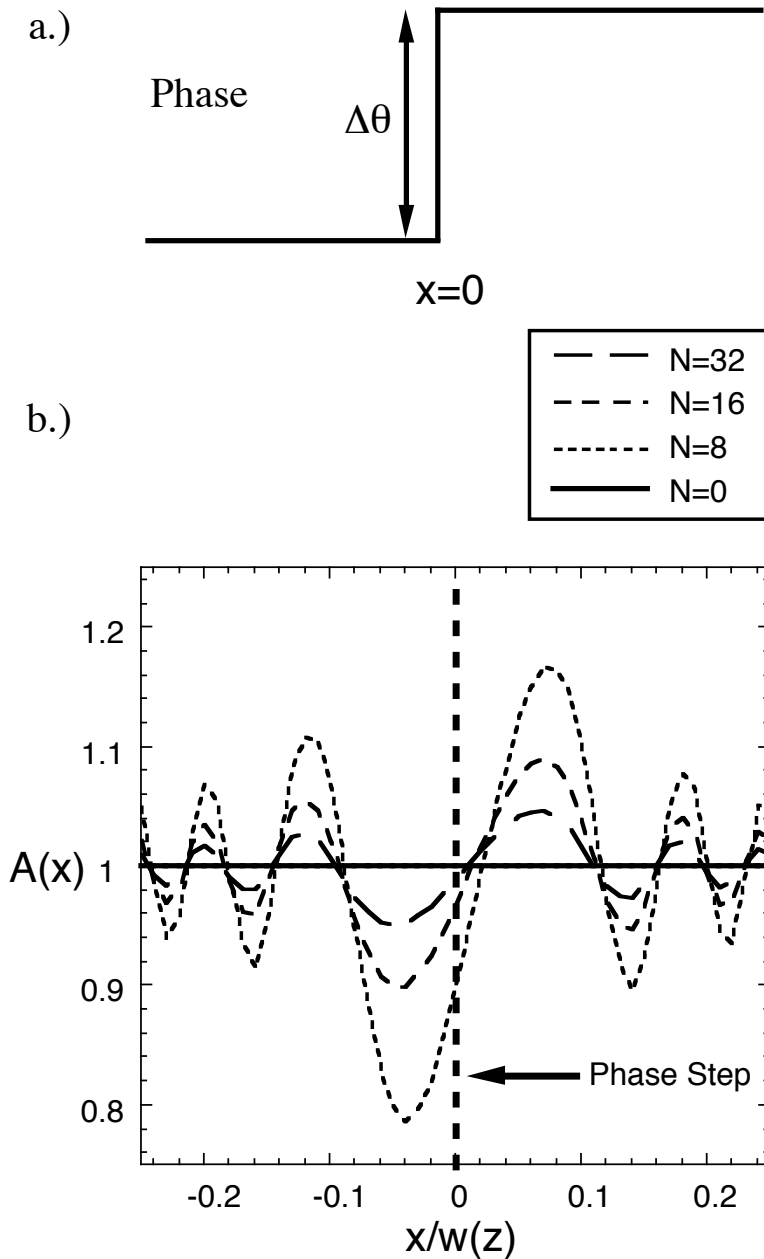
FIG. 3.6   Amplitude distortion at a phase step for an N=8, 16, and 32 step masks.

The case of no step (N=0) is also shown for comparison.   The amplitude is distorted

across the phase step. The amplitude peaks on one side of the step and dips on the other

side of the step. This effect decreases as N increases since the phase step is decreased in

size.
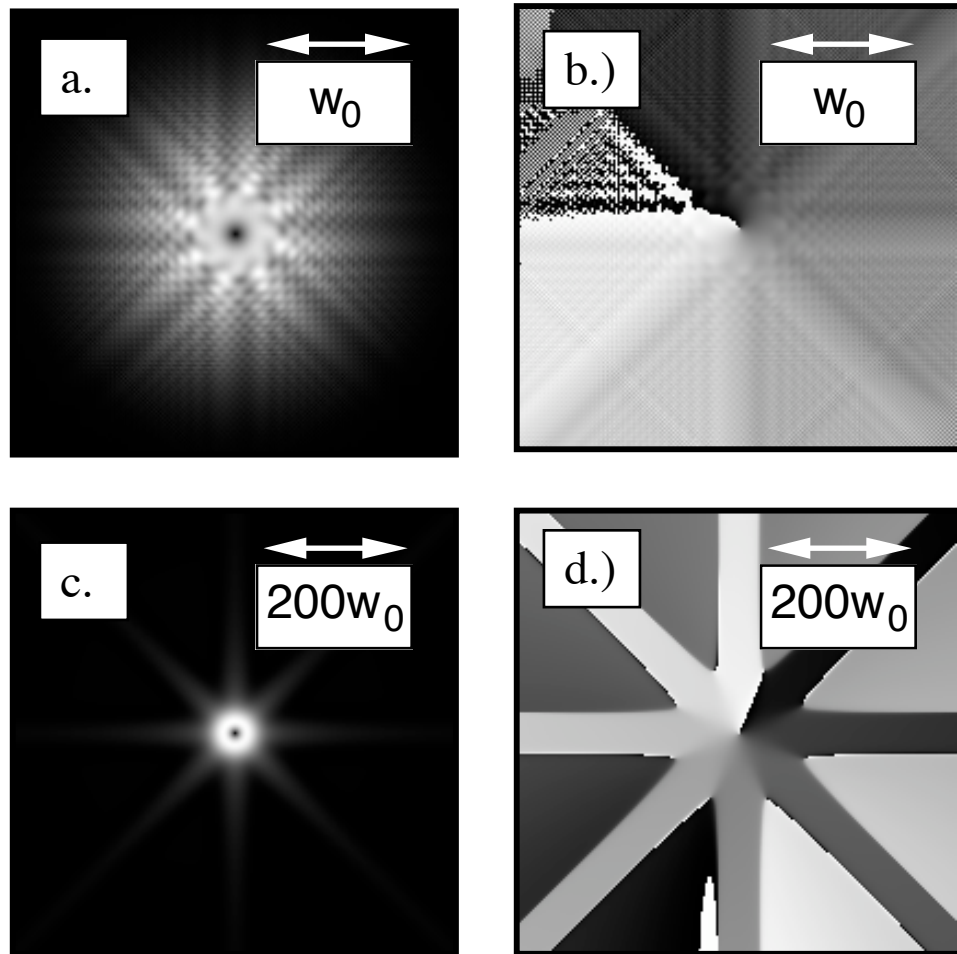
FIG. 3.7   A vortex beam created by an N=8 vortex DOE. The (a) amplitude and (b) phase of the beam in the near field ($z=0.12z_R$). Depicting phase rips where the amplitude and phase are heavily distorted. However a dark vortex core forms at the center of the beam. Frames (c) amplitude and (d) phase of the beam in the far field ($z=10z_R$). Showing a smoothly varying phase at the center of the beam surrounded by a high spatial frequency starburst pattern.
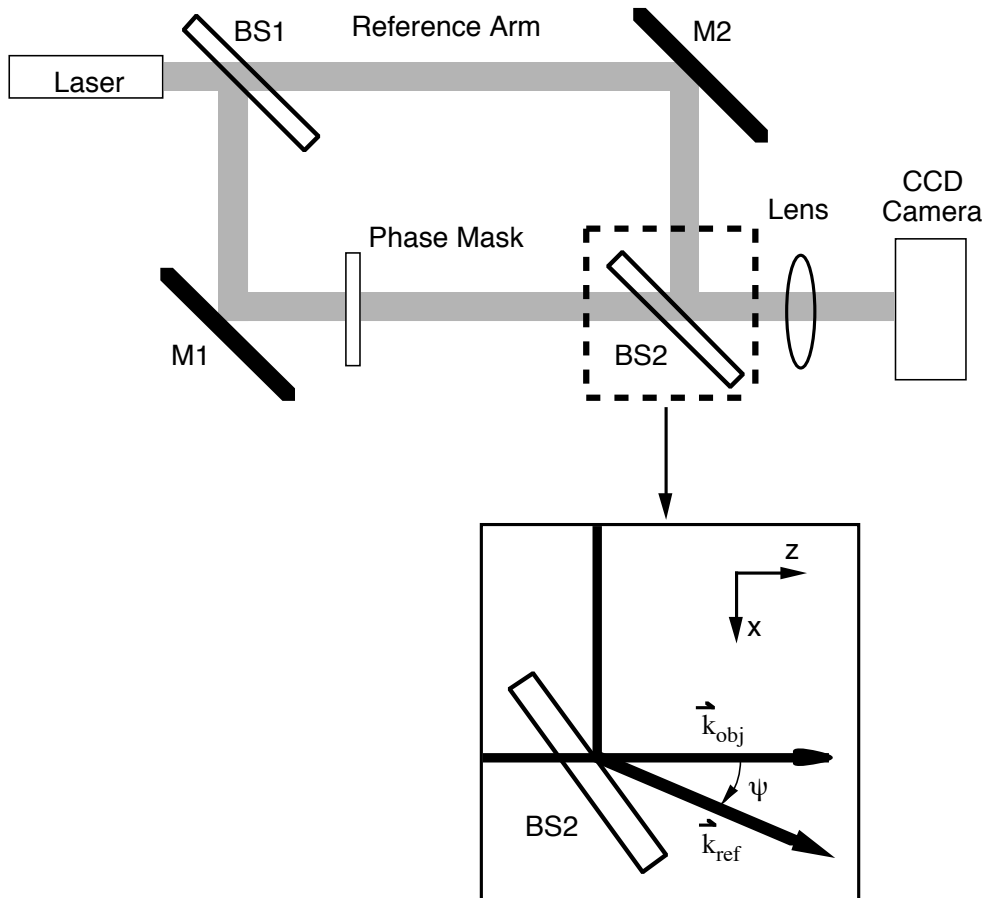
FIG. 3.8   Diagram of a Mach-Zehnder interferometer. A laser beam is split into two

paths by a beamsplitter (BS1). The two beams are then reflected from mirrors M1 and

M2 and are recombined at a second beamsplitter (BS2). The first beam is passed through

a test object (the phase mask) and the second beam is used as a reference beam. The

object beam is propagating in the direction of $\vec{k}_{obj}$ and the reference beam is propagating

in the direction of $\vec{k}_{ref}$, which is tilted with respect to the object arm by an angle ψ as

shown in the inset. The phase mask is then imaged by an imaging lens onto a CCD

camera.

Ideal   Phase Mask

$$\Lambda = \frac{2\pi}{f_0}$$
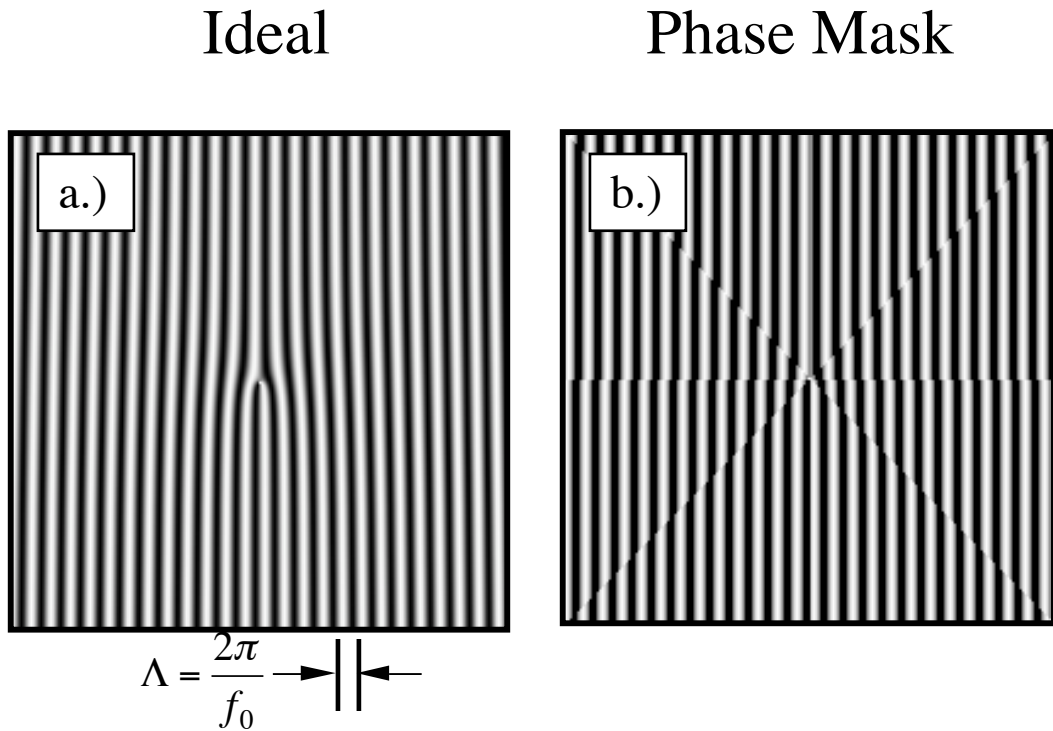
FIG. 3.9   A comparison of numerically generated interferograms produced by interfering a plane wave reference beam with a.) an ideal vortex DOE and b.) an N=8 stepped vortex DOE. Both produce a forking pattern in the fringes characteristic to optical vortices. However, the N=8 stepped vortex DOE produces kinks in the fringe patter at each phase step in the DOE.

a.)
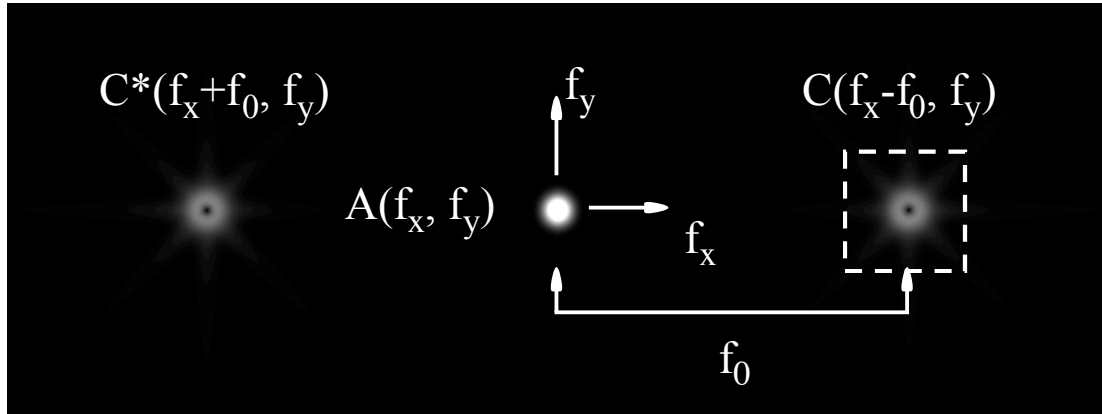
b.)
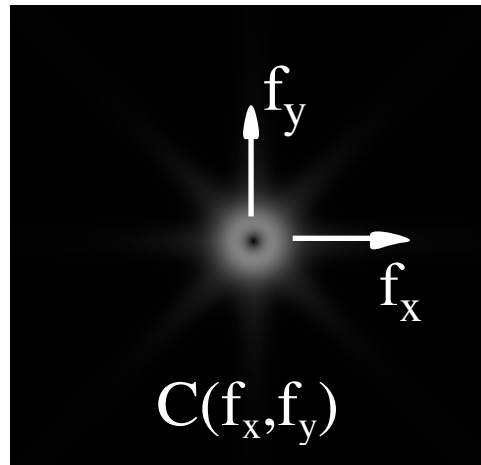
FIG. 3.10   a.) Spatial frequency spectrum of an interferogram produced by interfering a Gaussian reference beam with a vortex beam created by an N=8 vortex DOE. The spectrum is the sum of three terms, $A(f_x,f_y)$, located at the origin, $C(f_x-f_0,f_y)$ shifted to the carrier frequency f_0, and $C^*(f_x+f_0,f_y)$ shifted to $-f0$. The dashed square represents a band-pass filter used to extract $C(f_x-f_0,f_y)$ and eliminate the rest of the spectrum.

b.)   After bandpass filtering, the term $c(f_x-f_0,f_y)$ is shifted to the origin to obtain $C(f_x,f_y)$.

a.)
rect(x,y)

b.)
cyl(x,y)

c.)
Gaus(x,y)

d.)
Hann(x,y)
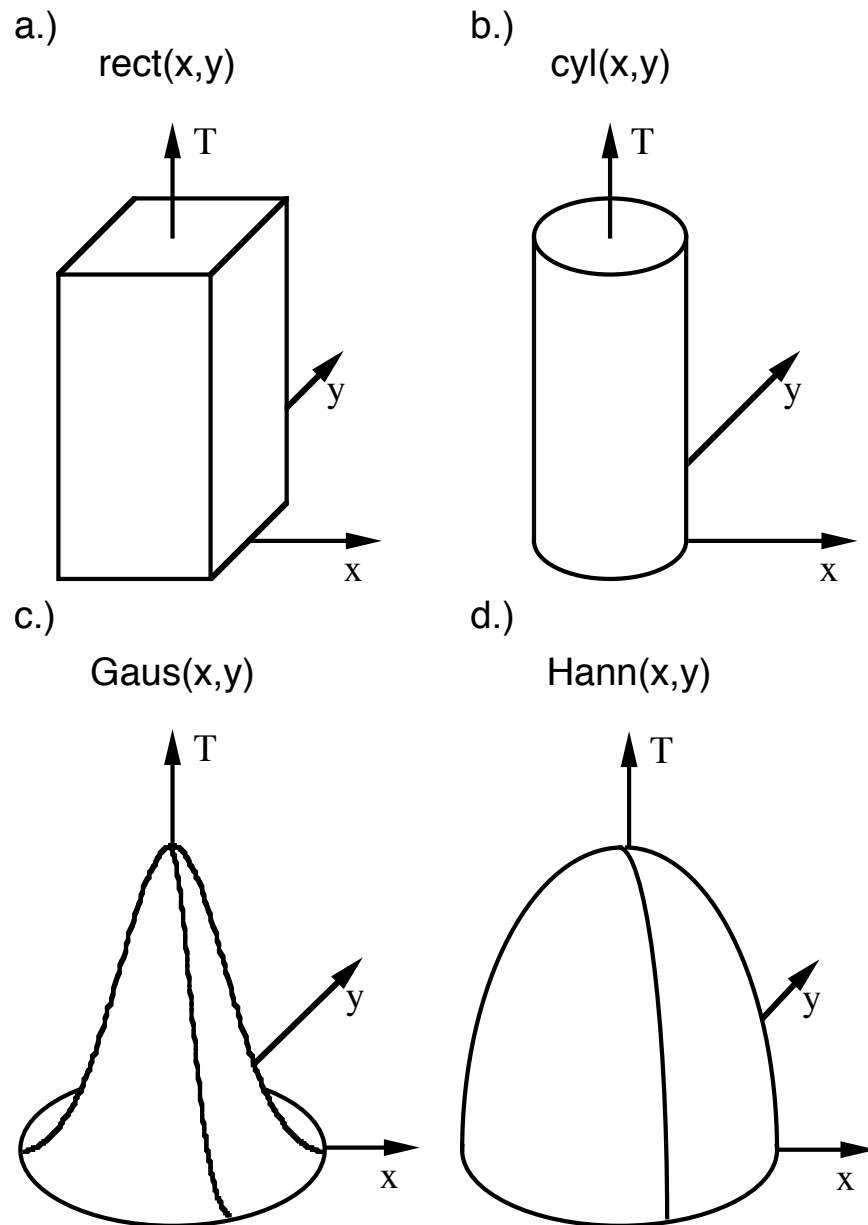
FIG. 3.11   A plot of the transmittance functions of four commonly used 2D band-

pass filters. The transmittance of a.) a square aperture, b) a circular aperture, c.) a

Gaussian aperture, and d.) Hanning window. All filters have unity transmittance at the

origin. Filters (a.) and b.) have sharp cutoffs where the transmittance falls to zero. Filters

(c) and (d) have transmittance functions that taper off more gradually towards zero.

Interferogram   Phase
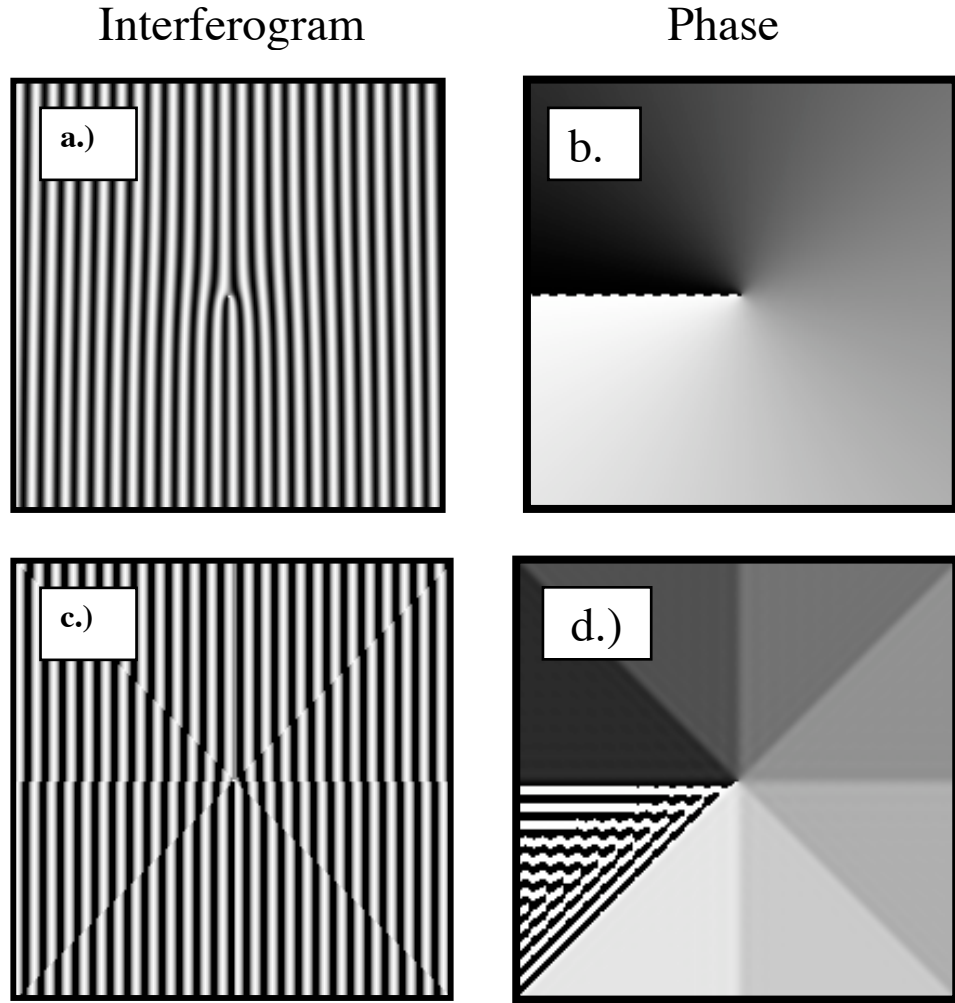
FIG. 3.12   Numerically calculated interferograms and retrieved phase profiles made

using a Fourier phase retrieval algorithm. The phase varies from 0 (black)-2π (white).

(a.) An interferogram of an ideal vortex DOE and (b.) the retrieved phase. (c.) An

interferogram of an N=8 vortex DOE and (d.) the retrieved phase. At the largest step in

the mask, both demonstrate a low level of noise in the phase, where values oscillate

between 0 and 2π. The N=8 vortex DOE also shows some blurring of the phase steps

because some of the high spatial frequencies have been removed during the filtering process.

Defects   **Defects**
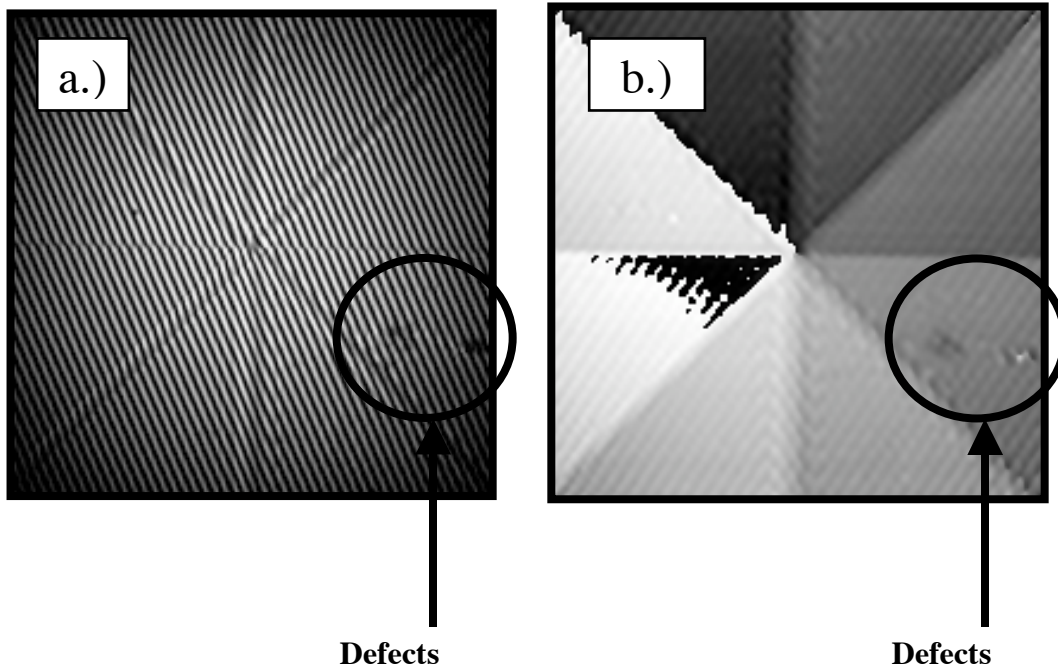
FIG. 3.13   a.) An experimental interferogram and b.) the retrieved phase profile made using a Fourier phase retrieval algorithm. The interferogram was made by placing an N=8 vortex DOE designed for λ_0=850nm into a Mach-Zehnder interferometer using a laser of wavelength λ=633nm. Defects appear in the lower right corner of the images (circles). Whether the defects are dust or scratches cannot be determined from the interferogram depicted in (a). However we can determine from the retrieved phase profile that the defect on the left is a divot and the defect on the right is a particle on the surface of the DOE.

4. The Nulling Properties of an Optical Vortex

4.1 Introduction

An optical vortex DOE may be used as a coherence filter by taking advantage of the destructive interference that occurs in the vortex core. In essence, "the vortex core opens a window in a spatially coherent beam of light, which may allow one to detect a weaker incoherent signal" [140]. In this chapter I will review the nulling properties of an optical-vortex-coherence-filter (OVCF) with the configuration depicted in Fig. 1. Light we wish to filter is passed through a vortex DOE placed at the entrance pupil of an imaging lens. The lens then focuses the light through an aperture of radial size R_{ap} placed in the focal region of the lens. I will review how the topological charge of the vortex produced by the vortex DOE and the size of the aperture effect the attenuation of a coherent beam of light.

I will then determine how the spectrum of the filtered light affects the attenuation properties of an OVCF. The vortex DOE is designed for one particular wavelength, however it is often desirable to form a polychromatic null. Therefore I will describe how an OVCF may be used to attenuate a polychromatic beam of light. In particular we will analyze the formation of fractional vortices when the wavelength of the filtered light does not match the wavelength for which the vortex DOE is intended. I will discuss how fractional vortices distort the amplitude profile of the filtered light and how this distortion affects the attenuation properties of an OVCF.

4.2 Power Attenuation

Let us assume a planar beam we wish to filter is transmitted through an ideal

vortex DOE of radial size w_m placed at a position z=0 as depicted in Fig. 4.1. The light in

the back focal plane of the lens, $E_f(r,z=f)$, is proportional to the Fourier transform of the

field at the entrance pupil of the lens,

$$E_f(r,z=f) \propto FT\left[E_i(r,z=0)\right] \tag{4.1}$$

where $E_i(r,z=0)=E_0\exp(im\phi)$ is the initial field at the output of the vortex DOE. The

Fourier transform of a vortex DOE may be quite complicated, therefore it is more fruitful

to examine the field in the back focal plane numerically. Numerically calculated radial

plots of the amplitude in the back focal plane, $|A(r,z=f)|$, are depicted in Fig. 4.2 for

|m|=0-4. For the m=0 case, no dark spot forms in the beam and the amplitude has the

profile of the familiar Airy pattern. However, for |m|>0 a dark core forms in the center of

the beam profile. When |m| increases in value the size of the core increases and the

center of the beam grows darker.

In the core region ($r<<w_0$), the amplitude may be approximated as [140],

$$A(r,z=f) \propto |r|^m \tag{4.2}$$

If an aperture is placed in the core region as depicted in Fig. 4.3, the amount of light

passing through the aperture will be decreased if m≠0. A plot of the numerically

calculated fraction of the total beam power transmitted through the aperture as a function

of the aperture size, R_{ap} is plotted in Fig. 4.4 for m=0-4. As the results show, when the

value of m is increased the beam attenuation is also increased (see Fig. 4.4). A least-

squares fit of Fig. 4.4 suggests that near the core, the fraction of transmitted power

decreases as:

$$\left(\delta P/P_{tot}\right) \propto \left(R_{ap}\big/\left(0.7+0.2m\right)\right)^{1.44+1.82\,m} \tag{4.3}$$

where δP is the transmitted power and P_{tot} is the total beam power impinging on the

aperture. Therefore if the fraction of transmitted power is known for a given aperture

size, it may be estimated for other aperture sizes as well by the relation [140],

$$\left(\delta P/P_{tot}\right)_2 \approx \left(\delta P/P_{tot}\right)_1 \left(R_{ap,2}\big/R_{ap,1}\right)^{1.44+1.82\,m} \tag{4.4}$$

According to Eq. (4.3) and (4.4) we may control the attenuation of a coherent beam of

light by controlling the charge of the vortex DOE and the size of the aperture in the

OVCF.

4.3 Spectral Attenuation Properties

4.3.1 Polychromatic Nulling

It is often desirable to obtain a polychromatic null, which may be difficult to do in

practice [148]. However, one may expect light passing through a vortex mask to form a

dark null over a wide range of wavelengths since vortices are robust phase structures,

which are known to persist even under strong perturbations to the wave front. In order to

verify this assertion, we examined the polychromatic transmission properties of an

OVCF. The field measured at the output of the OVCF may be expressed as a

superposition of spectral components,

$$E_{output} = \sum_{i=1}^{N} E_i(\lambda_i) \tag{4.5}$$

where $E_i(\lambda_i)$ is the ith spectral component of the field and N is the total number of components. Because the phase mask is designed to produce a charge m=1 vortex for one particular wavelength, λ_0, each component with a wavelength that differs from λ_0 will gain a different azimuthal phase retardation. For simplicity we will ignore the chromatic dispersion of the glass used to create the vortex DOE and assume a flat transmittance curve over the wavelength range under examination. According to Eq. (3.4), one may expect a vortex to form with a topological charge, $m'=\lambda_0/\lambda_i$ if the wavelength is not matched to the intended wavelength, λ_0. Therefore, we expect the vortex created by the DOE to have a topological charge, m>1 for spectral components with wavelengths shorter than λ_0, and to have a topological charge, m<1 for spectral components with wavelengths longer than λ_0. Since we could easily design the DOE to produce an m=1 vortex at the longest wavelength in the spectral range under examination, we will only consider the creation of vortices with topological charge m≥1.

To explore how a non-integer charged vortex affects the attenuation properties of an OVCF, we numerically computed the power transmission of an OVCF as a function of the wavelength. In our simulations, the OVCF was arranged with the geometry depicted in Fig. 1 and the field in the focal plane of the lens was calculated using Eq. (4.1). The fraction of power transmitted through an OVCF was calculated for wavelengths,

$$\lambda_i = \lambda_0 - \Delta\lambda \tag{4.6}$$

where $\Delta\lambda$ is the wavelength mismatch between λ_i and λ_0. A plot of the numerically calculated fraction of transmitted power, $(\delta P/P_{tot})$ as a function of the aperture size, R_{ap} is

shown in Fig. 4.5 for values of $0 \leq \Delta\lambda \leq \lambda_0/2$. When $\Delta\lambda \neq 0$, the curve of $(\delta P/P_{tot})$ vs. R_{ap}

falls in a region depicted in Fig. 4.5 as a gray zone. Interestingly, the attenuation curves

were improved for all wavelengths when $R_{ap} > 0.3R_{diff}$, but were degraded for small

aperture sizes ($R_{ap} < 0.3R_{diff}$) when $\Delta\lambda < \lambda_0/3$. The most degradation to the attenuation

curves occurred in our modeled data when $\Delta\lambda = 0.22\lambda_0$. Therefore we can create a

polychromatic null in the filtered beam if we constrain the aperture sizes to $R_{ap} > 0.3\ R_{diff}$.

The formation of a polychromatic null and its degradation at smaller aperture sizes may

be explained by examining the propagation of a light beam that has been transmitted

through a vortex DOE as we will do in the next section.

4.3.2 Fractional Vortices

        We numerically calculated the propagated beam profile one Rayleigh diffraction

length ($z = z_R$) away from an ideal vortex DOE located at $z = 0$ by numerically calculating

Eq. (3.5). It was clear that a mismatched wavelength passed through a vortex DOE will

produce a non-integer topological charge, $m' = m + \Delta m$, where m is the topological charge

at λ_0 and Δm is the additional topological charge, but the most surprising result in our

simulations was the presence of a secondary defect in the propagated beam. The beam

amplitude and phase in the plane $z = z_R$ are depicted in Fig. 4.6 for several values of $\Delta\lambda$.

As expected a circularly symmetric dark core is seen at the center of the beam when

$\Delta\lambda = 0$ (Fig. 4.6 (a,b)). However, when $\Delta\lambda \neq 0$ the dark core is shifted radially off-center by

an amount Δr (as shown in Fig. 4.6(c-f)) and the core is no longer circularly symmetric.

In addition to this shift, when $\Delta\lambda > \lambda_0/9$ ($\Delta m = 0.125$) a secondary defect is also created (indicated by arrows in Fig. 4.6). The secondary defect initially forms at the edge of the beam when $\Delta\lambda = \lambda_0/9$ ($\Delta m = 0.125$) as shown in Fig. 4.6 (c,d). However as $\Delta\lambda$ is further increased the secondary defect moves closer to the center of the beam until merging with the primary core to form a charge m=2 vortex when $\Delta\lambda = \lambda_0/2$ ($\Delta m = 1$) as shown in Fig. 4.7. Figure 4.6 suggests that when $\Delta\lambda < \lambda_0/3$ ($\Delta m = 0.5$) the secondary defect possesses fractional topological charge (see Fig. 4.6(c-f)) and Fig. 4.7 suggests that when $\Delta\lambda > \lambda_0/3$ the secondary defect has unity topological charge (see Fig. 4.7 (a-d). Therefore the secondary defect appears to have gained topological charge before reaching the $z = z_R$ plane when $\Delta\lambda > \lambda_0/3$ ($\Delta m > 0.5$).

We also numerically calculated the beam in the plane $z = 10 z_R$ (See Fig. 4.8), for values of $\Delta\lambda < \lambda_0/3$ ($\Delta m < 0.5$) to see if these secondary defects would also evolve into vortices with unity topological charge. As may be seen in Fig. 4.8 (a,b) when $\Delta\lambda < \lambda_0/9$ ($\Delta m < 0.125$) the phase of the beam is smooth and the secondary defect is no longer present. However, for values of $\Delta\lambda > \lambda_0/9$ ($\Delta m > 0.125$) all the secondary defects now have unity topological charge (indicated by arrows in Fig. 4.8 (c-f)).

To summarize, when $\Delta\lambda > \lambda_0/3$ ($\Delta m > 0.5$) the secondary defects evolved into unity charged vortices in the near field. Also, when $\Delta\lambda$ was in the range, $\lambda_0/9 < \Delta\lambda < \lambda_0/3$ ($0.125 < \Delta m < 0.5$), the secondary defects evolved into unity charged vortices in the far field but are removed from the beam when $\Delta\lambda < \lambda_0/9$ ($\Delta m < 0.125$). Therefore, we named the secondary defects, "fractional vortices" [4], if they evolved into unity charged vortices under propagation. We can now explain why the attenuation curves depicted in

Fig. 4.5 were improved for wavelengths shorter than λ_0. When $\Delta\lambda < \lambda_0$, the vortex core

was shifted off center and deformed, so one may expect the attenuation curve to be

degraded since light could leak into the filtering aperture. However the presence of the

secondary defect compensated for the additional light by providing additional

attenuation. When $R_{ap} < 0.3\ R_{diff}$, the secondary defect no longer provided assistance

since it lay outside the aperture and the curves are degraded as was observed (see Fig.

4.5).

There is now the question of how the secondary defects evolve into unity charged

vortices upon propagation. This may easily be explained by first examining the light in

the z=0 plane. In the z=0 plane, a vortex of fraction charge, m′, may be expressed as an

infinite series of vortex modes having integer charge n [4,139]:

$$\exp(im'\phi) = \sum_{-\infty}^{+\infty} C_n \exp(in\phi) \tag{4.7}$$

where $C_n = (-1)^n \operatorname{sinc}\big(\pi(m'-n)\big)\exp(i\pi m')$. The various modes represented by Eq. (4.7)

will disperse upon propagation. Therefore in a given z plane the modes will interfere and

the field may be represented as a composite beam [118]. Composite vortex beams are

known to contain multiple vortices, which may have different positions than the vortices

in the decomposed beams. Also, composite vortex beam often appear to contain higher

topological charge than the decomposed beams possess. This may account for the

additional vortices seen in Fig. 4.6 and Fig. 4.7.

To compare the results from our previous simulation with the modal theory, we

numerically propagated the vortex field given by Eq. (4.6) for the first n=10 terms by

using Eq. (3.5). We repeated the simulations for values of Δm ranging from 0 to 1, and

the amplitude and phase profiles in the plane $z=z_R$ are shown in Fig. 4.9 for $\Delta m <0.5$ and

are shown in Fig. 4.10 for $\Delta m >0.5$. As Δm was increased, a distortion appeared in the

phase of the beam accompanies by an amplitude depression (see Fig. 4.9(c-f)). As Δm

was further increased, this secondary defect gained topological charge forming an

additional unity charged vortex in the beam when $\Delta m \approx 0.5$ (see Fig. 4.10(a-d). The

secondary defect also moved closer to the center of the beam as Δm was increased

forming a charge 2 vortex at the beam center when $\Delta m=1$ (see Fig. 4.10 (e,f). As may be

seen by comparing Fig. 4.6 and Fig. 4.7 with Fig. 4.9 and Fig. 4.10 respectively, the

modal theory and the simulations of a vortex DOE qualitatively agree. Therefore, we

believe the presence of the second vortex may be explained by the interference of various

vortex modes described by Eq. (4.7).

4.3.3 Experimental Measurements

In order to validate the modeled spectral attenuation properties of an OVCF, we

performed an experiment with the apparatus depicted in Fig. 4.11. Broadband light from

a halogen bulb was sequentially passed through two apertures placed a distance

S=41.5cm apart. The first aperture, Ap_1, had a radial size R_s=0.25mm and the second

aperture, Ap_2, had a radial size w=2.5mm. Because of the small size of R_s, the beam at

incident on Ap_2 was considered spatially coherent since the coherence length is inversely

proportional to the aperture size ($L_c \propto \left(1/R_s\right)$)[149] (See Appendix A). Lenses L_1 and L_2

imaged Ap_2 with unity magnification onto an N=8 vortex DOE. Our vortex DOE was

composed of fused silica glass and was designed to produce a vortex of charge $m=1$ at

$\lambda_0=850$nm at an air interface. At a distance $z_d=92$mm from the mask the beam was

imaged onto a Meade Pictor model 416XT astronomical camera using lenses L_3 and L_4.

Spectral band-pass filters with bandwidths of $\delta\lambda=50$nm and mean transmitted

wavelengths ranging from, $\lambda_{ave}= 450$nm-855nm, were placed in front of the camera and

images were taken with each filter in place.

Several experimental images are shown in Fig. 4.12. When $\Delta\lambda=0$ a dark central

core forms in the intensity pattern of the beam and no secondary defect is visibility (see

Fig. 4.12(a)). However, when $\Delta\lambda=\lambda_0/8$ the intensity depression of a secondary defect is

visible at the edge of the beam (see Fig. 4.12 (b)). As $\Delta\lambda$ is further increased the

secondary defect moves closer to the vortex core (see Fig. 4.12 (c)). The two defects

merge to form the core profile of an $m=2$ vortex when $\Delta\lambda=\lambda_0/2$ (see Fig. 4.12(d)). The

radial position of the secondary defect was measured as a function of the wavelength

mismatch, $\Delta\lambda$ and is plotted in Fig. 4.13 (data points). To compare the experiment with

theory we numerically modeled the field transmitted through an N=8 vortex DOE after

the light had propagated a distance z=z_d. The radial position of the secondary defect in

the numerical model results was measured as a function of $\Delta\lambda$ and the resulting graph is

plotted in Fig. 4.13 (dashed curve). A comparison of the two curves in Fig. 4.13 show

that the numerical model and the experimental results qualitatively agree. A least squares

fit of the experimental plot in Fig. 4.13 (solid curve) suggest that the radial position of the

fractional vortex may be given by,

$$r = r_0\left(1 - 3.7\left(\Delta\lambda/\lambda_0\right)^2\right) \qquad (4.8)$$

where r_0 is the initial radial position of the fractional vortex upon creation. This equation may be used to determine how close the fractional vortex will form to the center of the beam, so that we may calculate the expected attenuation an OVCF will produce at a given wavelength.

4.4 Conclusions

In conclusion, in this chapter we have demonstrated that an OVCF may be used to null a coherent source of light. The attenuation of a primary beam was shown to depend on the charge of the vortex created by the vortex DOE and the size of the aperture used in the OVCF. We also demonstrated that the attenuation properties of an OVCF depended on the spectrum of the light we wish to filter. For a DOE designed to produce an m=1 vortex, the shape of the dark central vortex core was deformed and shifted off-center as we increased the wavelength mismatch between the incident light and the wavelength the DOE was intended for. However, for wavelength mismatches between 0-$\Delta\lambda/2$, a polychromatic null could be formed for aperture sizes greater than 0.3 times the beam size. This effect was explained by the formation of fractional vortices, which compensated for the misshapen vortex core. The propagation dynamics of fractional vortices were also explored and we demonstrated that the radial position of the fractional vortex is proportional to the wavelength mismatch squared. This may be useful in determining the attenuation of light with wavelengths that we do not measure a priori.

Vortex DOE   Lens   Aperture

Incident Light

f
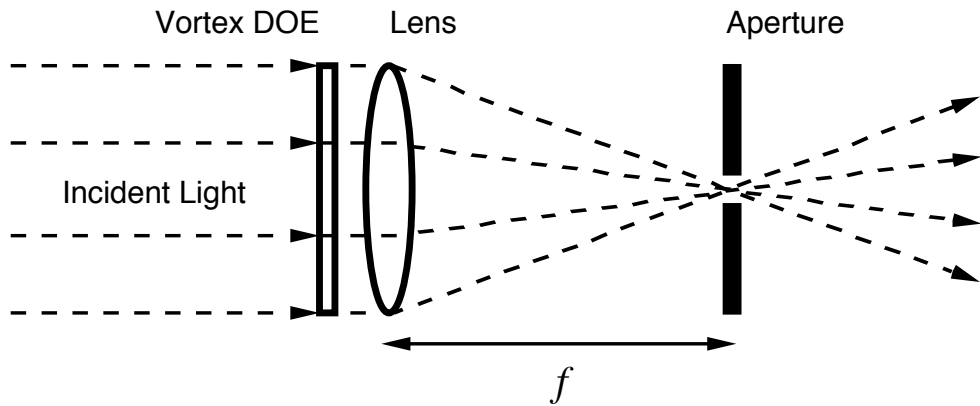
FIG. 4.1   Diagram of an optical vortex coherence filter. Collimated light we wish to filter is incident from the left onto a vortex DOE placed at the entrance pupil of an imaging lens. The light then comes to focus a distance f onto an aperture. The vortex DOE creates a dark null at the center of the focused beam in spatially coherent light. The aperture then blocks out light outside the vortex core region thereby filtering out spatially coherent light.
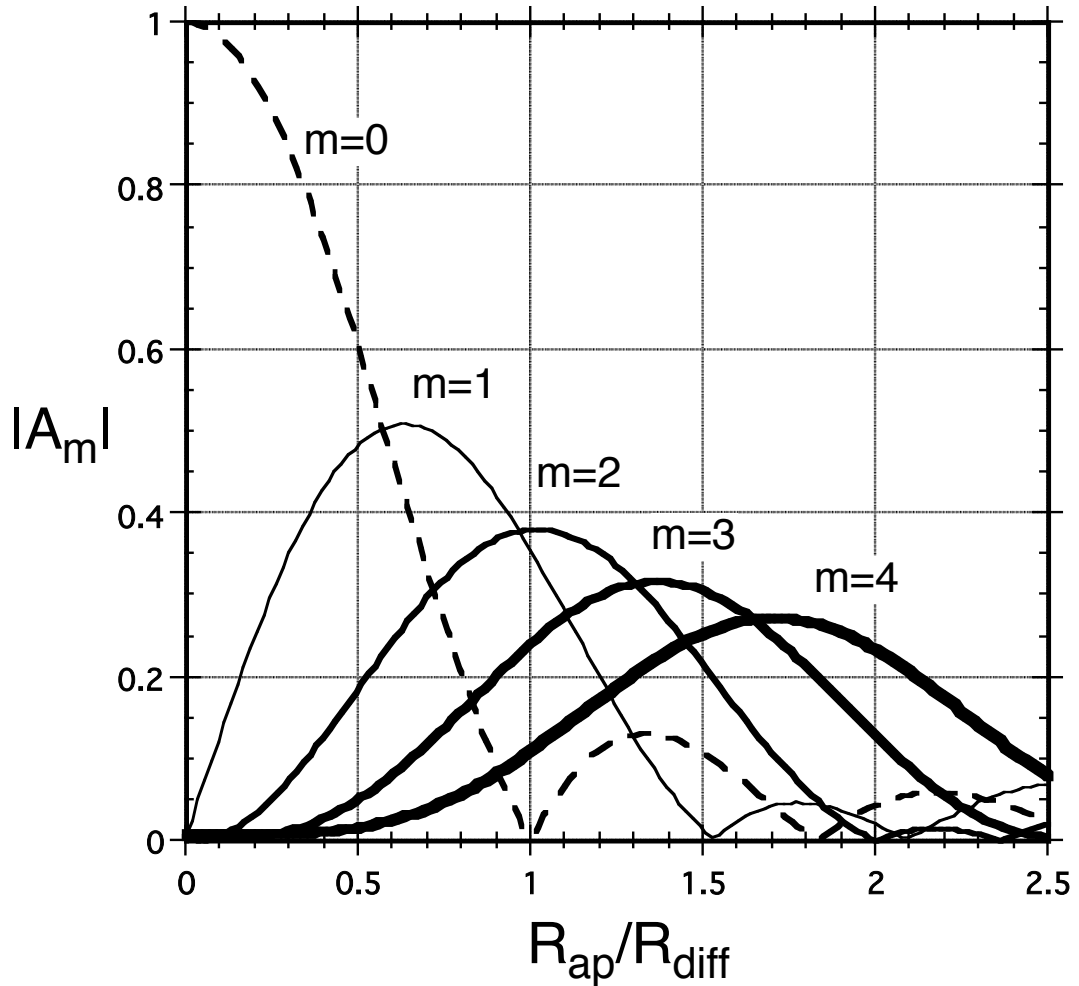
FIG. 4.2   Radial line plots of the amplitude in the focal plane for beams containing

vortices of charge |m|=0-4. As the value of |m| is increased the vortex core increases in

radial size and becomes flatter near r=0. The m=0 case corresponds to the familiar Airy

disk profile with the first amplitude zero at R_{diff} [140].
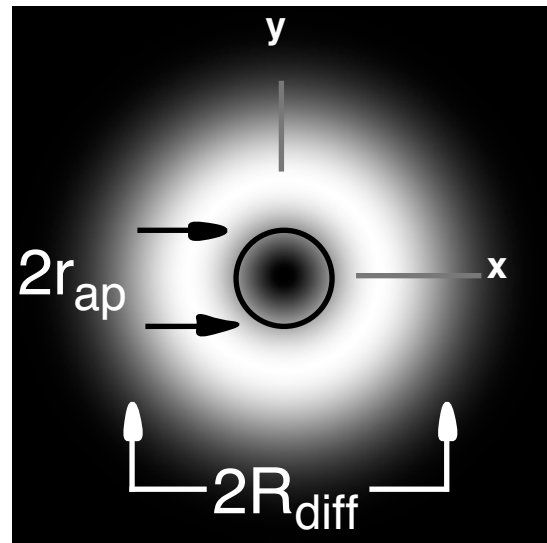
FIG. 4.3   Filtering of light by an optical vortex. A filtering aperture of radius r_{ap} is
placed in the vortex core of beam of radial size R_{diff}. The aperture blocks the intense light
outside the aperture only allowing the low intensity light in the vortex core to transmit.
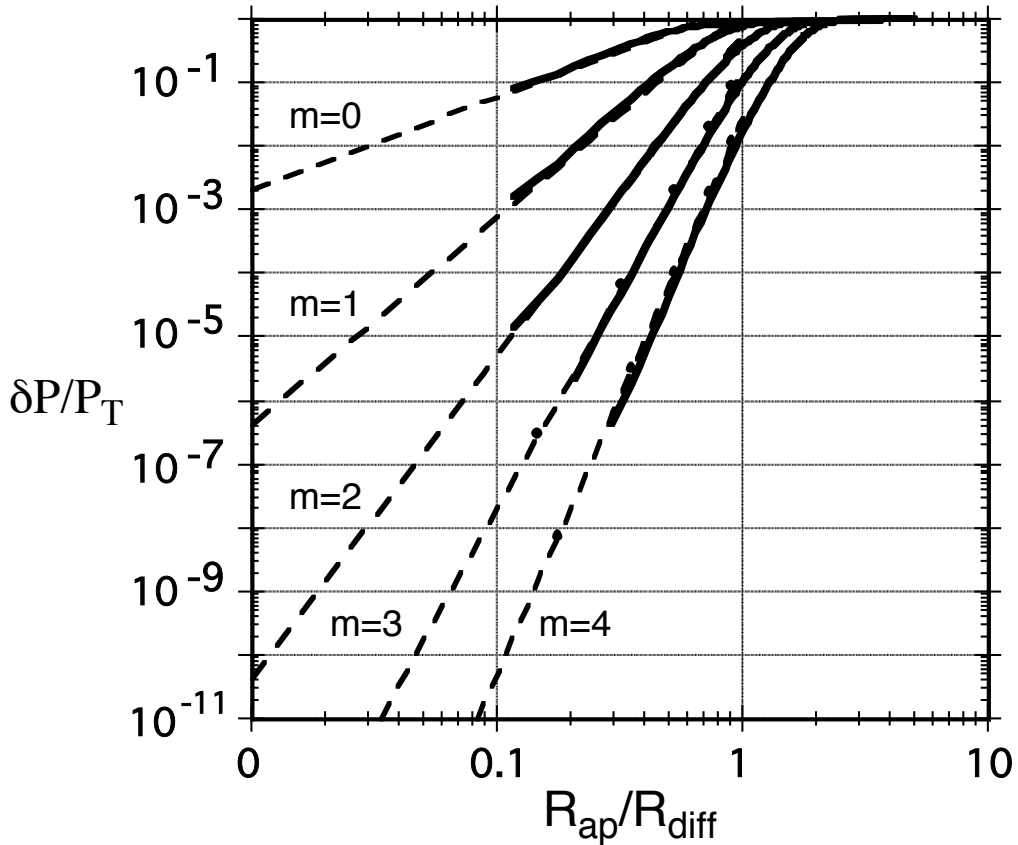
FIG. 4.4   Fraction of the total power transmitted through an optical vortex coherence filter (OVCF). The dashed curves are predictions from a least squares fit analysis for values of topological charge, |m|=0-4. The fraction of total power transmitted may be decreased by either decreasing the size of the aperture in the OVCF or by increasing the topological charge |m| of the vortex [140].
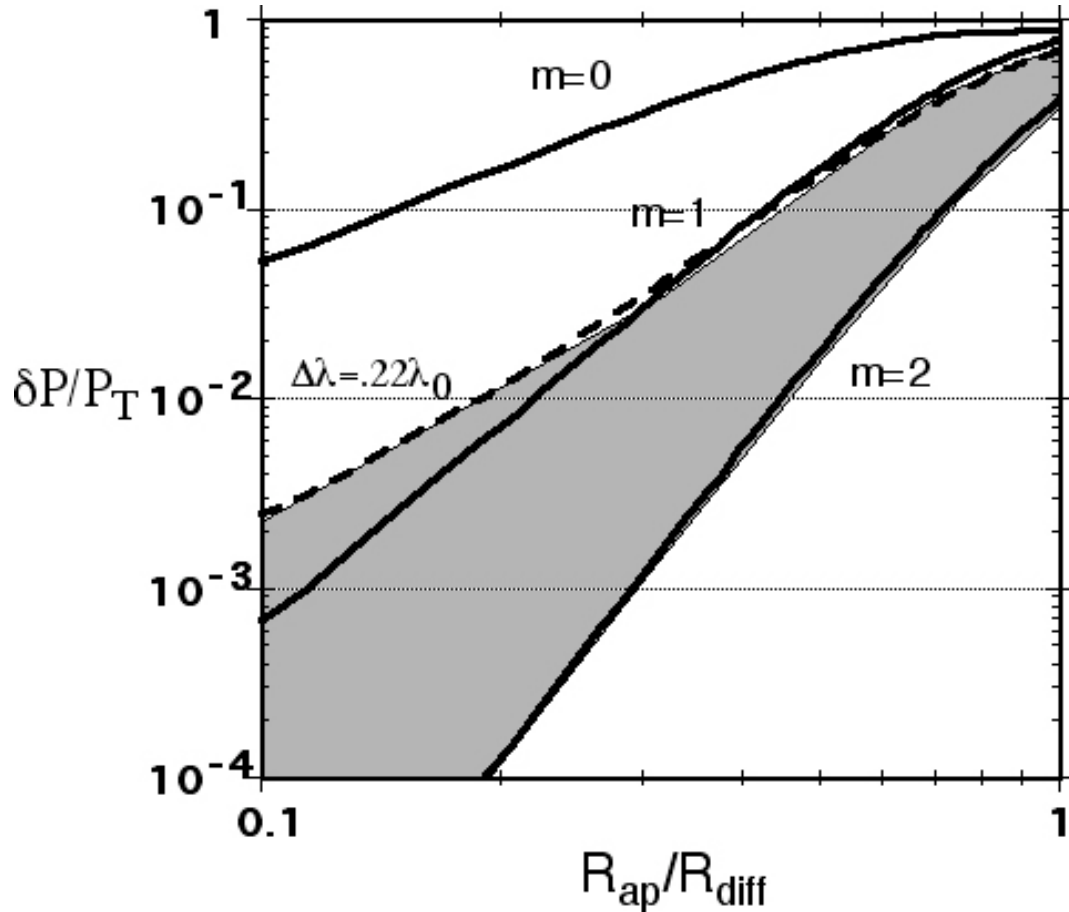
FIG. 4.5   Fraction of the total power of a polychromatic beam transmitted through an optical vortex coherence filter (OVCF). When the wavelength of the incident light is mismatched by an amount from the intended wavelength, λ_0, by an amount $\Delta\lambda$, the attenuation curves lay in the gray region. The attenuation created by the OVCF is is at least more than the attenuation expected if $R_{ap} > 0.3 R_{diff}$. The attenuation curves are degraded for smaller aperture sizes, with the largest degradation occurring at $\Delta\lambda = 0.22\lambda_0$.
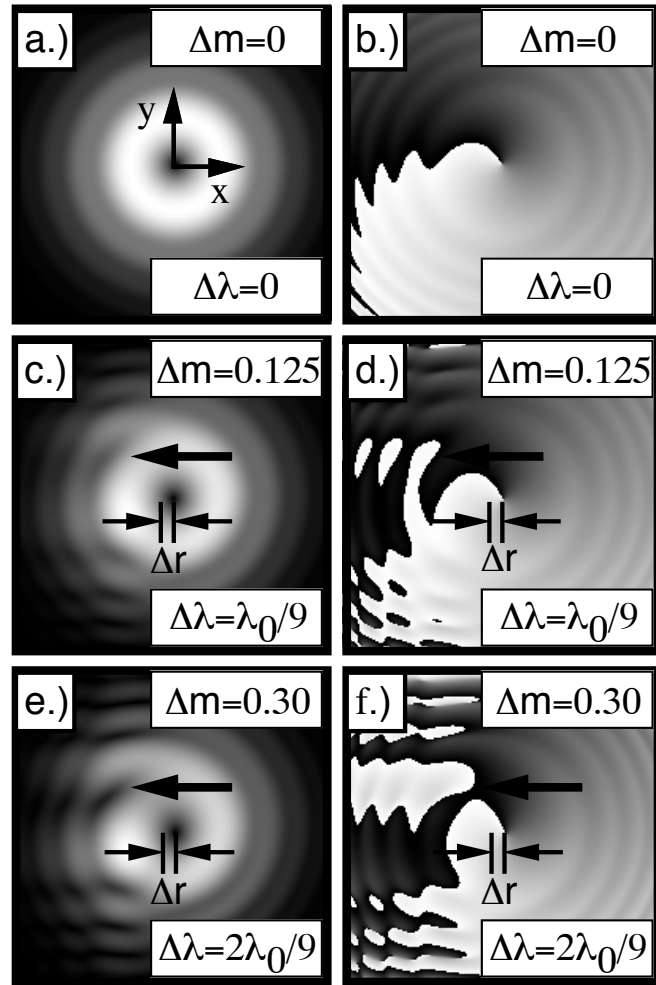
FIG. 4.6   A beam of light transmitted through an ideal m=1 vortex DOE intended

for use at a wavelength of λ_0. The images depict the amplitude (a,c,e) and phase (b,d,f)

profiles a distance $z=z_R$ away from the mask when the wavelength mismatch,

$\Delta\lambda$, between the incident light and λ_0 is changed from 0 to $2\lambda_0/9$. When $\Delta\lambda=0$ (a,b) the

beam contains an m=1 vortex. As $\Delta\lambda$ is made larger a secondary phase defect forms in

the beam indicated by an arrow (c-f).
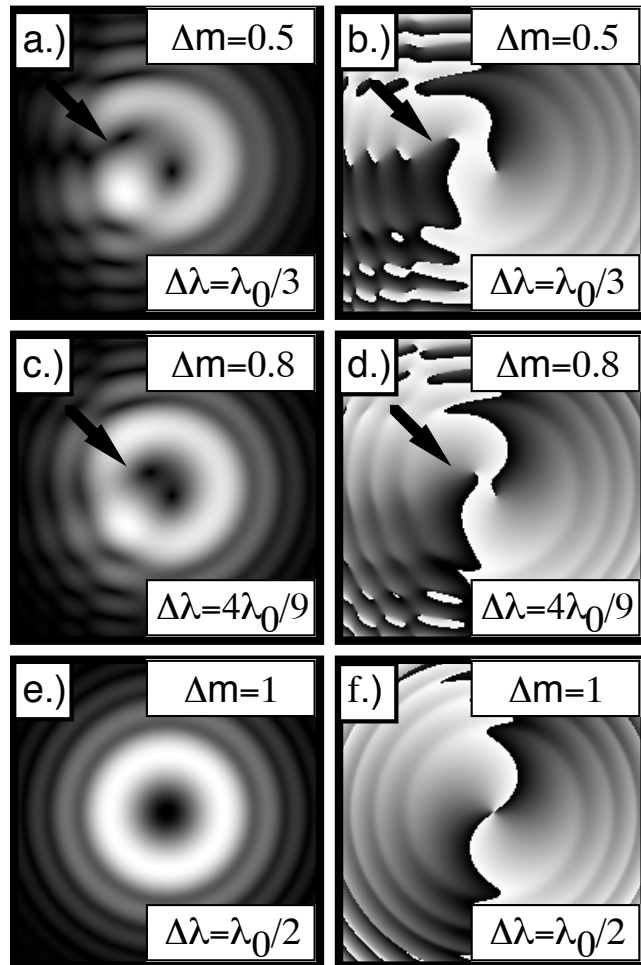
FIG. 4.7   A beam of light transmitted through an ideal m=1 vortex DOE intended for use at a wavelength of λ_0. The images depict the amplitude (a,c,e) and phase (b,d,f) profiles a distance $z=z_R$ away from the mask when the wavelength mismatch, $\Delta\lambda$, between the incident light and λ_0 is increased from $\lambda_0/3$ to $\lambda_0/2$. As $\Delta\lambda$ is increased a second vortex is seen in the beam indicated by an arrow (a-f) moving closer to the primary vortex. When $\Delta\lambda = \lambda_0/2$ (e,f) the second vortex joins with the primary vortex to form an m=2 vortex.
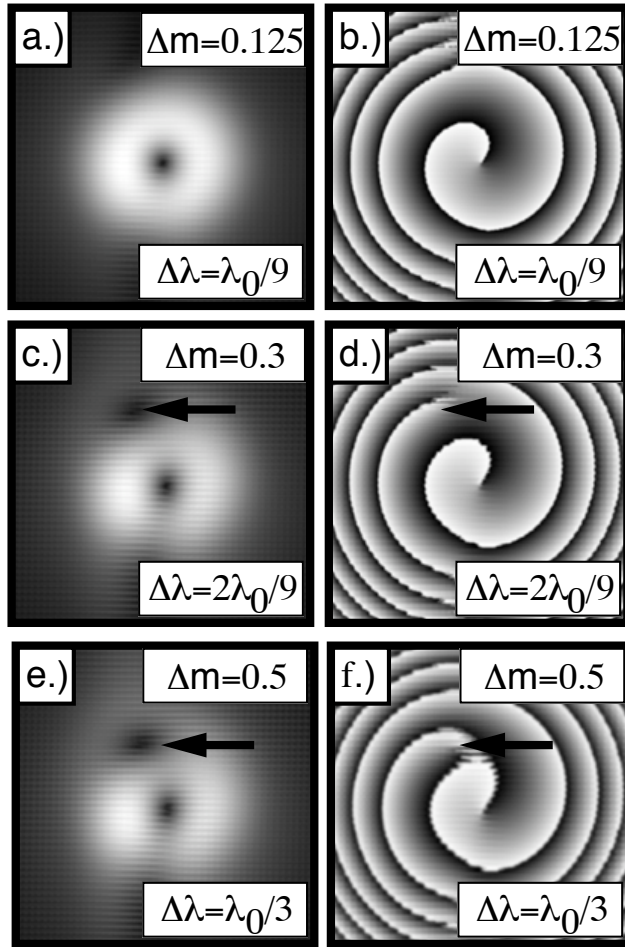
FIG. 4.8   A beam of light transmitted through an ideal m=1 vortex DOE intended

for use at a wavelength of λ_0. The images depict the amplitude (a,c,e) and phase (b,d,f)

profiles a distance $z=10z_R$ away from the mask when the wavelength mismatch,

$\Delta\lambda$, between the incident light and λ_0 is increased from $\lambda_0/9$ to $\lambda_0/3$. When $\Delta\lambda=\lambda_0/9$ (a,b)

the secondary defect no longer appears at the center of the beam. However, when

$\Delta\lambda>2\lambda_0/9$ (c-f), the secondary defect has evolved into a unity charged vortex.
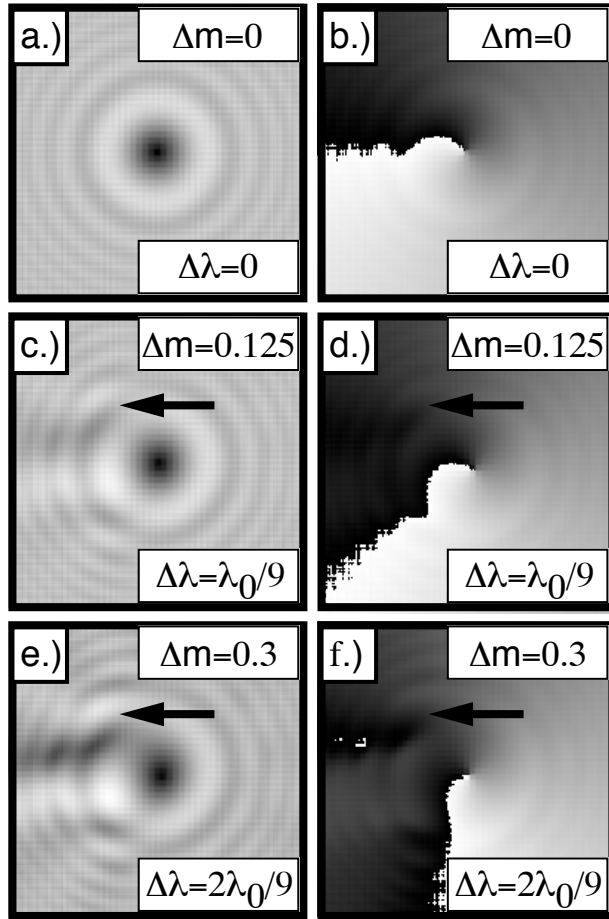
FIG. 4.9   A mode model representation of a beam of light transmitted through an ideal m=1 vortex DOE intended for use at a wavelength of λ_0. The images depict the amplitude (a,c,e) and phase (b,d,f) profiles a distance $z=z_R$ away from the mask when the wavelength mismatch, $\Delta\lambda$, between the incident light and λ_0 is increased from 0 to $2\lambda_0/9$. When $\Delta\lambda=0$ (a,b) the beam contains an m=1 vortex. As $\Delta\lambda$ is increased a secondary phase defect forms in the beam indicated by an arrow (c-f).
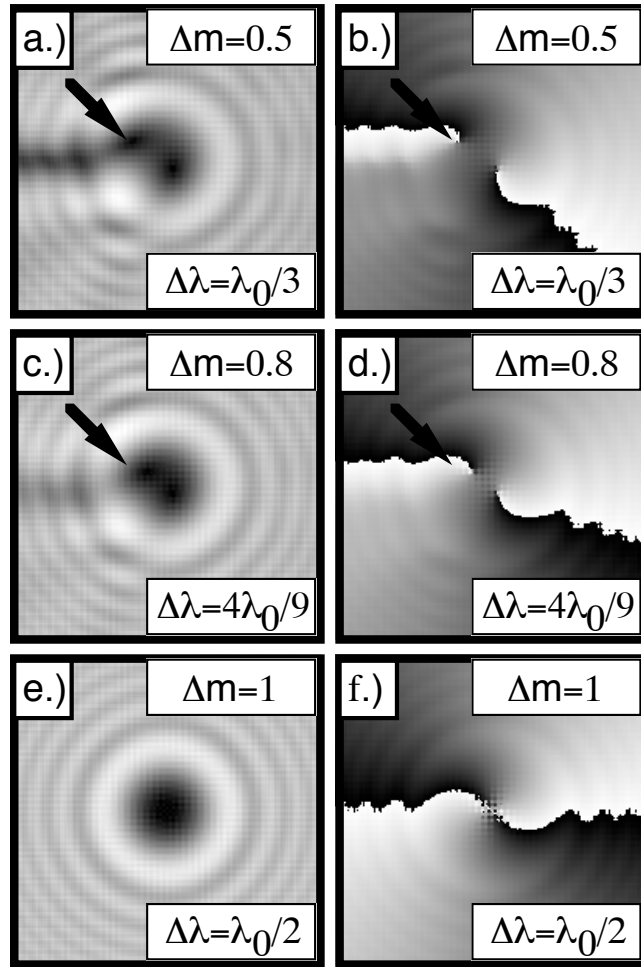
FIG. 4.10   A mode model representation of a beam of light transmitted through an ideal m=1 vortex DOE intended for use at a wavelength of λ_0. The images depict the amplitude (a,c,e) and phase (b,d,f) profiles a distance $z=z_R$ away from the mask when the wavelength mismatch, $\Delta\lambda$, between the incident light and λ_0 is increased from $\lambda_0/3$ to $\lambda_0/2$. As $\Delta\lambda$ is increased a second vortex is seen in the beam indicated by an arrow (a-d) moving closer to the primary vortex. When $\Delta\lambda = \lambda_0/2$ (e,f) the second vortex joins with the primary vortex to form a charge m=2 vortex.
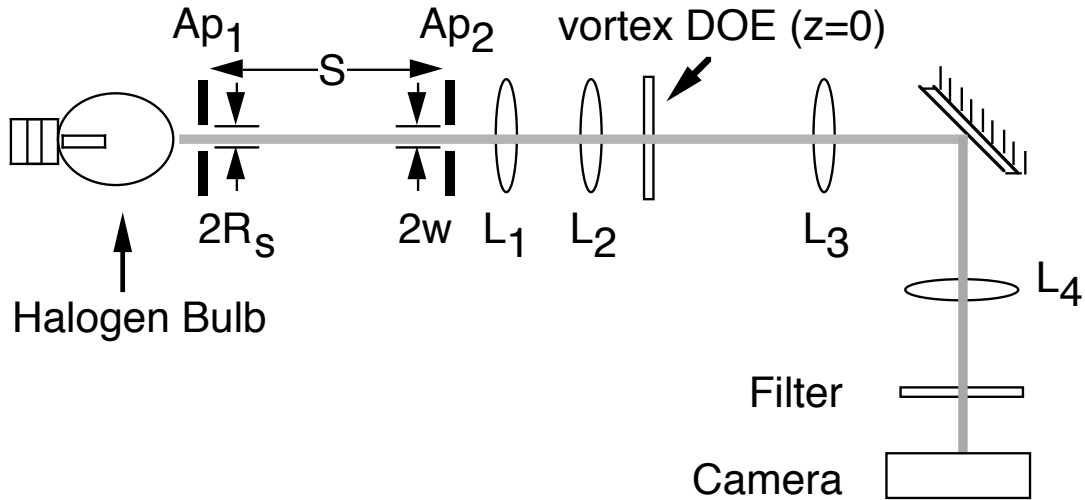
FIG. 4.11   The experimental setup. White light from a halogen bulb was passed

through two apertures (Ap_1 and Ap_2) separated by a distance S=41.5cm. The first

aperture had a size r_{ap}= 0.25mm and controlled the spatial coherence of the light in the

Ap_2 plane. The second aperture had a size, w=2.5 mm and was imaged by lenses L_1 and

L_2 with unity magnification onto an N=8 stepped vortex DOE in the plane z=0. Lenses

L_3 and L_4 then imaged the z=92.5mm plane onto a Meade Pictor CCD camera after the

light was transmitted through various 50 nm band-pass filters.
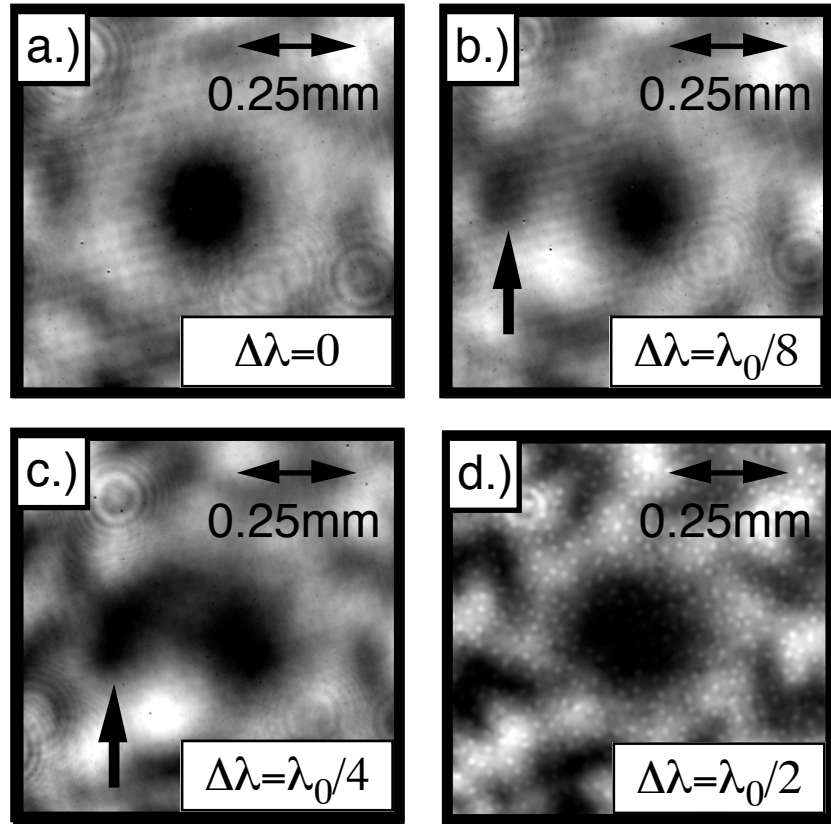
FIG. 4.12   Experimental images. The intensity of a beam of light transmitted through an N=8 vortex DOE intended to produce an m=1 vortex at a wavelength of λ_0=855nm. The images depict the intensity a distance z=92mm away from the DOE when the wavelength mismatch, $\Delta\lambda$, between the incident light and λ_0 is increased from 0 to $\lambda_0/2$. When $\Delta\lambda$=0 (a) the beam contains an m=1 vortex. As $\Delta\lambda$ is increased a secondary phase defect forms in the beam indicated by an arrow (b,c). When $\Delta\lambda=\lambda_0/2$ (d) the secondary phase defect and the primary vortex core merge and the beam contains an m=2 vortex.
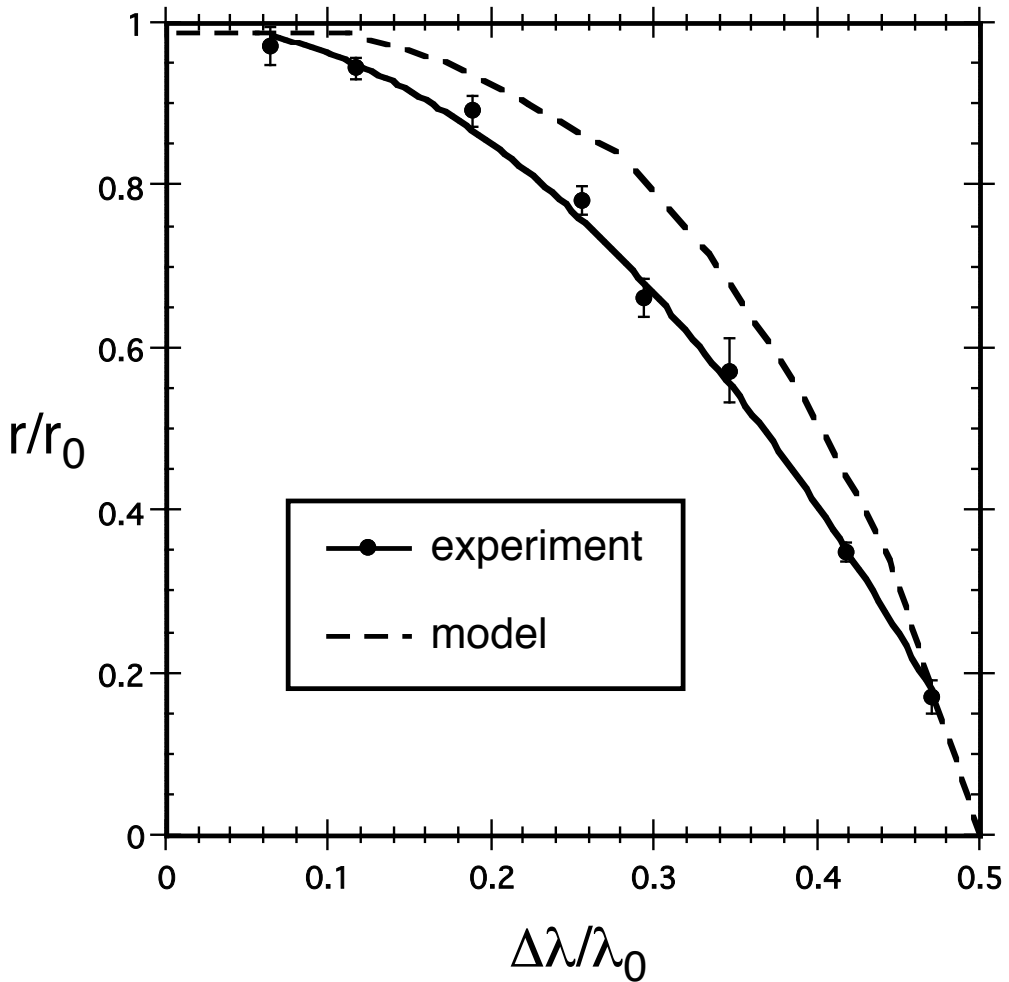
FIG. 4.13   A plot of the radial position of the secondary defect as a function of the wavelength mismatch, $\Delta\lambda$, between the wavelength of light that is incident on a vortex DOE and the wavelength, λ_0, intended for use with the DOE. The radial position, r, is normalized to r_0, the radial position of the secondary defects initial creation, and $\Delta\lambda$ is normalized to λ_0. The data points are experimental result and a solid line is a least squares fit. As a comparison the radial position computed from a numerical model is shown as a dashed curve.

5. Optical Vortices in Partially Coherent Light

5.1 Introduction

The space-time evolution of a wave is governed by its phase front topology. A wave having a helical phase front may be called a "vortex wave" owing to the circulation of momentum around the helix axis [2]. Vortex waves are known to occur in coherent systems having a well-defined phase, but are ill defined in partially coherent systems where statistics are required to quantify the phase. In the incoherent limit neither the helical phase nor the characteristic "eye" in the intensity profile is observable. Here we explore the vortex state and its statistical properties when the beam has arbitrary spatial coherence.

Optics affords a convenient means to vary the spatial coherence properties by changing the apparent size of an incoherent source as viewed in the detection plane. Recently, several groups have explored the theoretical and practical properties of optical vortices formed in partially coherent light. Certain classes of partially coherent beams carefully constructed to carry optical vortex modes have been examined analytically [120-127] and experimentally [128]. Zeros with [131] and without [132] a vortex phase structure were predicted to occur in the two-point correlation function.

In this chapter, we will use experimental and numerical techniques to explore how a beam transmitted through a vortex phase mask changes as the transverse coherence length at the input of the mask is changed. We assume a quasi-monochromatic,

statistically stationary light source and ignore temporal coherence effects. We demonstrate that although the characteristic dark core of a vortex fills with diffuse light with decreasing coherence, robust attributes of the vortex remain in the beam, most prominently in the form of a ring dislocation in the cross-correlation function.

5.2 A Partially Coherent Vortex Field

Spatial coherence refers to how well correlated two points along a wavefront are. A beam of light may be said to be spatially coherent if the light emitted across the area of the source is emitted in phase. An example of a spatially coherent source is a laser beam. A beam of light may be said to be spatially incoherent if light emitted across the area of the source is emitted randomly out of phase. For instance, a light bulb is an example of an incoherent light source. One property of light that is directly affected by spatial coherence is the beam spread. A spatially coherent beam of light tends to spread very little as it propagates and that is why a laser beam may be shot across a room and still form a small spot on the opposite wall. However, a spatially incoherent light source tends to spread very much as it propagates and that is why a light bulb can fill a room with light. As we will demonstrate in this chapter, this property of light will have a direct effect on the detection of vortices in partially coherent systems. For the interested reader a more thorough discussion of coherence theory may be found in Appendix A.

For a coherent wave, a single optical vortex in a scalar beam may be described by Eq. (3.1) as we have done in previously. The vortex nature of the field is governed by the

phase factor, *exp(imφ)*, which at any fixed instant of time produces helical surfaces of

constant phase given by *mφ-kz=const*. Since the amplitude vanishes along the helix axis

(*r=0*) owing to destructive interference in the vicinity of the vortex core i.e., *A(0, z)=0*,

we expect spatial coherence will play a role in the formation of the vortex. For

computational simplicity in the discussion below we consider a vortex with the initial

field amplitude of a Laguerre-Gaussian mode [29]:

$$A(r, z = 0) = E_0 \ (r/w)^m \ \exp(-r^2/w^2)\exp(i\beta) \qquad (5.1)$$

where E_0 and w are the characteristic amplitude and beam size in the plane $z=0$, and β is

an arbitrary phase.

A partially coherent beam propagating through a vortex mask may be expected to

gain the characteristic vortex phase factor *exp(imφ)* even though the wave front is not

well-defined. For example, if we view an incoherent beam as an incoherent

superposition of coherent beams each having a random phase, $\tilde{\beta}$, then each coherent

beam will gain a vortex phase factor. A schematic diagram of a partially coherent beam

of light transmitted through a vortex mask is shown in Fig. 5.1. Here we assume an

incoherent source of diameter D_s a distance z_s from a vortex mask of radial size *w* in the

plane $z=0$. A measure of the spatial coherence of a single beam of light may be found by

calculating the mutual coherence function (MCF) [149] of the electric field for points in

the transverse plane, $\vec{r}_1$ and $\vec{r}_2$ (see Appendix A),

$$\Gamma(\vec{r}_1, \vec{r}_2) = \left\langle E(\vec{r}_1, t)E^*(\vec{r}_2, t) \right\rangle \qquad (5.2)$$

where $<>$ denotes a time average. We may assume the statistical distribution of the

phase, $\tilde{\beta}$, in the plane $z=0$ corresponds to a Carter-Wolf type light source having a

Gaussian-Schell correlator,

$$C\left(\left|\vec{r}_1 - \vec{r}_2\right|\right) = \exp\left[-\left|\vec{r}_1 - \vec{r}_2\right|^2 \big/ L_c^2\right] \tag{5.3}$$

where L_c is the transverse coherence length at $z=0$ (See Appendix A). This simply states

that the correlation between two points along the wavefront is only dependent on the

distance between the two points. Using Eqs. (5.1) and (5.2) the MCF may be written:

$$\Gamma(\vec{r}_1, \vec{r}_2) = C\left(\left|\vec{r}_1 - \vec{r}_2\right|\right)E_0^2\left|\vec{r}_1 \cdot \vec{r}_2 / w^2\right|^m \exp\left[-\left(r_1^2 + r_2^2\right)\big/w^2\right]\exp\left[-im(\phi_1 - \phi_2)\right] \tag{5.4}$$

The MCF in the detection plane (see Fig. 5.1) after the beam has propagated a distance z_d

is given by [149],

$$\Gamma'(\vec{r}_1', \vec{r}_2') = a \iint \iint \Gamma(\vec{r}_1, \vec{r}_2)\rho_1^{-3}\rho_2^{-3}(1 - ik\rho_1)(1 + ik\rho_2)\exp\left[ik(\rho_1 - \rho_2)\right]d\vec{r}_1 d\vec{r}_2 \tag{5.5}$$

where $\rho_i = \left[\left|\vec{r}_i' - \vec{r}_i\right|^2 + z_d^2\right]^{1/2}$ $(i=1,2)$ and $a = z_d^2 / 4\pi^2$. As we will show, the most striking

statistical feature of a propagated vortex formed in a partially coherent beam is that the

cross-correlation function, $\chi'(\vec{r}') \equiv \Gamma'(\vec{r}_1', -\vec{r}_1')$, is a more robust pattern than the intensity

(the auto-correlation function), $I'(\vec{r}') \equiv \Gamma'(\vec{r}_1', \vec{r}_1')$.

5.3 Cross-Correlation Singularities

A geometric description of rays passing through various sectors of the mask will

serve to develop an understanding of the nature of the beam as it propagates. Consider

first the correlation function in the plane of the mask, $\Gamma(\vec{r}_1, \vec{r}_2)$. According to Eq. (5.4),

the points $\vec{r}_1$ and $\vec{r}_2$ are positively correlated (i.e. $\mathrm{Re}\left[\Gamma(\vec{r}_1, \vec{r}_2)\right]$ >0) if the phase difference

between them obeys the relation, $m|\phi_2 - \phi_1| \le \pi/2$; otherwise, the points are anti-

correlated (i.e $\mathrm{Re}\left[\Gamma(\vec{r}_1, \vec{r}_2)\right]$<0). Note that if the mask is removed (i.e. if m=0), $\Gamma(\vec{r}_1, \vec{r}_2)$ is

everywhere real and positive. Let us now examine light in the plane $z=z_d$. This

correlation/anti-correlation distinction is carried with the beam as it propagates and may

be geometrically described as a conical projection of the light source through the center

of the mask. This cone defines a circle, shown in the (x', y') plane in Fig. 5.1, forming a

correlation/anti-correlation boundary. To clarify this point let us examine the cross-

correlation function $\chi(\vec{r}) \equiv \Gamma(\vec{r}_1, -\vec{r}_1)$. for various rays transmitted through the phase

mask to the detection plane as depicted in Fig. 5.1. In the case of light outside the conical

projection (points A and B in Fig. 5.1(a)), the light may be described by a superposition

of rays that have all passed through nearly the same sector of the mask. Thus on average

the field at point A and B will each gain phase shifts from opposite sides of the mask.

Therefore, for these two points, $\mathrm{Re}\left[\Gamma(\vec{r}_1, \vec{r}_2)\right]$<0. Let us now examine a point inside the

conical projection of the light source, for example point C shown in Fig. 5.1(b). The light

inside this region may be described by a superposition of rays that have passed through

all sectors of the mask. Accordingly, the field in this area will gain a phase shift of $m\pi$

from the phase mask and for two points inside the conical projection, $\mathrm{Re}\left[\Gamma(\vec{r}_1, \vec{r}_2)\right]$>0 .

Therefore, there appears to be a (+/-) correlation boundary that forms in a partially

coherent beam of light passed through a vortex phase mask. The size of this boundary

may be expected to increase with increasing beam spread, and thus it depends on both the

size of the source (as evident in Fig. 5.1) and the diffraction properties of the system.

This correlation/anti-correlation boundary may be shown to persist to the far-field

$(z_d >> kw^2/2)$ where the MCF is given by [150],

$$\Gamma'(\vec{f}_1, \vec{f}_2) = (1/\lambda z_d)^2 \iint \iint \Gamma(\vec{r}_1, \vec{r}_2) \exp\left[-i2\pi\left(\vec{f}_1 \cdot \vec{r}_1 - \vec{f}_2 \cdot \vec{r}_2\right)\right] d\vec{r}_1 d\vec{r}_2 \qquad (5.6)$$

where $\vec{f}_i = \vec{r}_i'/\lambda z_d$ (i=1,2). Numerical integration of Eq. (5.6) allows us to visualize the

far-field intensity distribution, $I'(\vec{f}) \equiv \Gamma'(\vec{f}_1, \vec{f}_1)$. The case $m=1$ is shown in Fig. 5.2(a,b,c)

for different states of coherence. The high coherence case produces a dark vortex core

with a minimum intensity that is close to zero as expected. In the partial and low

coherence cases, the core fills with diffuse light. In contrast, the far-field cross-

correlation function, $\chi'(\vec{f}) \equiv \Gamma'(\vec{f}_1, -\vec{f}_1)$, shown in Fig. 5.2(d,e,f), maintains attributes of

a singularity as the spatial coherence is decreased. In each case, $\chi'(\vec{f})$ exhibits a ring

phase dislocation of radius, f_r, that is characterized by a π phase step across the circular

boundary where $\chi'(\vec{f})$ is zero. Inside (outside) the ring the numerical value of

$\mathrm{Re}\left[\chi'(\vec{f})\right]$ is positive (negative).

5.4 Experimental Measurements

At any distance, z_d, the spatial distribution of $\mathrm{Re}\!\left[\chi'(\vec{r}')\right]$ may be obtained with the aid of a wavefront folding (WFF) interferometer [151]. The expected interferogram is given by,

$$F(x',y') = I(-x',y') + I(x',-y') + 2\mathrm{Re}\!\left[\left\langle E(-x',y')E^*(x',-y')\right\rangle\right]\cos\!\left(\Delta\vec{k}_\perp \cdot \vec{r}'\right) \quad (5.7)$$

where $\Delta\vec{k}_\perp$ is difference between the wave vectors of the two beams emerging from the interferometer. Owing to the symmetry of our system, $E(-x',y')=E(x,y)exp(i\pi)$ and $E(x,-y)=E(-x,-y)exp(i\pi)$; hence the cross-term in Eq. (5.7) becomes $2\mathrm{Re}\!\left[\chi'(\vec{r}')\right]\cos\!\left(\Delta\vec{k}_\perp \cdot \vec{r}'\right)$. The magnitude and phase of $\mathrm{Re}\!\left[\chi'(\vec{r}')\right]$ is found by measuring the fringe visibility and deformation, respectively. At the boundary of a ring dislocation in $\chi'(\vec{r}')$ the fringe visibility is expected to vanish and the π phase shift across the boundary turns bright fringes dark.

We obtained the cross-correlation function of a vortex beam with the apparatus shown in Fig. 5.3. Broadband light from a halogen bulb was passed through two apertures placed a distance S=41.5cm apart. The spatial coherence of the source was controlled by varying the size of the aperture, Ap_1. Assuming the beam in the Ap_1 plane is spatially incoherent, the transverse coherence length in the second aperture plane is approximately given by, $L_c = .64\lambda_{ave}S/R_s$, where λ_{ave} is the average wavelength, and R_s is the radial size of Ap_1 [149]. The second aperture, Ap_2, had a radial size w=2.5mm. Lenses L_1 and L_2 imaged Ap_2 with unity magnification onto a vortex phase mask. Our

mask resembled a spiral staircase having sixteen steps, each differing in phase from its

adjacent neighbor by $\pi/8$. The fused silica mask was designed to produce a vortex of

charge $m=1$ at $\lambda_0=890$nm at an air interface, although as we showed in chapter 4, we

found it also produces an m=1 vortex at wavelengths shorter than 800nm. At a distance

$z_d =92$mm from the mask the beam was imaged onto a camera using lenses L_3 and L_4.

The WFF interferometer was created by placing Dove prisms, D_1 and D_2 in each arm of a

Mach-Zehnder interferometer. These prisms inverted the beam in one arm across the x-

axis $(E_1(x',y')=E(-x',y))$ and the other arm across the y-axis $(E_2(x',y')=E(x',-y'))$. A

Meade Pictor model 416XT astronomical camera recorded the interferograms. A 50nm

bandpass filter with a mean transmitted wavelength of $\lambda_{ave}=800$nm was placed in front of

the camera to eliminate temporal coherence effects (e.g., fringe fading).

During the experiment we varied R_s from 0.25mm to 1.5mm in 0.125mm steps

with a precision of ±0.005mm. At the largest transverse coherence length, the predicted

ring dislocation was barely detectable. As the value of R_s was increased the ring of zero

fringe visibility increased in size. Meanwhile the area of high fringe visibility (i.e. the

coherence area) decreased in size. We note that another ring dislocation attributed to the

Airy disk is expected to bound the coherence area [129]. From our experimental

interferograms, these rings coincided when $R_s= 0.89$mm (i.e. $L_c= 0.25$mm).

Two typical experimental images obtained with $R_s=0.5$mm (i.e. $L_c= 0.5$mm) may

be seen in Fig. 5.4(a) for m=1 and Fig. 5.4(b) for m=0. A ring of zero fringe visibility of

radial size, R', is seen within the coherence area in Fig. 5.4(a). Bright fringes inside the

ring are shifted to dark fringes outside the ring, indicating a π phase shift occurs across

the ring. A corresponding ring is not seen in Fig. 5.4(b). Although the intensity appears

lower inside the ring dislocation in Fig. 5.4(a), the value of the fringe visibility was

0.36±.05 (0.11±.05) inside (outside). This difference in fringe visibility qualitatively

agrees with the results shown in Fig. 5.2(f).

The average of five measurements made of R′ and L_c were calculated and plotted

in Fig. 5.5. The transverse coherence length, L_c was measured at the plane $z=0$ (shown in

Fig. 5.3) by removing the mask and then replacing lens L_4 with a 250mm focal length

lens, which imaged the plane $z=0$ onto the CCD camera. The ring radius R′ a distance z_d

from the mask may be approximated by [149]:

$$R'(z_d) = R(0) + (2\pi)^{1/2}(z_d / kL_c)$$ (5.8)

where $R(0)$ is the initial size of the ring in the mask plane. Ideally $R(0)=0$, but due to a

slight misalignment of the mask we measured $R(0)=.021$mm. As seen in Fig 5.5, we

have excellent agreement between the measured (data points) and predicted (solid line)

values of R′ at difference values of the coherence length.

The diffusion of light into the vortex core may be quantified by determining the

relative intensity compared to the maximum value:

$$\eta' = (I'_{max} - I'_{core})/(I'_{max} + I'_{core})$$ (5.9)

where I'_{core} is the measured intensity at $\vec{r}' = 0$ and I'_{max} is the recorded maximum intensity

at some other point in the profile ($\vec{r}' \neq 0$). We expect $\eta \to 1$ in the coherent limit, $L_c \to \infty$,

and $\eta \to 0$ in the incoherent limit, $L_c \to 0$. The average of five measurements of η, plotted

in Fig 5.5(b), shows that as L_c decreases, the vortex becomes less conspicuous in the

intensity profile. As a qualitative measure, we may define a vortex as having a dark core

if $\eta \geq 0.8$. As shown in Fig. 5.5(b), by our qualitative measure the vortex no longer possesses a distinct dark core when $L_c < 0.5$mm. However, as shown in Fig. 5.5(a), the ring dislocation in $\chi'(\vec{r}')$ is still detected when $L_c < 0.5$mm.

5.5 Conclusions

In conclusion, we find that although the dark core of an optical vortex diffuses and becomes inconspicuous in incoherent light, the cross-correlation function maintains a ring dislocation that persists regardless of the size of the transverse coherence length. This ring dislocation was characterized by an island of positively correlated light, which increased in area with increased beam spread.
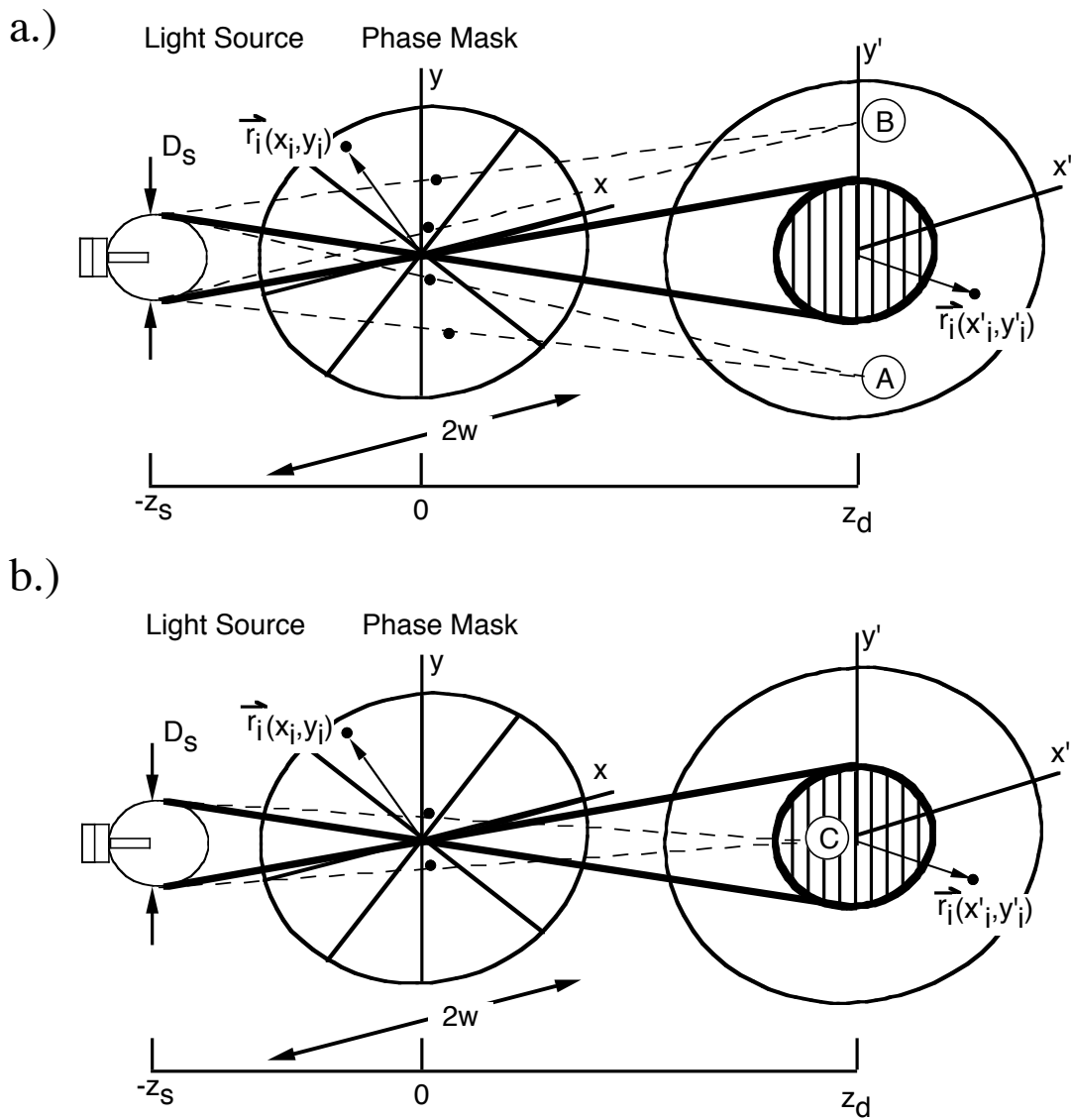
FIG. 5.1   A diagram of a partially coherent beam of light transmitted through a vortex mask of transverse diameter 2w. In the plane $z=z_d$ a conical projection of the source through the center of the mask forms an enclosed circular region. Light inside the circle (point C) contains rays from all sectors of the mask, but outside the circle (points A and B) the light contains rays from only adjacent sectors of the mask as depicted by the dashed lines.
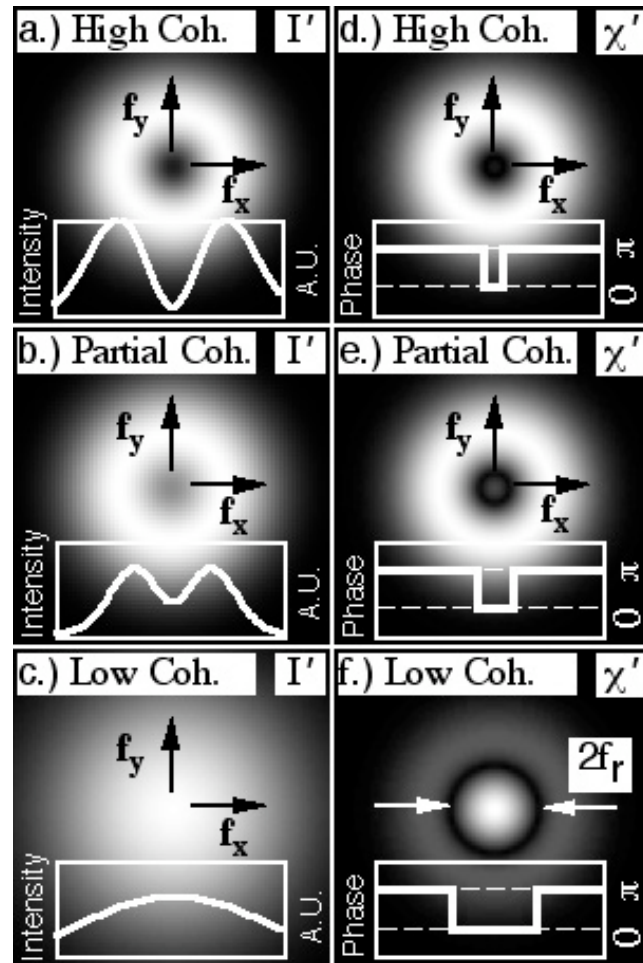
FIG. 5.2   Numerically computed intensity (a,b,c) and cross-correlation (d,e,f) functions for m=1 in the far-field plane for various coherence lengths. As the coherence decreases the dark vortex core fills with diffuse light. However, a ring dislocation persists in the cross-correlation function, and its radial size, f_r, increases with decreasing coherence.
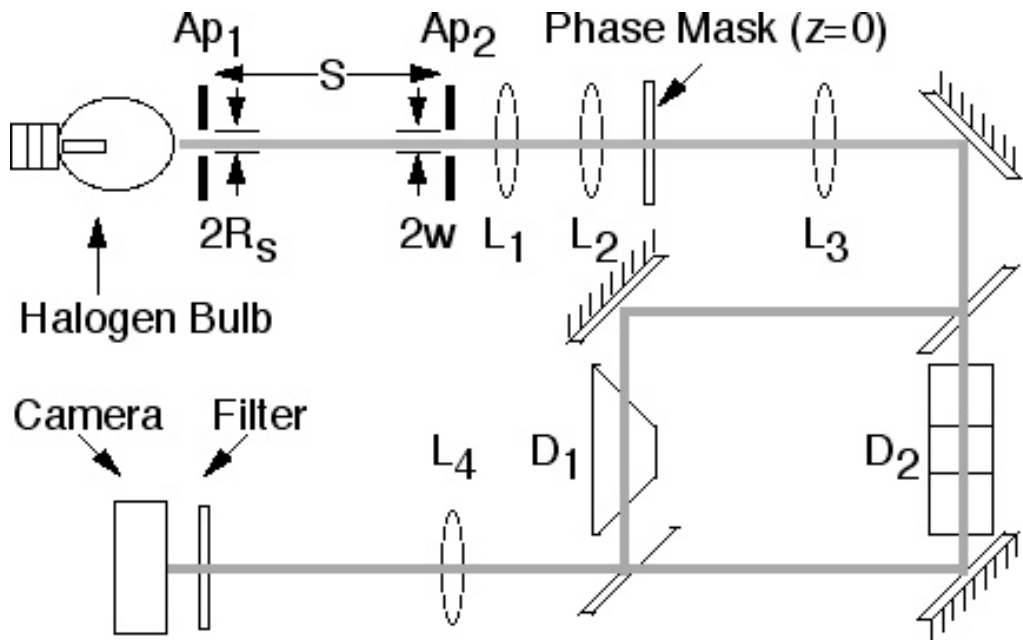
FIG. 5.3   A schematic diagram of the experiment showing light from a halogen bulb

with a mean wavelength of 800 nm and a bandwidth of 50 nm passing through two

apertures separated by a distance, S= 41.5cm. The Ap_2 plane was imaged with unity

magnification by two 50.2 mm focal length lenses (L_1 and L_2) onto a phase mask

designed to produce an m=1 vortex beam. The plane z=92mm was imaged with a

magnification of 3 by two lenses having focal lengths, f=125mm (L_3) and f=500 mm (L_4)

onto a CCD camera after passing through a wavefront folding interferometer comprising

Dove prisms, D_1 and D_2.
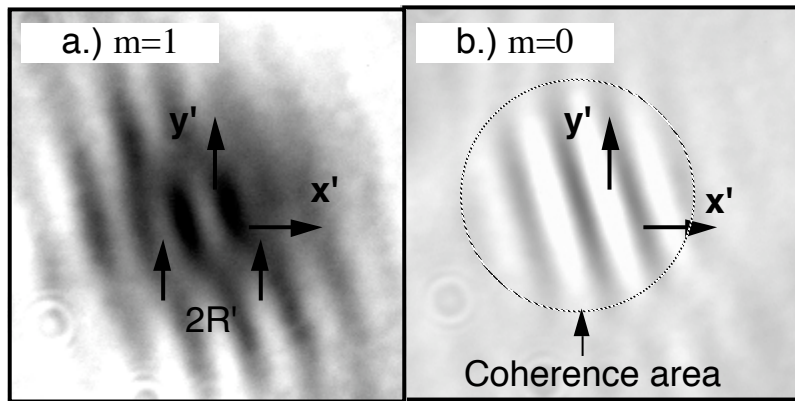
FIG. 5.4   Experimental interferograms of the cross-correlation function in the plane

z=540mm for an (a) m=1 vortex beam and (b) m=0 non-vortex beam (L_c/w=0.20 in both

cases). Shifted (a) and uniform (b) fringes indicate the respective presences and absences

of a ring dislocation of radial size, R'=0.08mm.
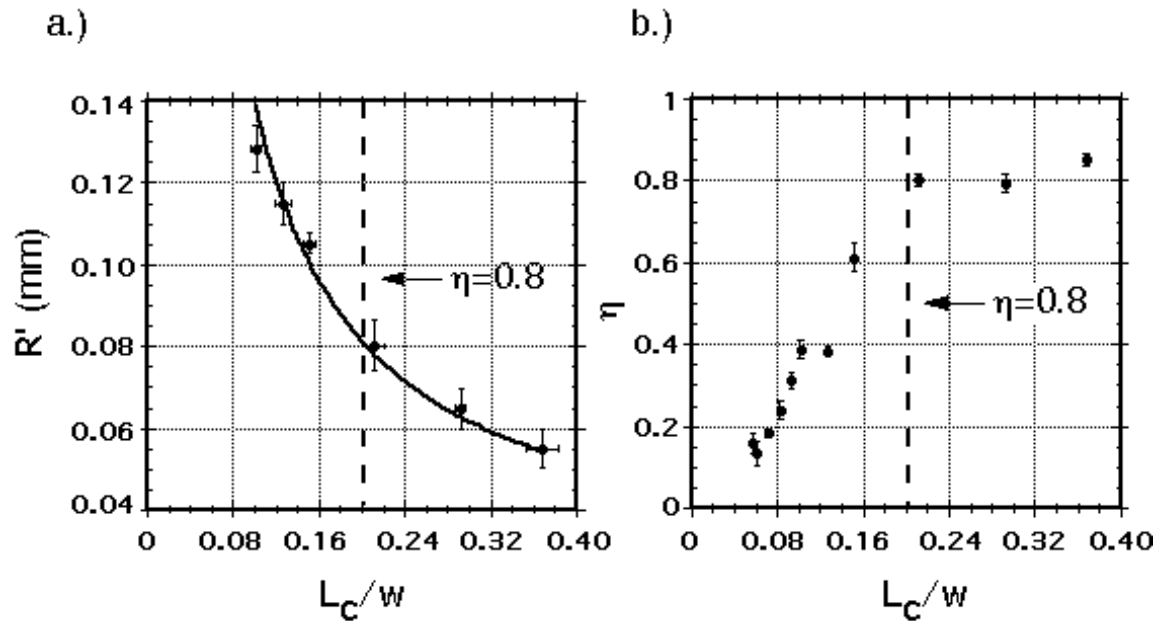
FIG. 5.5   A comparison of the visibility of the correlation singularity in the cross

correlation function and the visibility of the vortex. Since an optical vortex is designated

as a point where both the real and imaginary parts of a field are simultaneously zero, a

visibility of the vortex core less than .8 was considered a loss of vortex visibility. The

dashed lines show the point when the vortex would have a visibility of n=0.8 and would

no longer be distinguishable as an optical vortex. As can be seen by the comparison of

(a) and (b), under low coherence the correlation singularity is a more robust pattern than

the vortex core itself.

6. Application 1: The Detection of

Forward-Scattered Light

6.1 Introduction

When a laser beam is passed through a scattering medium containing particles larger than the wavelength, light is scattered in all directions. However, the most intense scattering usually occurs in the forward direction (see Fig. 6.1) [153, 154] (see Appendix B)]. Light scattered along the optical axis is often difficult to distinguish from the superimposed unscattered laser beam, especially when there is a dilute concentration of weak scatterers. If one were to measure the intensity of the scattered light as a function of the angle, θ, at which it is scattered (see Fig. 6.1), one may determine various properties of the scattering medium; such as the size, shape and density of particles in the medium [154]. In typical scattering experiments used to determine particle sizes, the intensity of the zero angle scattered light is orders of magnitude smaller than the beam intensity, and the signal is essentially lost in the glare of the beam. Non-existent or inaccurate zero angle scattering data pose problems for techniques that use the inverse scattering method to determine particle size distributions [155-157]. Thus a technique that nulls the coherent on-axis unscattered radiation may allow more accurate particle size determinations.

In this chapter we will demonstrate the utility of an optical vortex coherence filter in the detection of forward-scattered light. As I have stated previously, an optical vortex may be characterized as a dark channel of destructive interference, which nulls spatially

coherent light. Scattering, however, may superimpose other modes into the dark vortex

core region, shifting or brightening the core if the light is respectively coherent or

incoherent. The core may therefore be used as a window for a variety of applications to

detect scattered light without the blinding effects of the unscattered coherent source

[140].

6.2 Measurement of Forward-Scattered Light with an OVCF

In order to measure the on-axis scattered light the OVCF was placed in the laser

beam after the beam was first passed through a scattering cell as shown in Fig. 6.2. The

mask equally affects the phase of the scattered and unscattered light, but only the

spatially coherent components develop the intended vortex core. Assuming the incident

beam is spatially coherent, the field transmitted through both the scattering cell and an

ideal phase mask given by Eq. (3.4) may be written in the form:

$$E(r,\phi,z) = \left\{ A_{unsc}^{coh}(r,z) + A_{sc}^{coh}(r,\varphi,z) + A_{sc}^{incoh}(r,\varphi,z) \right\} \exp\left[-im(\lambda_0 / \lambda)\phi \right] \tag{6.1}$$

where *sc (unsc)* and *coh (incoh)* respectively indicate scattered (unscattered) and coherent

(incoherent) light. We ignore the phase factor, $\exp\left[-ikn_2 d_0 - ikn_1(z - d_0) \right]$. The complex

scattered amplitude functions have spatial distributions that depend on the shape and

concentration of scatterers, and they are generally time-dependent, e.g., owing to moving

particles or a finite coherence time of the laser [154].

For simplicity we assume the intensity centroids of each scattered beam coincide with the optical axis where $A_{unsc}^{coh}(r = 0, z) = 0$. The complex speckle field, A_{sc}^{coh}, formed from the coherent superposition of fields from many scatterers, may be highly structured. The vortex position may be shifted by intensity and phase gradients of the speckle; however, this effect may be negligible if the coherence area of A_{sc}^{coh} in the detection plane is smaller than a pixel. Thus we ignore A_{sc}^{coh} below. The term A_{sc}^{incoh} is a random variable. For the case $m(\lambda_0 / \lambda) = \pm 1$, the resulting time integrated intensity in the vicinity of the vortex core may be written

$$\left\langle |E(r\,\phi,z;t)|^2 \right\rangle = \left\langle |a_{unsc}^{coh}|^2 \right\rangle (r/w)^2 + \left\langle |A_{sc}^{incoh}|^2 \right\rangle + I_0^{incoh} \tag{6.2}$$

where we assume $\left\langle A_{sc}^{coh} \right\rangle = 0$ and $A_{unsc}^{coh} = a_{unsc}^{coh} r/w$ for $r << w$, where w is the characteristic size of the beam, and we have added the term I_0^{incoh} which is attributed to incoherent light from the laser source. Equation (6.2) shows that the incoherently scattered radiation can be directly measured by placing a small detector at the vortex center, r=0, when $I_0^{incoh} << \left\langle |A_{sc}^{incoh}|^2 \right\rangle$. This result may be generalized for a vortex core translated to any point in the beam, thereby allowing the angular measurement of the scattering spectrum as we will show in the next section (section 6.4).

Yang et al. estimated the far field concentration dependent incoherent scattering distribution for a few scattering events (see appendix B) [153], which we express as

$$\left\langle |A_{sc}^{incoh}|^2 \right\rangle \Big/ I_0^{coh} = \sum_j (C_j a_j / j!)(\rho/\rho_0)^j \exp(-\rho/\rho_0)\exp[-2.69 a_j(wr/\lambda z)^2] \tag{6.3}$$

where j is the number of times the light is scattered before emerging from the cell, the coefficients $0 \le C_j \le 1$ are coherence factors determined from experimental data,

$a_j = (1 + 0.273jw^2/w_s^2)^{-1}$, $\rho_0 = (\pi R^2 L)^{-1}$ is the scattering extinction parameter (L is the

length of the cell, and R is the particle radius), w is the radial size of the aperture near the

input face of the cell, $w_s = Rn_2/n_1$ (n_2/n_1 is the ratio of refractive indices of the particle and

the host medium), and I_0^{coh} is the scatter-free on-axis intensity when the phase mask is

removed, r is the distance from the optical axis in the transverse far field plane, and z is

the far field distance from the aperture to the object plane – here the output face of the

cell.

6.3 The On-Axis measurement

To demonstrate the coherence filtering ability of a vortex phase mask, a HeNe

laser beam ($\lambda = 632.8\ nm$) was passed through a scattering cell containing an aqueous

suspension of $2R = 2.25\mu m$ diameter polystyrene spheres ($n_2 = 1.59$, $n_1 = 1.33$, $w_s = 1.34$

μm). The concentration of spheres, ρ, was varied from 0 to 2.3 x 10^8 spheres/ml in the

$L = 10\ mm$ long cell. A 10 nm laser filter was placed at the output of the laser to reject

broadband radiation from the plasma tube. A $2w = 25\ \mu m$ diameter aperture was placed

near the input face of the cell, thereby achieving a value of $a_1 = 0.04$. (Note: a larger

aperture produces a smaller fraction of scattered light, whereas a smaller aperture results

in a weaker signal.) The output plane of the scattering cell was imaged without

magnification with a 50 mm focal length, f/2 lens, onto a Pictor Model 416XT 16 bit

digital camera having 9 μm × 9 μm pixels. To take advantage of the full dynamic range

of the camera, time exposures varied from $T_{exp}=30\ s$ for strong scattering to $1\ s$ for weak

scattering. To achieve a large diffracted vortex core in the detection plane, the vortex

phase mask was placed near the imaging lens.

Samples of the recorded images are shown in Fig. 3. Note that dark frame images

have been subtracted to increase the accuracy of our data. The "scatter-free" case, $\rho=0$,

in Fig. 6.3(a) shows a vortex core at the origin (even though $|m|(\lambda_0\ /\ \lambda)$ is greater than

unity), as well as radial diffraction lines caused by the discrete phase steps on the mask.

We confirmed the vortex nulling effect predicted in Chapter 4 by determining the ratio of

power in the core to that of the total beam: $\left(\delta P\ /\ P_{total}\right)_{exp} = 10^{-5}$ whereas

$\left(\delta P\ /\ P_{total}\right)_{theory} = 3\times10^{-6}$. In the strong scattering case, $\rho = 2.3\ \text{x}\ 10^8\ cm^{-3}$, diffuse light

fills the image in Fig. 6.3(b). Line plots superimposed on the images depict the intensity

distributions through the vortex and across the beam. We note that speckle from coherent

scattering is not seen owing to long integration times and an average speckle area about

the size of a pixel.

To quantify the amount of light scattered into the vortex core we determined the

average number of counts per pixel per second, κ , within a 3×3 array of pixels centered

on the vortex at r=0. A mean value was obtained by averaging over 3 repeated

measurements at a given concentration:

$$\overline{\kappa}_\rho = T_{exp}^{-1} \sum_{i,j,k=1}^{3}(1/27)n_k(x_i,y_j) \tag{6.4}$$

where n_k is number of photons counted at the pixel labeled by *(i,j)*. For comparison we

also measured the average counts per pixel per second, $\overline{\text{K}}_\rho$, over a large area of the beam.

The ratio $\overline{\kappa}_\rho / \overline{K}_{\rho=0}$, which may be compared with Eq. (6.3), is shown in Fig. 6.4 as a

function of the normalized particle concentration ρ/ρ_0, where $\rho_0 = 2.5 \times 10^7 cm^{-3}$. As

expected from Eq. (6.3), the relative intensity of the core initially increases as ρ/ρ_0

increases, and then decreases as scattering attenuates the transmitted light. The solid line

in Fig. 6.4 represents the calculated values of Eq. (6.3). The coefficient C_0 is assigned

the measured value $\overline{\kappa}_{\rho=0} / \overline{K}_{\rho=0} = 0.033$. The scattered light is expected to be incoherent,

and thus we set $C_{j>0} = 1$. The summation in Eq. (6.3) may be terminated at $j=3$ since the

model is valid for only a few scattering events. Thus, using no adjustable parameters, we

find good agreement between our data and the predicted values in Eq. (6.3).

6.4 The Cross Sectional Measurement of the Scattering Amplitude

As mentioned previously, the OVCF technique may also be generalized to the

measurement of the cross sectional profile of the scattering amplitude. If we translating

the vortex core the intensity measured inside the core will correspond to the angle the

core is centered on. By rastering the phase mask as depicted in Fig. 6.5, the entire

forward-scattering amplitude may be measured. In order to demonstrate this, an

experiment was performed with the experimental setup shown in Fig. 6.2. In this case,

the density of scatterers was fixed at a value of $4.6\rho/\rho_0$. The beam had a width,

$w=1.9$mm in the mask plane and the vortex phase mask was translated horizontally across

the beam in 76.2μm increments. An image was captured by the camera at every

increment and the average number of counts per pixel per second, $\bar{\kappa}$, within a 3×3 array

of pixels centered on the vortex at r=0 was calculated using Eq. (6.4). The ratio $\bar{\kappa}/\bar{\kappa}_0$,

where $\bar{\kappa}_0$ is the scattering intensity at θ=0, is plotted as a function of θ in Fig. 6.6. The

scattering angle θ is normalized to the angular beam size in the mask plane, θ_0=21mrad.

As expected the peak scattering intensity occurs at $\theta \approx 0$.

6.5 Conclusions

In conclusion we have used an optical vortex phase mask to null unscattered

coherent light and measure incoherent scattered light along the optical axis. The

concentration dependent scattering intensity agreed with a theoretical model for multiple

scattering. This novel technique may be generalized to measure the scattering spectrum

by translating the phase mask across the scattered beam. Our measurements confirm that

an optical vortex may be used as a window to measure a weak optical signal in the

presence of an intense superimposed coherent beam of light.
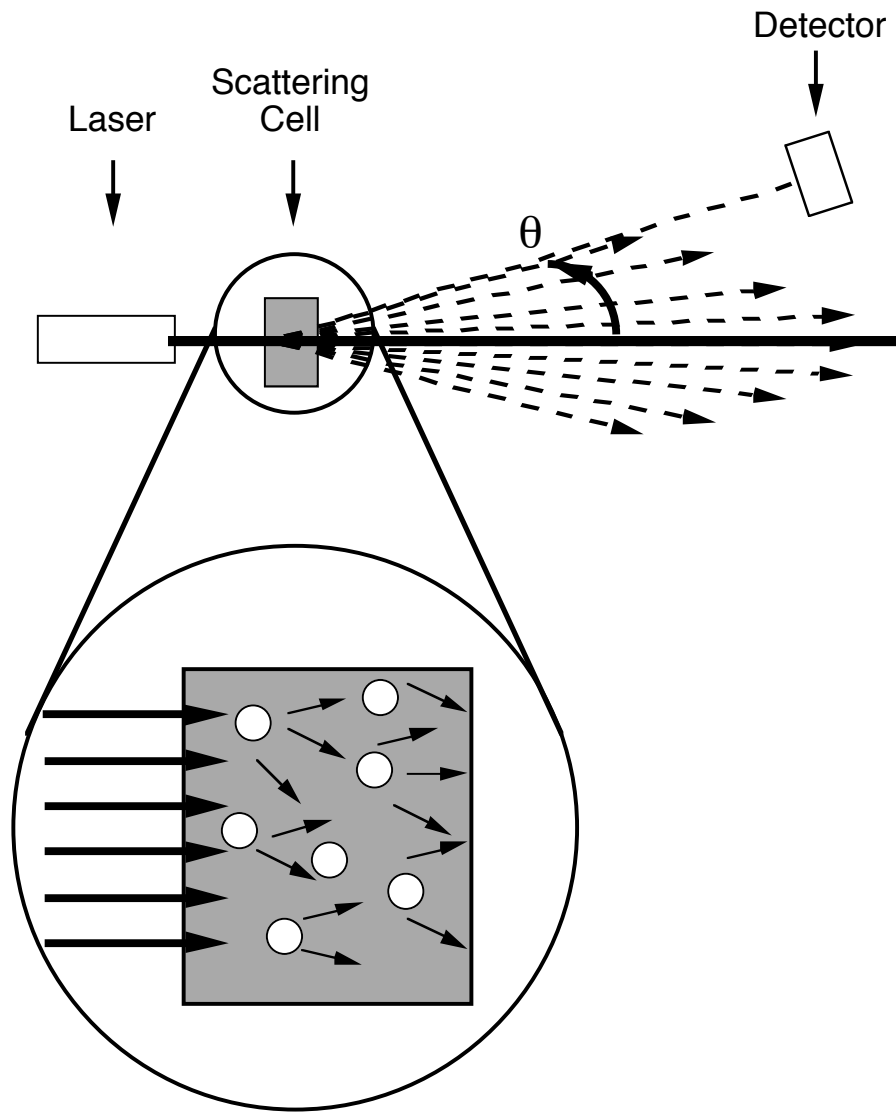
FIG. 6.1   A schematic depiction of an optical scattering experiment. When the laser

beam is transmitted through a scattering cell, particles in the scattering medium scatter

the light multiple times. A detector may be used to measure the intensity of the scattered

light as a function of the angle at which it is scattered.   Although light scatters in all

directions it scatters preferentially in the forward direction, $\theta \approx 0$ along the optical axis.
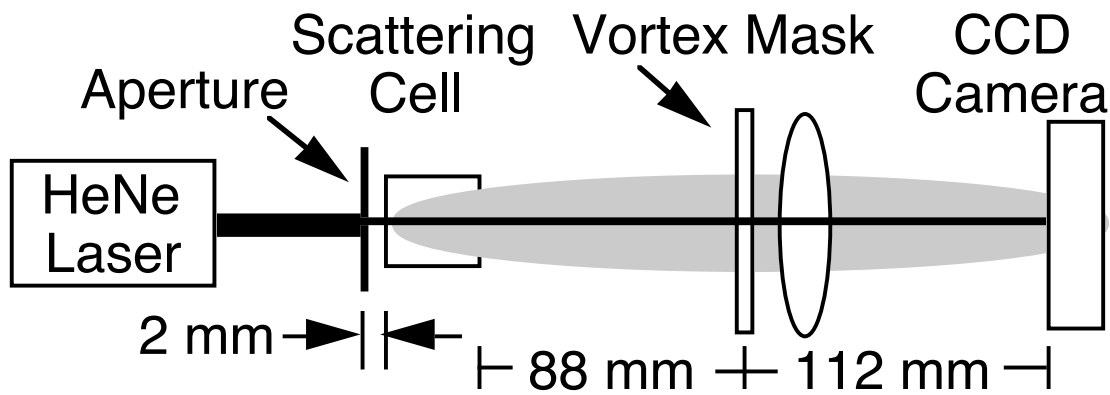
FIG. 6.2   Schematic diagram of the experiment showing light from a laser beam

passing through an 25 µm diameter aperture, a 10 mm long scattering cell, a vortex phase

mask, and an imaging lens arranged for unity magnification onto a low noise digital

astronomy camera.
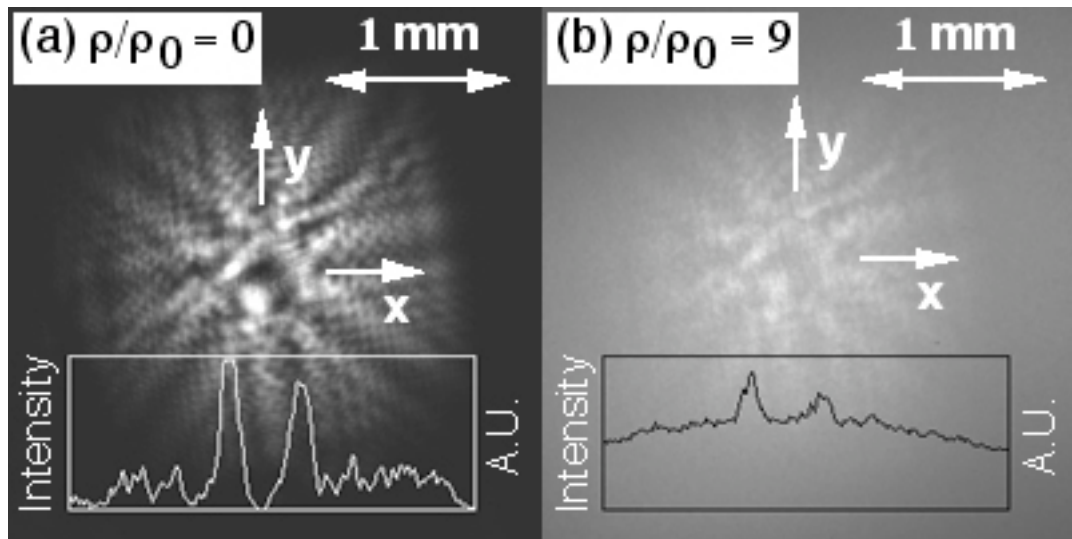
FIG. 6.3   Recorded intensity distributions for (a) zero scattering and (b) high scattering. Superimposed line plots show intensity profiles, I(x,y=0), through the vortex cores. The intensity nearly vanishes in (a), but is nonzero due to zero-angle scattering in (b).
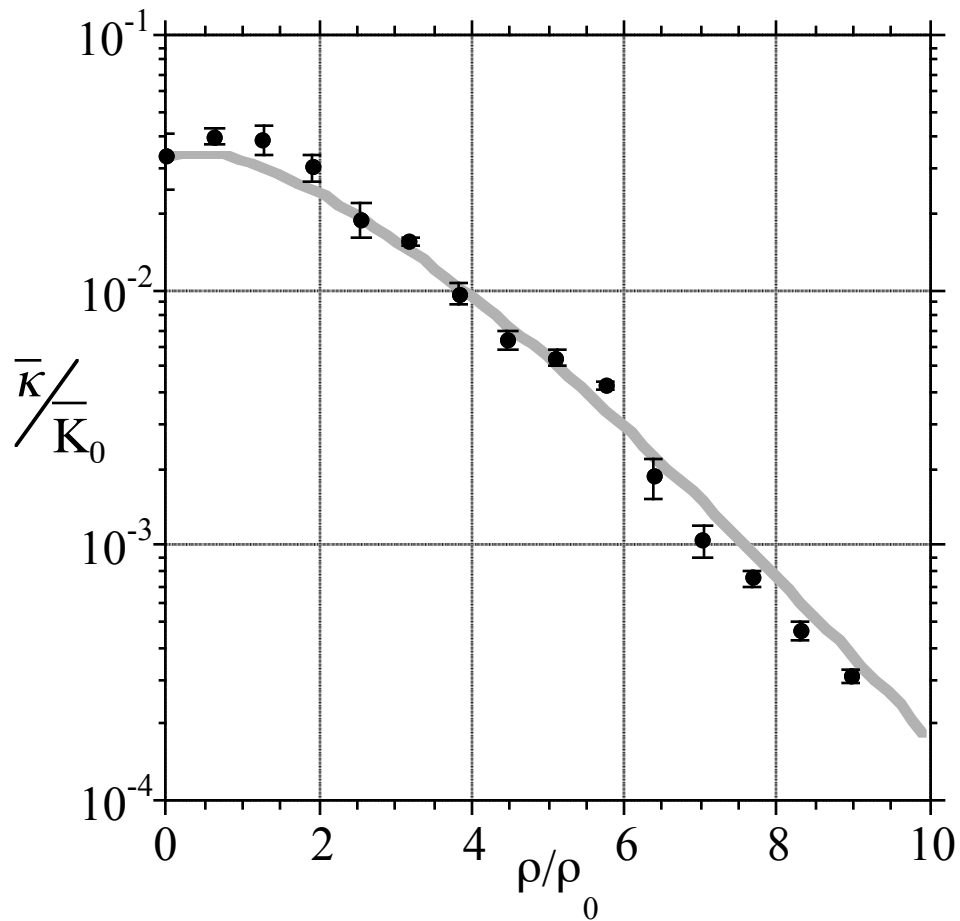
FIG. 6.4   Zero-angle scattered light as a function of scattering concentration where

ρ_0 = 2.5x10^{7}cm^{-3}, $\overline{\kappa}$ is proportional to the average intensity over a small region of the

vortex core, and $\overline{K}_0$ is proportional to the average intensity across a large area of the

beam at $\rho=0$. The experimental data (circles) agrees well with a multiple scattering

theoretical model (line).
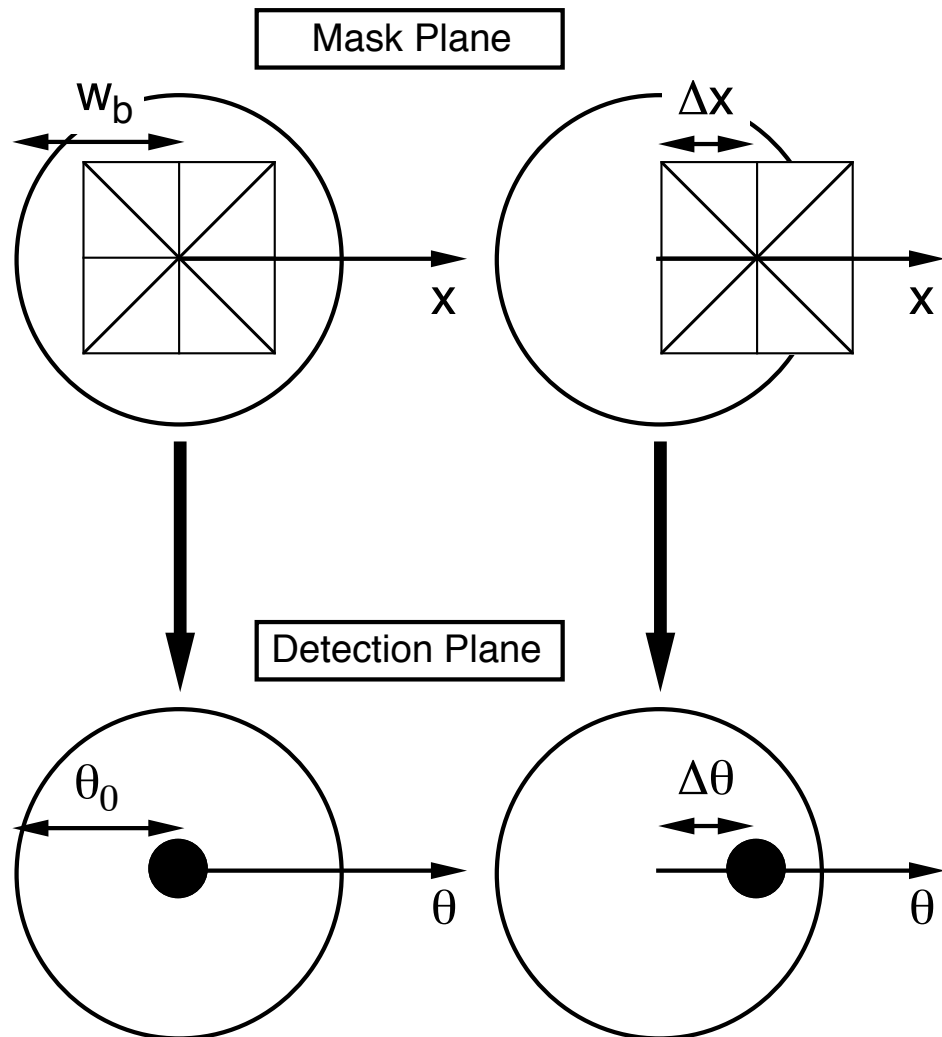
FIG. 6.5   Schematic diagram of the measurement of the angular spectrum with an OVCF. A vortex DOE is translated in the x-direction by an amount Δx and the vortex core in the detection plane is translated by an amount $\Delta\theta$. By measuring the core intensity the angular spectrum may be measured.
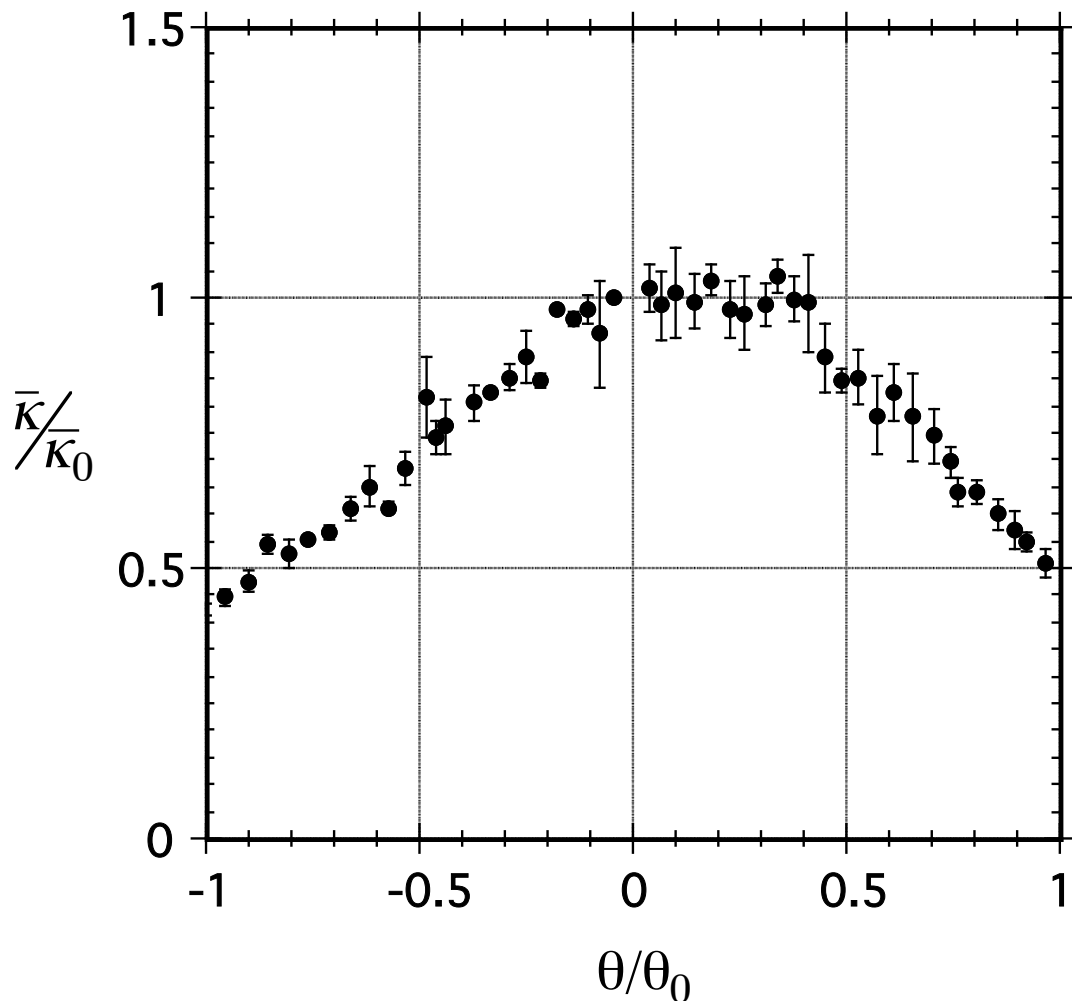
FIG. 6.6   The angular scattering spectrum. Light from a HENE laser with a

wavelength of 633 nm was scattered by a solution of 2.25μm polystyrene spheres in

water with a concentration of 1.15×10^8 spheres/ml. As expected the light is scattered

preferentially in the forward direction and has an approximately Gaussian profile for

small angles.

7. Application 2: The Enhanced Discrimination of Binary Sources

7.1 Introduction

It has been an ongoing struggle in the field of optics to push back the limits of resolution. Two point sources are considered resolvable if a distinct light distribution can be detected for each source [119]. The limits of resolution affect a wide range of fields including microscopy [158], astronomy [159], remote sensing [160], and pattern recognition [161]. For many situations, it is not always necessary to measure the intensity distribution of each source but is often enough just to distinguish between them. A weaker nearly collinear signal may be lost in the intense glare of a brighter nearby source. In this case, it may be only necessary to attenuate the brighter source so the weaker signal may be detected. There have been many novel techniques implemented recently to achieve this goal [148, 160]. This chapter will present a new technique allowing one to differentiate the light from two nearby sources by the use of an optical vortex diffractive mask.

7.2 Vortex formation in the focal region

When a lens of diameter, D, and focal length, f, is illuminated by a single point source located a distance $z_s \gg f$ from the lens, a single spot will form in the focal plane.

Because the aperture of the lens diffracts the light from the source, the focal spot is not a point but rather has an Airy disk amplitude profile given by [ref],

$$A(r,\theta) = E_0 \frac{J_1\big(2.44(\theta/\theta_d)\big)}{2.44(\theta/\theta_d)} \tag{2}$$

where E_0 is the characteristic amplitude, $\theta_d = 1.22\lambda/D$, $\theta = r/f$, and r is the radial coordinate in the focal plane. Now let us examine how the amplitude profile in the focal plane of the lens is affected if an ideal m=1 vortex mask is placed at the entrance pupil of the lens as depicted in Fig. 7.1. If the vortex mask is centered on the z-axis (θ=0), the amplitude profile of the vortex beam in the focal plane may be described by [13]:

$$A(\theta') = E_0\big[\theta_d/\theta'\big]\big[J_1(\theta'/\theta_d)H_0(\theta'/\theta_d) - J_0(\theta'/\theta_d)H_1(\theta'/\theta_d)\big] \tag{3}$$

where $\theta' = 3.83\theta$, and J_n and H_n are the Bessel and Struve functions of order n, respectively. The vortex intensity profile, $I_{m=1}(\theta) = |A(\theta)|^2$, shown in Fig. 7.2 (solid curve), exhibits a minimum value at θ=0 and a peak value at $\theta_v = 0.64\theta_d$. For comparison, the intensity profile of an Airy disk, $I_{m=0}(\theta)$, is also shown in Fig. 7.2 (dashed curve). It resembles a bulls-eye pattern, with a peak value at θ=0 surrounded by concentric dark rings, the first of which occurs at $\theta=\theta_d$.

7.3 Resolution Enhancement by an Optical Vortex

Let us now consider how the amplitude profile in the focal plane of the lens will change if a second point source (labeled Source 2 in Fig. 7.1) is also present. Consider the experiment depicted in Fig. 7.1, where light from two nearly collinear sources,

subtending an angle, $\alpha \ll 1$, is transmitted through a vortex phase mask placed next to a lens of focal length f, and diameter D. If we assume the two sources are mutually incoherent (i.e. they radiate independently), the intensity in the focal plane of the lens is the sum of the intensities of each source. Since the two sources subtend an angle, α, the focal spots of each source described by Eq. (2) will have an angular separation, α.

The Rayleigh criterion states that the images of two point sources are resolved when the intensity maximum of one source overlaps the first intensity minimum of the second source. For an Airy disk profile (m=0), this occurs when the two focused beams are separated by an angle $\alpha = \theta_d$ as seen in Fig. 7.3(a). However, when an m=1 vortex phase mask is placed in front of the lens (as depicted in Fig. 7.1), the Rayleigh criterion is satisfied when the intensity maximum of one source overlaps with the vortex core of the second source. By measuring the distance between the first intensity maximum and minimum of Eq. (2), one may show that this occurs when the two sources are separated by an angle $\alpha = \theta_v = 0.64\theta_d$ as seen in Fig. 7.3(b). Therefore the two point sources are resolvable at smaller separation angles when a vortex phase mask is present, than they were without the mask present. The ratio, θ_d/θ_v, may be used as a measure of the enhancement in resolution gained by the use of a vortex phase mask. In the focus of the lens depicted in Fig. 7.1, a theoretical value of, $\theta_d/\theta_v = 1.56$, may be calculated.

7.4 Experimental Results

To verify these results, an experiment was performed as depicted in Fig 7.1. Spatially incoherent light from a halogen bulb with a mean wavelength, $\bar{\lambda}$=700nm, was coupled into two optical fibers of diameter, $2r_s$=110μm. To insure the two fibers emitted mutually incoherent light, the two fibers differed in length by an amount Δl=1m, which was much greater than the longitudinal coherence length [ref], $l_c = \bar{\lambda}^2/\Delta\lambda \approx 2.5$μm. The total power emitted by the first fiber (labeled Source 1 in Fig. 1) was 0.163±0.005μW and the total power emitted by the second fiber (labeled Source 2 in Fig. 7.1) was 0.125±0.005μW. A lens of focal length, f=150mm, was placed a distance z_s=1.45m from the output of the two fibers, forming two focused spots in the back focal plane of the lens. A vortex phase mask was placed at the entrance pupil of the lens inducing an m=1 vortex into the intensity profiles of each source. Since each source was an incoherent extended source rather than an ideal point source the light at the entrance pupil of the lens was not perfectly spatially coherent. A useful measure of spatial coherence is the coherence area, which is the area over which points in a beam of light are correlated. According to the Van Cittert-Zernike theorem, the coherence area of a beam of light increases upon propagation from a source. The coherence area at a distance z_s from an extended spatially incoherent source is given by [149],

$$A_C = \pi\left(0.61\bar{\lambda}z_s/2r_s\right)^2 \tag{3}$$

The ratio of the coherence area (A_C) to the area of the entrance pupil of the lens (A_T) gives a qualitative scale of the spatial coherence in the pupil plane. The ratio, A_C/A_T, varies from 0 (incoherent) to 1 (coherent). At the input pupil of the lens the coherence area of each source was calculated to be A_C=99.5mm². To make the two beams spatially coherent

($A_C/A_T \geq 1$), an aperture (labeled **ap** in Fig. 7.1) of radial size r_{ap}=1mm was placed 50mm

after the lens. Thereby making the effective diameter of the lens, D= 3mm, and the

effective area of the entrance pupil of the lens, A_T= 7.1mm^2. This also decreased the

resolvability of each source by increasing the radial size of each focal spot to θ_d =

717±4μrad (measured without the phase mask in place). The intensity in the back focal

plane was measured with a Meade Pictor 416XT CCD camera, which produced 16-bit

images with an area of 768 X 512 pixels. The CCD chip had dimensions of 6.90mm X

4.60mm, with an effective area of 81μm^2 per pixel. Because of the weak intensity of the

detected signals, an exposure time of 16s was used and dark frame images (made by

blocking both light sources) were subtracted from each image to remove stray light.

   The center of the vortex core in Source 1 was designated as θ=0, and was located

by imaging Source 1 with Source 2 blocked. Source 1 was held firmly in place and

Source 2 was attached to a translation stage. The separation between the two sources was

varied from Δd_{min}=278μm to Δd_{max} = 1269μm, in increments of Δd= 25±6μm. Images of

the combined beams were recorded for each Δd. Images in the back focal plane of the

lens are shown in Fig. 7.4 for various values of α=Δd/z_s. When α = 192±4μrad

($\Delta d=\Delta d_{min}$=278±6μm), the vortex core in the combined beam appears to be a single

circularly symmetric dark spot located at θ=0 (shown in Fig. 7.4(a)). However as α is

increased, the vortex core appears more elliptical and the intensity at θ=0 increases until

reaching a maximum when α=472±4μrad (Δd=684±6μm) (shown in Fig. 7.4(b)). As α is

further increased, the intensity at θ=0 decreases eventually falling to a minimum recorded

value when α=875±4μrad ($\Delta d=\Delta d_{max}$=1269±6μm) (shown in Fig. 7.4(d)). Also, when

α=717±4μrad (Δd= 1040±6μm), the two sources are just resolvable when the in the

absence of the vortex phase mask (shown in Fig. 7.4(c)).

To quantify the signal measured from Source 2, the number of counts per sec, κ_0,

(which is proportional to power) was measured over an 81 μm^2 aperture at θ=0. The

mean value of κ_0 was determined by averaging over three repeated measurements. For

comparison we also measured the average number of counts per second, $\overline{K}$, over a large

area of the beam (A_{beam}=1.59x10^{5}μm^2). The ratio $\overline{\kappa}_0/\overline{K}$ is plotted in Fig. 7.5 (data points)

as a function of α/θ_d. The error bars in Fig. 7.5 represent the standard deviation in the

measured values of $\overline{\kappa}_0/\overline{K}$. As α increases the ratio $\overline{\kappa}_0/\overline{K}$ traced out the profile of the

vortex embedded in Source 2. When α=192±4μrad (Δd=Δd$_{min}$=278±6μm), the ratio,

$\overline{\kappa}_0/\overline{K}$=6.5x10^{-4}±1.7x10^{-4}. As α was increased the ratio increased to a maximum value of

$\overline{\kappa}_0/\overline{K}$= 1.23x10^{-3}±0.3x10^{-4} when α=θ_v=472±4μrad (Δd=684±6μm). When α was further

increased, the value of $\overline{\kappa}_0/\overline{K}$ further decreased. Falling to a value of

$\overline{\kappa}_0/\overline{K}$=7.0x10^{-4}±1.3x10^{-4} when α=θ_d=717±4μrad (Δd= 104±6μm) and a value of

$\overline{\kappa}_0/\overline{K}$=3.2x10^{-4}±0.8x10^{-4} when α=875±4μrad (Δd=Δd$_{max}$=1269±6μm). Interestingly the

error associated with the measured value of $\overline{\kappa}_0/\overline{K}$ was smallest in value when α=θ_v.

This occurs because the intensity profile of Source 2 has the smallest rate of change at

this point. This may be useful in detecting the angle at which the maximum signal occurs

when the system has a low signal to noise. To quantify the enhancement in resolution,

we calculated the ratio θ_d/θ_v which had a value of 1.52±0.2. This compared well with the

analytic result of 1.56 stated previously.

To better compare theory with experiment a numerical simulation was performed. In the simulation we assumed that light from two point sources form planar beams at the input plane of an ideal m=1 vortex mask placed at the entrance pupil of a lens. Each of the two focused spots produced by the lens may be calculated numerically by,

$$E_f(k_x, k_y) \propto FT[E(x,y)P(x,y)] \tag{4}$$

where *FT[]* denotes a Fourier transform, *E(x,y)* is the field at the entrance pupil of the lens, and P(x,y)=1 within the lens aperture and P(x,y)=0 outside the lens aperture. One focused spot was centered on the origin at $k_x = k_y = 0$ ($\theta = 0$) while the second focal spot was translated in the x-direction. As the second focal spot was translated, the calculated number of counts per second was measured over an aperture centered at $\theta = 0$ with an area that was 1.6×10^{-3} times the total area of the beam. To more accurately model the experiment the total power of the translated source was normalized to be 0.75 times the total power of the source centered at the origin. As shown by the solid line in Fig. 7.5, the numerically calculated number of counts also traced out the profile of the translated source with a peak number of counts per sec of $\overline{\kappa}_0 / \overline{K} = 1.18 \times 10^{-3}$ when the two sources have an angular separation of $\theta_v = 0.61\theta_d$, which differed slightly from the experimental value of $\theta_v = (0.66 \pm 0.01)\theta_d$. The small difference in the shape of the two curves may be attributed to a small misalignment of the two sources in the experiment, where the two sources were not perfectly aligned with the origin in the y-direction. The numerically computed ratio θ_d / θ_v, used as a measure of resolution enhancement, had a value of 1.64 compared to the experimental value of 1.52 ± 0.2 and an analytic value of 1.56. The small difference in θ_d / θ_v may be attributed to the slightly different vortex profiles calculated

numerically as compared to the profile calculated analytically. For comparison the case

of two Airy disks with no vortex present (m=0) is also shown (dashed line in Fig. 7.5).

The value of $\overline{\kappa}_0/\overline{K}$ measured at the first zero of the Airy disk formed by Source 1 traces

out the profile of the Airy disk profile formed by Source 2. However for the Airy disk

case (m=0) the maximum signal occurs when the two sources are separated by θ_d instead

of $0.64\theta_d$, as is the case for two vortex beams (m=1).

7.5 Conclusions

In conclusion, we have used an optical vortex diffractive mask to increase the

contrast between two sources, which allowed the two sources to be distinguished below

the Rayleigh criterion. In our experiments, when a diffractive phase mask was placed in

front of an imaging lens, the resolving power of the system was enhanced by a factor of

1.52 ± 0.2 when compared to the same system without a vortex phase mask present. This

value was in qualitative agreement with the theoretical predicted value of 1.56. We

believe this technique may find uses in the field of astronomy. Where it may enhance the

resolution between binary stars, or aid in the detection of extra-solar planets.
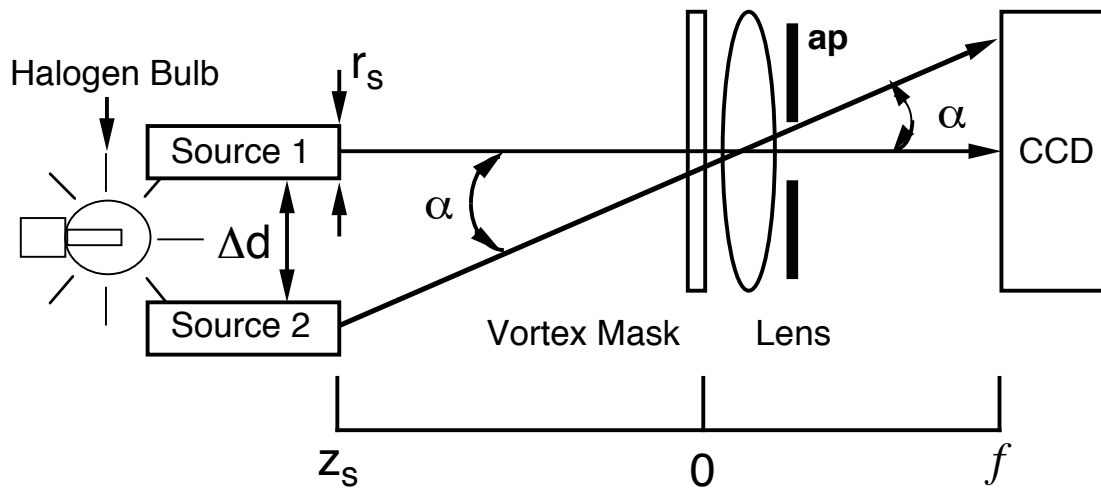
FIG. 7.1   Narrowband light ($\Delta\lambda$=50nm) from a halogen bulb was coupled into the

end of two fiber optic cables of diameter, d_s=105 μm, separated by a distance Δd. A

vortex phase mask was placed a distance z_s=1.45m away from the two sources so that the

two sources subtended an angle α with respect to the mask. A lens of focal length

f=150mm focused the light onto a CCD camera placed in the back focal plane. An

aperture (ap) was placed 5mm behind the lens to increase the radial spot sizes of each

source, thus making the two sources unresolvable in the focal plane.
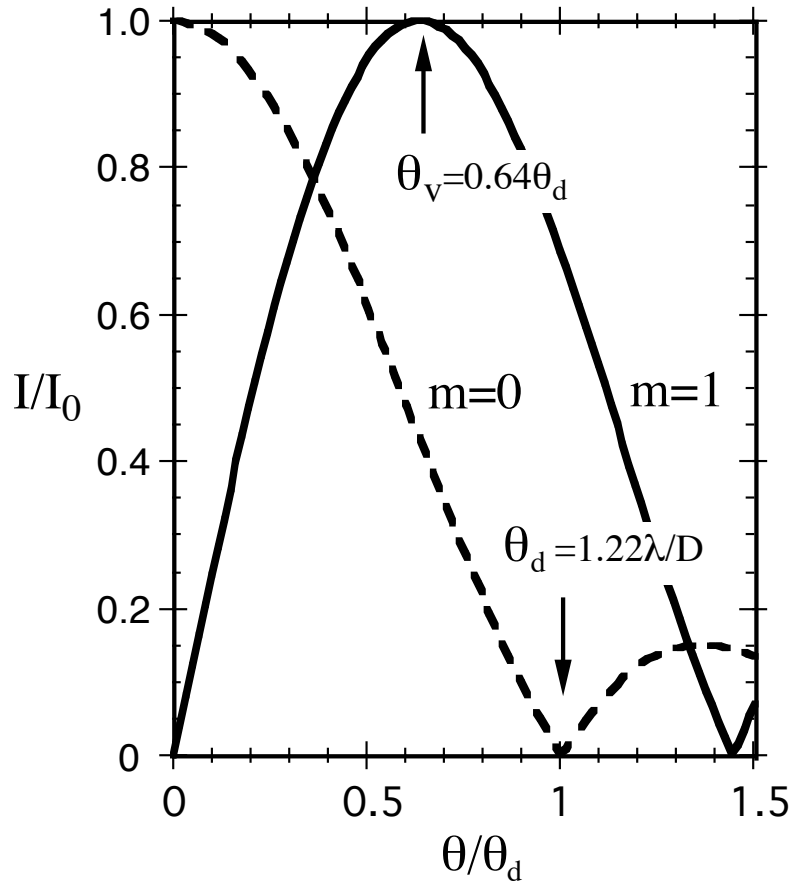
FIG. 7.2   Angular line plots of the intensities, $I_V(\theta)$ (solid line) and $I_A(\theta)$ (dashed

line) in the focal plane. The angle θ is normalized by $\theta_0 = 2/kD$, where k is the wave

number of the focused light. The intensities are normalized to I_0, the maximum beam

intensities for each beam. The vortex profile has a peak at $\theta_V = 2.45\theta_0$, and the Airy disk

profile has a minimum value at the position $\theta_d = 3.83\theta_0$.
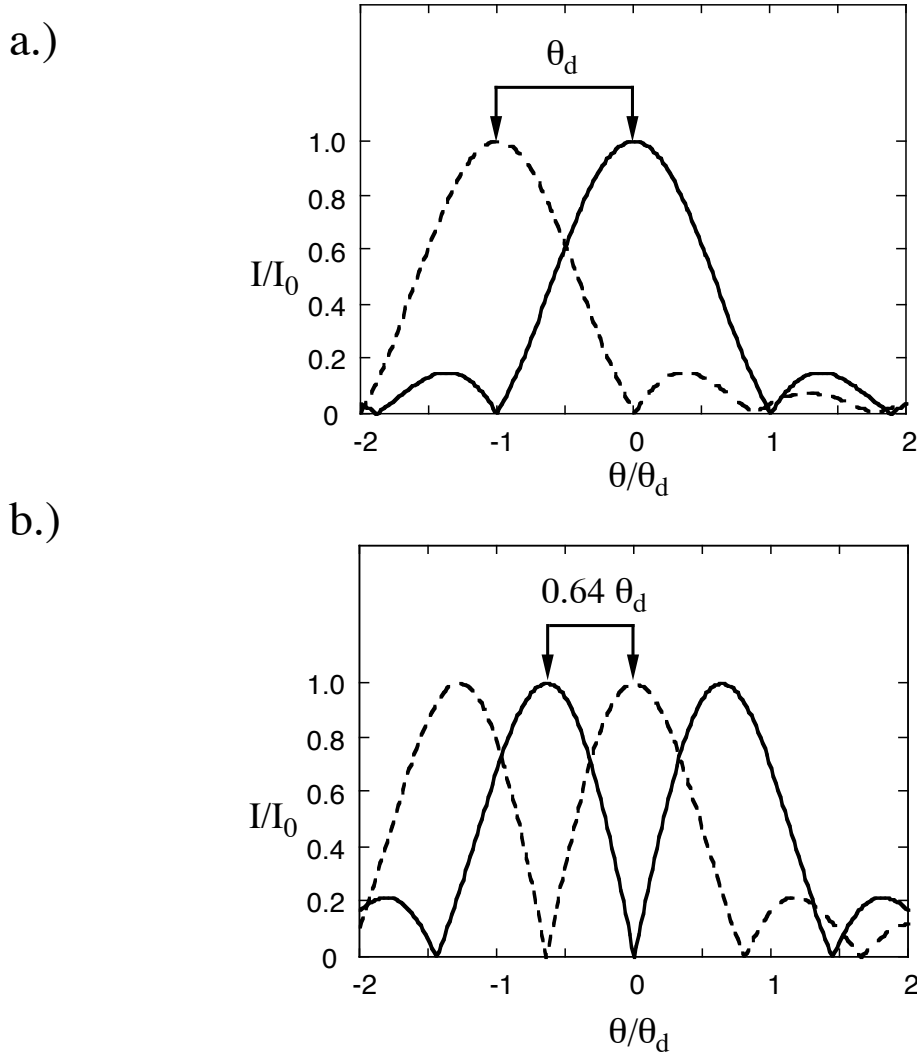
FIG. 7.3   Angular line plots in the back focal plane of a lens of focal length f and diameter D when two sources are present. The intensity is normalized to I_0 the maximum intensity of each beam, θ is the angle coordinate in the focal plane and is normalized by $\theta_d = 1.22\lambda/D$. a.) When the two sources have an Airy disk distribution, the two sources are resolvable when separated by the angle θ_d. b.) When the two sources have a vortex distribution, the two sources are resolvable when separated by 0.64 θ_d.
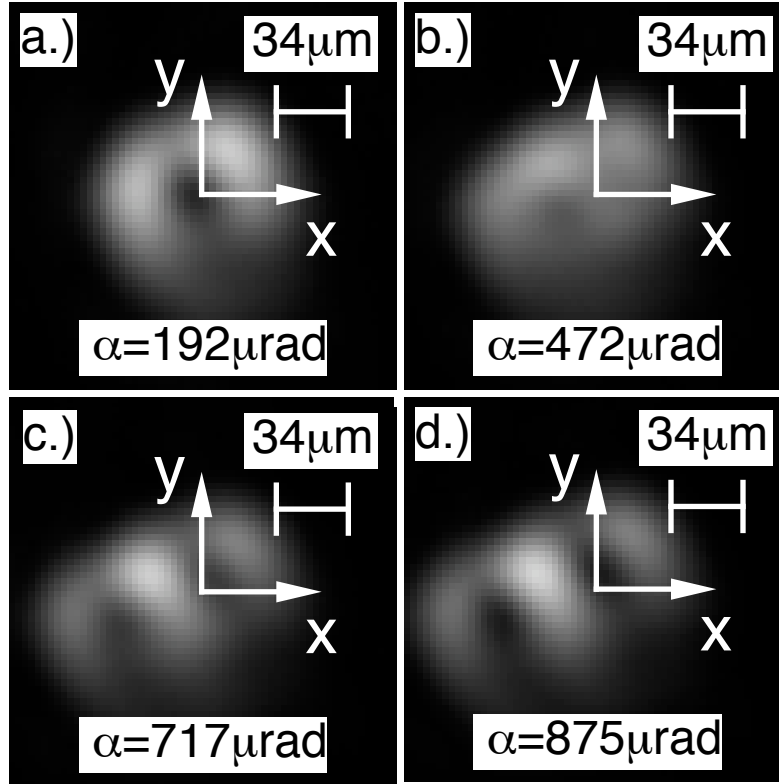
FIG. 7.4   Recorded intensity distributions for an angular separation between the two

sources of a.) α=192µrad, b.) α=472µrad, c.) α=717µrad, and d.) α=875µrad. Initially,

the vortex cores of each source overlap as depicted in frame (a). As α is increased the

intensity at θ=0 (x=y=0) increases until reaching a maximum value, depicted in frame

(b). As α is further increased, the intensity at θ=0 decreases. Frame (c) depicts the case

when the two sources are separated by θ_d and are just resolvable without the vortex mask

in place. Frame (d) shows the case when the two sources are separated by the maximum

angular separation.
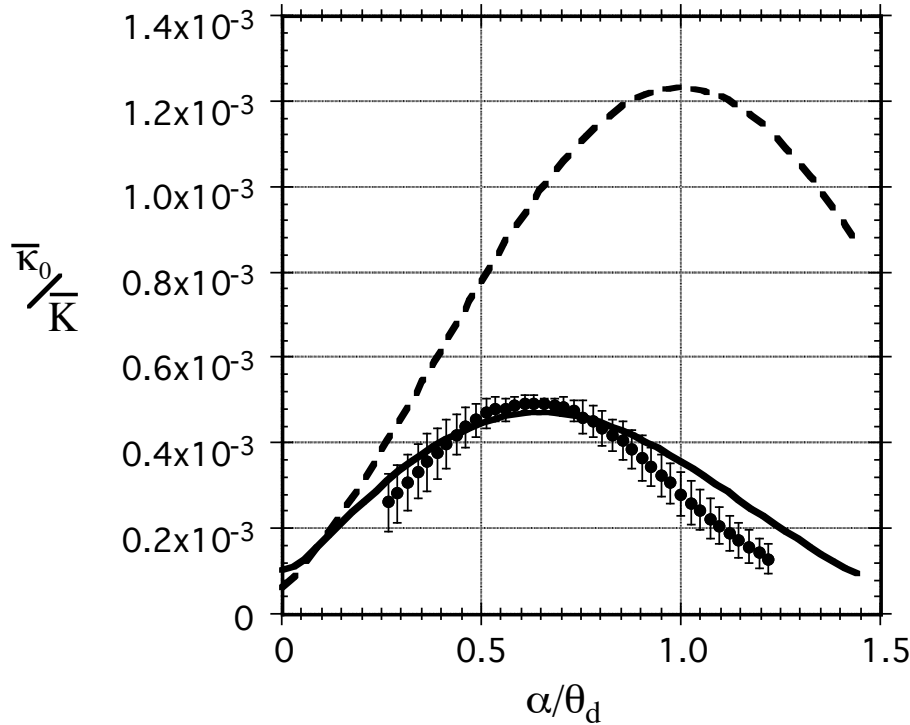
FIG. 7.5   A plot of the ratio, $\overline{\kappa}_0/\overline{K}$, of the average number of counts/sec measured at

$\theta = 0$ as a function of α, the angular separation of the two sources when an m=1 vortex

DOE is placed in front of the imaging lens. The value of $\overline{\kappa}_0$ was measured over an

$81\mu m^2$ aperture and the value of $\overline{K}$ was measured over a $1.59 \times 10^5 \mu m^2$ aperture. The

experimental plot is shown as data points with error bars and exhibits a peak value of

$\overline{\kappa}_0/\overline{K} = 1.23 \times 10^{-3} \pm 0.3 \times 10^{-4}$ at an angular separation of $\theta_v = (0.66 \pm 0.01)\theta_d$. A numerical

simulation (solid line) shows good agreement between theory and experiment. The same

model was used to show the m=0 case (dashed line).

Appendix A. Coherence Theory

Spatial coherence refers to how well correlated two points along a wavefront are in time. A measure of the spatial coherence of a single beam of light may be found by calculating the mutual coherence function (MCF) [149] of the electric field for points in the transverse plane, $\vec{r}_1$ and $\vec{r}_2$ (see Fig. A.1),

$$\Gamma(\vec{r}_1, \vec{r}_2, \tau) = \left\langle E(\vec{r}_1, t + \tau) E^*(\vec{r}_2, t) \right\rangle \tag{A.1}$$

where $<>$ denotes a time average and τ is the time delay between points and , $\vec{r}_1$ and $\vec{r}_2$. If we assume that the light is statistically stationary then the time average may be replaced by an ensemble average when convenient. Also, it is often more convenient to deal with the temporal Fourier transform of the MCF known as the Mutual spectral density function (MSDF), although we will opt to use the MCF whenever possible.

The utility of the MCF in coherence theory is best demonstrated by the Young's two-slit experiment depicted in Fig. A.2. Light from a source, S, is allowed to propagate a distance l_1 to a pinhole plane containing two pinholes, P_1 and P_2 separated by a distance d. The light is allowed to pass through the pinholes and propagate a distance l_2 to an observation plane. The field at a point Q in the observation plane may be described as a superposition of the fields emitted from each pinhole,

$$E(Q,t) = K(Q,P_1)E(P_1, t - {}^{\rho_1}\!/_c) + K(Q,P_2)E(P_2, t - {}^{\rho_2}\!/_c) \tag{A.2}$$

where $K(Q,P_i)$ represents the transfer function for the light emitted from the ith pinhole to the point Q in the observation plane. The optical intensity at point Q in the observation plane is then given by,

$$(A.3)$$

$$I(Q) = |K(Q,P_1)|^2 \left\langle E(P_1,t - \rho_1/c)E^*(P_1,t - \rho_1/c) \right\rangle$$

$$+ |K(Q,P_2)|^2 \left\langle E(P_2,t - \rho_2/c)E^*(P_2,t - \rho_2/c) \right\rangle$$

$$+ K(Q,P_1)K^*(Q,P_2)\left\langle E(P_1,t - \rho_1/c)E^*(P_2,t - \rho_2/c) \right\rangle$$

$$+ K^*(Q,P_1)K(Q,P_2)\left\langle E^*(P_1,t - \rho_1/c)E(P_2,t - \rho_2/c) \right\rangle$$

Using the definition of the time average, the third angular bracket is:

$$\left\langle E(P_1,t - \rho_1/c)E^*(P_2,t - \rho_2/c) \right\rangle = \lim_{T \to \infty} \frac{1}{2T} \int_{-T}^{T} E(P_1,t - \rho_1/c)E^*(P_2,t - \rho_2/c)dt \quad (A.4)$$

A change of variables to t´=t-ρ_1/c reveals that the angular bracket only depends on the

time difference between the two pinholes, τ=(ρ_1-ρ_2)/c. The third angular bracket may

now be recognized as $\Gamma(P_1,P_2,\tau)$ and the fourth angular bracket is just the complex

conjugate of the third bracket, $\Gamma^*(P_1, P_2, \tau)$. If we define a normalized function

$$\gamma_{12}(\tau) = \frac{\Gamma(P_1,P_2,\tau)}{\left[\Gamma(P_1,P_1,0)\Gamma(P_2,P_2,0)\right]^{1/2}} \quad (A.5)$$

and write it in the form,

$$\gamma_{12}(\tau) = |\gamma_{12}(\tau)| \exp[i\phi_{12}(\tau)] \quad (A.6)$$

the optical intensity at point Q may be expressed as:

$$I(Q) = I_1(Q) + I_2(Q) + 2[I_1(Q)I_2(Q)]^{1/2} |\gamma_{12}(\tau)| \cos[\phi_{12}(\tau)] \quad (A.7)$$

where $I_1(Q)$ and $I_2(Q)$ are the intensities due to the first and second pinholes respectively.

It is now apparent that $|\gamma_{12}(\tau)|$ is a measure of the visibility of interference fringes and

$\phi_{12}(\tau)$ is a measure of the fringe deformation.

   If the source S, used in Fig. A.2 is a point source, then light emitted from the

source will have traversed a fixed distance R_1 and R_2 in reaching the pinholes P_1 and P_2

respectively. Unless the source position along the x-axis bisects the separation distance

between the two pinholes, $R_1 \neq R_2$, and the phase difference between the light arriving at

pinholes P_1 and P_2 is $\theta_{12}=2\pi|R_1-R_2|/\lambda$. If θ_{12} does not vary in time, $|\gamma_{12}(\tau)|=1$ and

$\phi_{12}(\tau)=\theta_{12}$. In this case we will say the light emitted from pinholes P_1 and P_2 is

completely spatially coherent. Meaning that the fringes produced by Young's experiment

have perfect contrast and extend over the entire plane of observation. In practice such an

ideal situation is impossible but it is a useful limiting case never the less. It is possible to

show [ref] that if $|\gamma_{12}(\tau)|=1$ in a domain D for all τ, then the MCF may be represented in a

factored form given by,

$$\Gamma(P_1,P_2,\tau) = U(P_1)U(P_2)\exp(-i2\pi\nu_0\tau) \tag{A.8}$$

where $U(P_i)$ is a monochromatic field of frequency, $\nu_0 =ck_0/2\pi$ that is a solution to the

Helmholtz equation given by,

$$\left(\nabla^2 + k_0^2\right)U(P_i) = 0 \tag{A.9}$$

Therefore only monochromatic fields are coherent. However, light that is band limited

may be treated as quasi-monochromatic and may be approximated as coherent provided

the bandwidth, $\Delta\nu << \bar{\nu}$, where $\bar{\nu}$ is the mean frequency of the band limited light.

If the source in Fig. A.2 has some extended shape instead of a point source

distribution, then θ_{12} will differ depending on what point on the source contributes light

to the two pinholes and in general $|\gamma_{12}(\tau)| \neq 1$. If we assume the source is composed of N

point sources all radiating as a function of time, then the phase difference between the

two pinholes will also be a function of time, $\theta_{12}(t)$. If each radiator is emitting randomly,

the time average in Eq. (A.1) now gives $|\phi_{12}(\tau)| \approx 0$ and the light emitted by the source may

be considered spatially incoherent. However, as Parrent pointed out in his PhD

dissertation [163], a completely incoherent source cannot radiate. Therefore a completely

incoherent field cannot exist in free space.

We may relax the condition on incoherence by instead assuming the source is

composed of N radiators that are not completely independent of each other. If we assume

the correlation between the radiators is a sharply peaked function that is only dependent

on the distance between the radiators, then the properties of a nearly incoherent field are

produced.

Spatial coherence increases upon propagation [119] from a source. This effect

was first pointed out by Van Cittert and was later generalized by Zernike. According to

the Van Cittert-Zernike Theorem, if we assume an incoherent source as we have

described above, the spatial coherence a distance z from the source is the two-

dimensional Fourier transform of the optical intensity in the source plane:

$$\Gamma(\vec{r}_1,\vec{r}_2,0) = \frac{\exp\left[i\overline{k}(r_1 - r_2)\right]}{\pi z_d^2} \iint_A \Gamma(\vec{s},\vec{s},0)\exp\left(-i2\pi \frac{x_{12}x_s + y_{12}y_s}{\overline{\lambda}z_d}\right) dx_s dy_s \qquad \text{(A.10)}$$

where $\vec{r}_1 = x_1\hat{i} + y_1\hat{j}$ and $\vec{r}_2 = x_2\hat{i} + y_2\hat{j}$ are two points in the propagated beam (see Fig.

A.2), $r_1 = \left(x_1^2 + y_1^2\right)^{1/2}$, $r_2 = \left(x_2^2 + y_2^2\right)^{1/2}$, $x_{12} = (x_1 - x_2)/2$, $y_{12} = (y_1 - y_2)/2$,

$x_s = (x_1 + x_2)/2$, $y_s = (y_1 + y_2)/2$, and $\Gamma(\vec{s},\vec{s},0)$ is the optical intensity in the source

plane. An interesting consequence of this theorem is that the absolute value of the MCF

in the plane $z=z_d$ is only a function of the distance between the two points in the pinhole

plane that are being examined. Thus any partially coherent source may be represented by

a fictitious incoherent source a distance $z=z_d$ in front of the real source. Thus if we know

a priori the MCF for any given plane we can calculate it in another plane by assuming a

fictitious incoherent source. Hopkins used this method extensively to study the influence

of partial coherence on image formation and it bares his name today.

A Carter-Wolf type source is one model source of great utility derived from the

Van Cittert-Zernike theorem. It was first introduced by Schell to model a partially

coherent source but was later examined in more depth and thus popularized by Carter and

Wolf. A Carter-Wolf type source may be described by MSDF that is separable into two

functions:

$$\Gamma(\vec{r}_1, \vec{r}_2, v) = I(x_s, y_s, v) g(x_{12}, y_{12}, v) \tag{A.11}$$

where the function $I(x_s, y_s, v)$ represents the average intensity of the source and

$g(x_{12}, y_{12}, v)$ represents the correlation between two points in the beam (see Fig. A.3).

Since the correlation between the two points only depends on the distance between them,

such a source obeys the Van Cittert-Zernike theorem.

If we choose a sharply peaked function for $g(x_{12}, y_{12}, v)$ that varies rapidly

compared to $I(x_s, y_s, v)$ then the source will be incoherent. However, if we instead

choose a function $g(x_{12}, y_{12}, v)$ that is slowly varying with respect to $I(x_s, y_s, v)$ then the

source will be spatially coherent. A partially coherent source may be modeled by a

Gaussian correlator:

$$g(x_{12}, y_{12}, v) = \exp\left[-\left(x_{12}^2 + y_{12}^2\right)/L_c^2\right] \tag{A.12}$$

where L_c is the characteristic waist size of the Gaussian correlator and is known as the

transverse coherence length. In this case, changing the value of L_c will vary the spatial

coherence of the source. If L_c is made large compared to the source size, then more

points in the source will be strongly correlated and the source may be considered spatially

coherent. However, if L_c is made small compared to the source size only a few points

will be correlated and the source may be considered spatially incoherent. It should be

noted that a Gaussian form for $g(x_{12}, y_{12}, \nu)$ is inaccurate for very small coherence lengths

($L_c << w_0$) since the actual correlation function will be the two dimensional Fourier

transform of the irradiance of the source. Despite this fact, the Gaussian correlator of Eq.

(A.12) provides an excellent approximation for most partially coherent systems of

interest.

One particular property of light that is directly affected by spatial coherence is the

beam spread. The amount a beam will spread under propagation is strongly dependent on

the amount spatial coherence present in the system. The beam spread of a partially

coherent beam may be described by the beam spread equation [149]:

$$ w(z_d) = \left[2\pi w_0^2 \left((z_d^2 / k^2 w_0^2 L_c^2) + 1 \right) \right]^{1/2} \tag{A.13} $$

where $w(z_d)$ is the width of the beam a distance z from a source of width w_0. If $z >> k w_0 L_c$

then Eq. (A.13) reduces to the simple form:

$$ w(z_d) \cong (2\pi)^{1/2} z_d / k L_c \tag{A.14} $$

According to Eqs. (A.13) and (A.14), the larger the value of L_c and hence the more

spatially coherent the light source is, the less the beam will spread as it propagates.
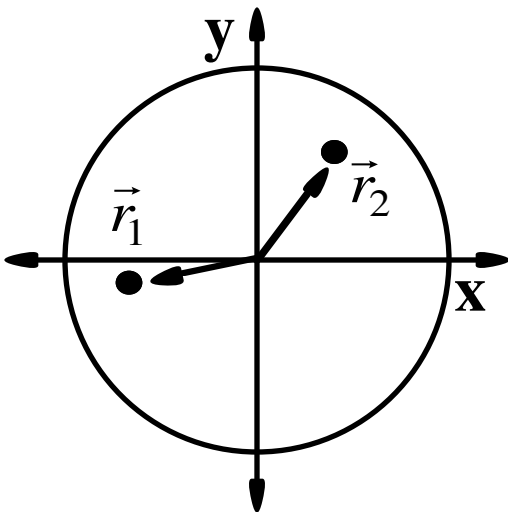
FIG. A.1   Cross-section of a beam of partially coherent light.   The

correlation between points $\vec{r}_1$ and $\vec{r}_2$ is used as a measure of the spatial coherence.

Points $\vec{r}_1$ and $\vec{r}_2$ are allowed to have any value in the (x, y) plane inside the beam

depicted as a circle.
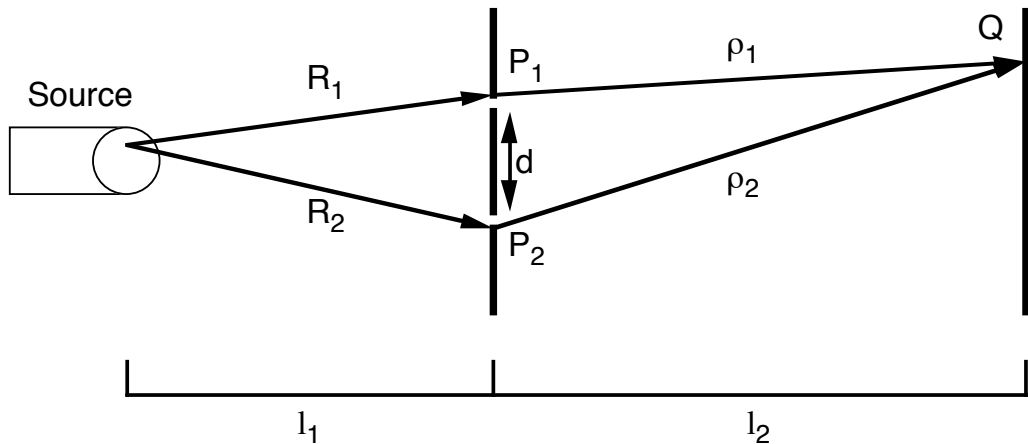
FIG. A.2   A diagram of the Young's two slit experiment. Light from an

extended source is incident on a two pinhole (P1 and P2) separated by a distance

d. The source is a distance l_1 away from the pinholes and follows paths R_1 and R_2

to pinholes P_1 and P_2 respectively. The transmitted light from the two pinholes is

then observed at a point Q in a detection plane a distance l_2 from the pinholes.

The light emitted from pinholes P_1 and P_2 travel paths ρ_1 and ρ_2 to point Q

respectively.
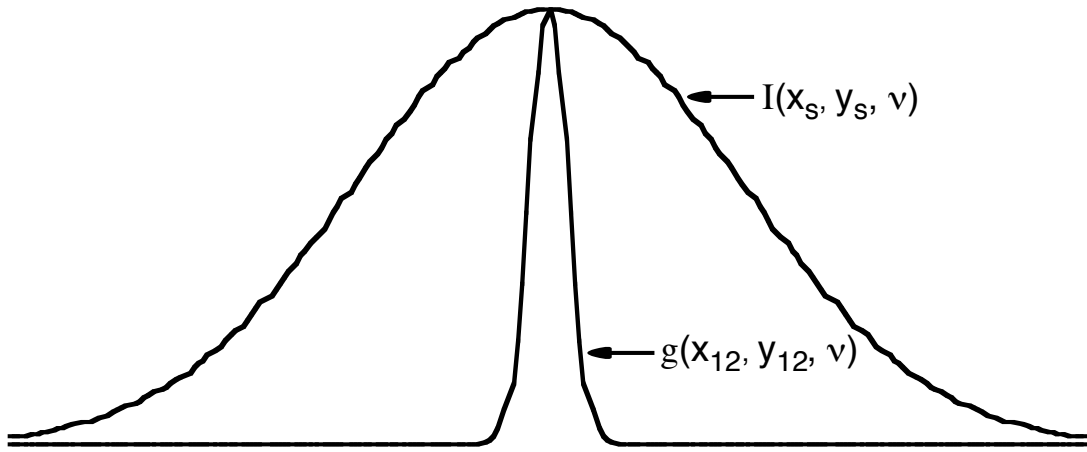
FIG. A.3   Schematic depictions of the functions used in a Carter-Wolf type source.

The function $I(x_s, y_s, \nu)$ is a function of the average variables of the source, (x_s, y_s), and

measures the intensity of the source. The function $g(x_{12}, y_{12}, \nu)$ is a function of the

difference variables of the source (x_{12}, y_{12}) and is a measure of the correlation between

two points in the source. The source may be considered spatially incoherent if

$g(x_{12}, y_{12}, \nu) \gg I(x_s, y_s, \nu)$.

Appendix B. Scattering Theory

When light is incident on a particle with a refractive index that differs from the surrounding medium, the light may scatter off the particle [152]. When light is incident on a turbid medium, light may scatter in all direction but it is most preferentially scattered in the forward direction, along the axis at which it was incident with the turbid medium [154]. When light is scattered multiple times by particles that are larger than the wavelength of the light, the spatial coherence of the light is degraded. Yang et al.[153] have previously discussed the effect multiple scattering has on the spatial coherence of light directed in the forward direction and in this appendix, I will summarize their calculation of the scattering intensity in the forward direction for light that has been scattered j times.

Calculation of the phase function $P_s(\beta,\theta)$

Let us examine a ray of light, which was incident with an impact parameter b on a impenetrable sphere of radius R, and has been scattered at an angle θ from the sphere as depicted in Fig. B.1. Because the sphere is impenetrable, the angle, ϕ, the incident light makes with a normal to the surface is equals the angle the scattered light makes with a normal to the surface. The light is therefore scattered at an angle, $\theta=\pi-2\phi$, with respect to the incident direction. The angular distribution that governs the directional change of light when it's scattered is called the phase function $P_s(\beta, \theta)$, which is a function of the

size parameter $\beta = kR$ and the scattering angle, θ. We may use Mie scattering theory to estimate $P_s(\beta, \theta)$ if we assume the size of the scatterer is large compared to the wavelength of the impinging light. From Mie scattering theory [154]:

$$P(\beta, \theta) = \frac{1}{\sigma_{sca}} \left(\frac{d\sigma}{d\Omega} \right)_{avg} \tag{B.1}$$

where $(d\sigma/d\Omega)_{avg}$ is the differential cross section of the scattering particles averaged over all polarization angles, and σ_{sca} is the scattering cross section. Assuming there is no polarization dependence in the scattering process, the scattering cross section is:

$$\left(\frac{d\sigma}{d\Omega} \right)_{avg} = |f(k,\theta)|^2 \tag{B.2}$$

where $f(k, \theta)$ is the scattering amplitude, which may be given by,

$$f(k,\theta) \cong \frac{iRJ_1(\beta \sin\theta)}{\sin\theta} \tag{B.3}$$

where we have assumed $\beta \gg 1$.

The total scattering cross section is the sum of the scattering and absorption cross sections given by σ_{sca} and σ_{abs} respectively. If we assume total elastic scattering with no absorption then $\sigma_{tot} = \sigma_{sca}$ and using the optical theorem [154]:

$$\sigma_{tot} = \frac{4\pi}{k} \text{Im} \left[f(k,0) \right] \tag{B.4}$$

When $\theta = 0$ in Eq. (B.3) we may calculate f(k, 0) and substitute it into Eq. (B.4) to yield:

$$\sigma_{tot} = 2\pi R^2 \tag{B.5}$$

We may now substitute Eqs. (B.3) and (B.5) into Eq. (B.1) to obtain the phase function:

$$P(\beta, \theta) = \left(\frac{\beta^2}{8\pi} \right) \left(\frac{2J_1(\beta \sin\theta)}{\beta \sin\theta} \right)^2 \tag{B.6}$$

Calculation of the Scattering Intensity

Consider a turbid medium of length L having an optical thickness, $D=\rho/\rho_0$, where

ρ is the density of scatterers in the turbid medium and $\rho_0=(\pi R^2 L)^{-1}$ is the scattering

extinction parameter (see Fig. B.2). By use of a three dimensional model of scattering

the electric field of light that has been scattered j times may be connected to D. The

change in the intensity of light that has traveled through a small slice δD of the scattering

medium as depicted in Fig. B.2 may be given by [153],

$$\delta\left(E_j^{\,2}(D,\vec{\upsilon})\right) = E_{j-1}^2(D',\vec{\upsilon}')\left[P_s(R,\zeta(\vec{\upsilon},\vec{\upsilon}'))\delta D'\right]\exp\left[-\frac{D-D'}{\cos(\zeta(\vec{\upsilon},\vec{z}))}\right] \qquad \text{(B.7)}$$

where $E_j^{\,2}(D,\vec{\upsilon})$ is the intensity of light arriving at a distance D in the direction of $\vec{\upsilon}$ after

undergoing exactly j scattering events and $\zeta(\vec{\upsilon},\vec{v})$ is the angle between $\vec{\upsilon}$ and $\vec{v}$. The

first factor in Eq. (B.7), $E_{j-1}^2(D',\vec{\upsilon}')$, is the intensity of light that has been scattered

exactly j-1 times before reaching the small slice δD in direction $\vec{\upsilon}'$. The second term in

Eq. (B.7), $\left[P_s(R,\zeta(\upsilon,\upsilon'))\delta D'\right]$, represents the probability that this inputted light is

scattered exactly once within the slice δD in the direction $\vec{\upsilon}$. The last term in Eq. (B.7),

$\exp\left[-(D-D'/\cos(\zeta(\vec{\upsilon},\vec{z}))\right]$, represents the attenuation of the emerging light as it

propagates unscattered through the remaining thickness of the turbid medium. Since we

are considering light that is highly forward directed, we can approximate $\vec{\upsilon}$ with θ_x and

θ_y, the angle between the z-axis and the x-z and y-z planes respectively and we may also

approximate the cosine term with unity. We may also fit $P_s(R,\theta)$ given by Eq. (B.6) to a

Gaussian function of size parameter $\gamma = \pi^2 R^2/\lambda^2$ to yield:

$$E_j^{\,2}(D,\theta_x,\theta_y) = \int_0^D \int_{-\infty}^{\infty} \int_{-\infty}^{\infty} E_{j-1}^2(D',\theta_x',\theta_y') \qquad \text{(B.8)}$$
$$\times \left[\frac{\gamma}{\pi} \exp\left(-\gamma\left[(\theta_x - \theta_x')^2 + (\theta_y - \theta_y')^2 \right] \right) \right]$$
$$\times \exp\left[-(D - D') \right] d\theta_x' d\theta_y' dD'$$

We may also approximate $E_{j-1}^2(D',\vec{v}')$ with a Gaussian function of size parameter,

$\alpha = 2.69 w^2/\lambda^2$ where w is the size of the beam at the input of the turbid medium and

obtain a solution by induction for the scattering intensity given by,

$$E_j^{\,2}(D,\theta_x,\theta_y) \approx E_{input}^2 \left(\frac{\gamma}{j\alpha + \gamma} \right) \left(\exp\left[-\left(\frac{\gamma\alpha}{j\alpha + \gamma} \right)(\theta_x^2 + \theta_y^2) \right] \right) \left(\frac{D^j}{j!} \exp(-D) \right) \qquad \text{(B.9)}$$

The scattering intensity given in Eq. (B.9) is only valid for light scattered a few times and

thus is confined to a cone in the forward direction. It's expected to yield a better fit to

experiments for small values of D, since these are dominated by E_j terms where j is small

and is expected to deviate upward from the experimental curves at larger D since it over

estimates the values of $E_j^{\,2}$ for large j.
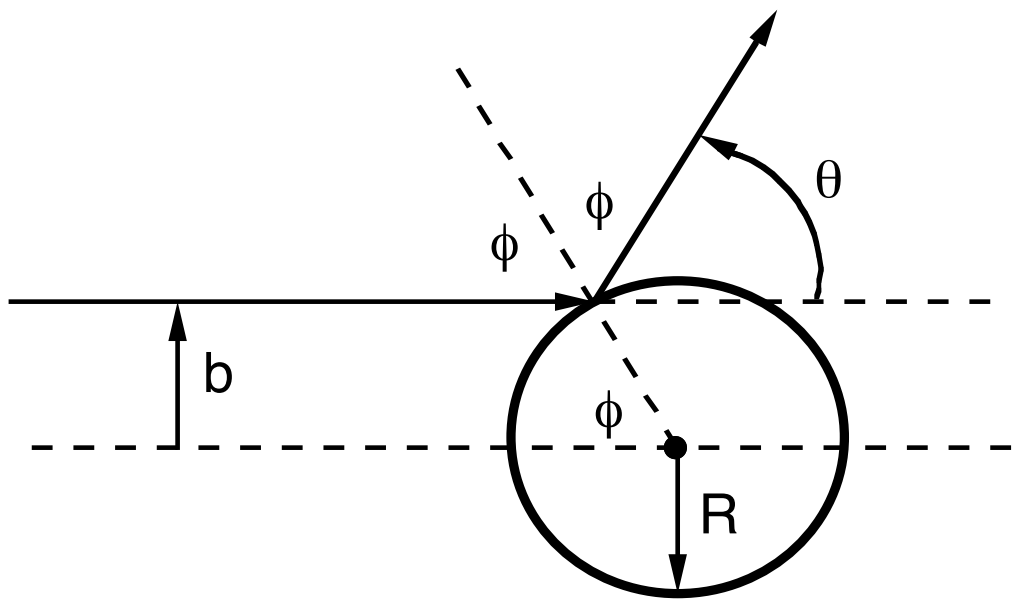
FIG. B.1   Scattering of light from a impenetrable sphere. Light is incident from the

left with an impact parameter b onto an impenetrable sphere of radius R. The incident

light is reflected at an angle ϕ with respect to the normal of the sphere surface and the

light is scattered at an angle θ with respect to the incident direction.
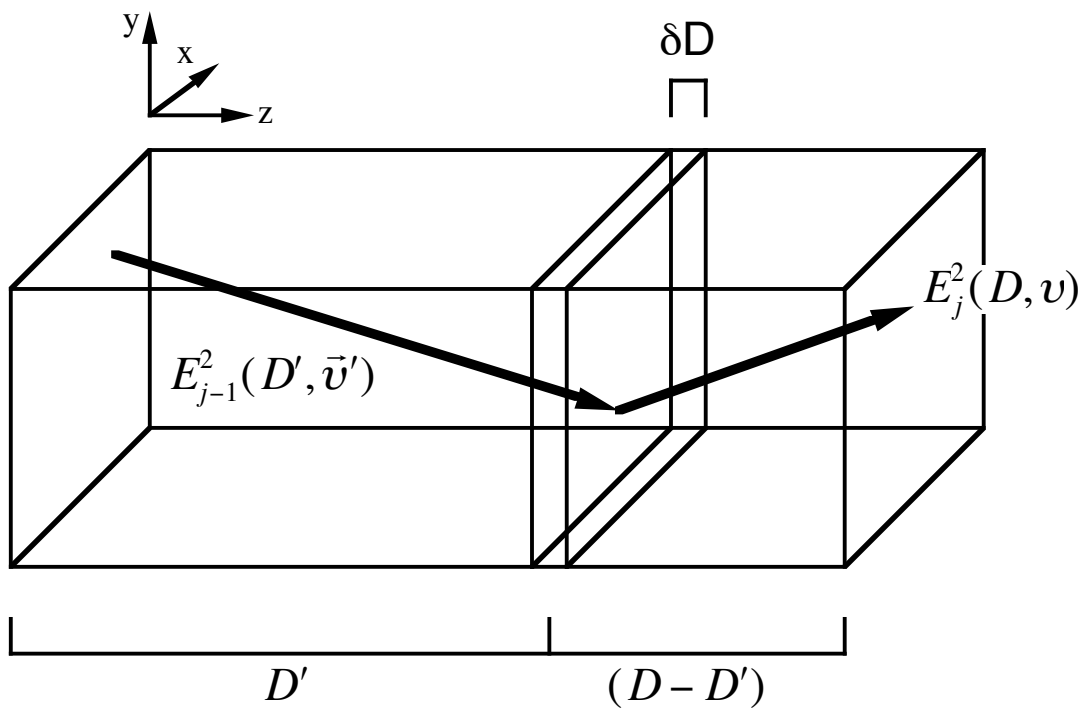
FIG. B.2   A schematic diagram of light scattering multiple times in a turbid medium of optical depth D. Light scattered exactly j-1 times into the $\vec{v}'$ direction after passing through an optical depth of D´ of the turbid media is scattered in the $\vec{v}$ direction, after passing through a slice of the turbid media   δD thick. The scattered light then exits after being attenuated by the remaining turbid medium of optical depth (D-D´).

Bibliography

[1]   L.M. Pismen, *Vortices in Nonlinear Field*s, Oxford Science Publications

(Clarendon Press, Oxford, 1999).

[2]   Sheldon Green eds., *Fluid Vortices*, (Kluwer Academic Publishers, Dordrecht,

Netherlands, 1995).

[3]   L. Davis, *Natural Disasters*, Facts on File Science Library (Facts on File, new

York 2002).

[4]   M. Vasnetsov and K. Staliunas, eds., *Optical Vortices*, vol. 228, Horizons in

World Physics, (Nova Science, Huntington, NY, 1999).

[5]   K.T. Gahagan and G.A. Swartzlander Jr., "Trapping of Low-index Microparticles

in an Optical Vortex," J. Opt. Soc. Am. B **15**, 524-534 (1998).

[6]   C.S. Buer, K.T. Gahagan, G.A. Swartzlander Jr., and P.J. Weathers, "Insertion of

Microscopic Objects Through Plant Cell Walls Using Laser Microsurgery,"

Biotechnology and Bioengineering **60**, 348-355(1998).

[7]   C.S. Buer, K.T. Gahagan, G.A. Swartzlander Jr., and P.J. Weathers, "Differences
        in optical trapping prompt investigations of Agrobacterium surface chacteristics,"
        Journal of Industrial Microbiology and Biotechnology **21**, 233-236 (1998).

[8]   A.W. Snyder, L. Poladian, and D. J. Mitchell, "Stable black self-guided beams of
        circular symmetry in a bulk Kerr medium," Opt. Lett. **17**, 789-791 (1992).

[9]   A. Berzanskis, A. Matijosius, A. Piskarkas, V. Smilgevicius, and A. Stabinis,
        "Conversion of topological charge of optical vortices in a parametric frequency
        converter," Opt. Comm. **140**, 273-276 (1997).

[10]   M.W. Beijersbergen, L. Allen, H.E.L.O. van der Veen, and J.P. Woerdman,
        "Astigmatic laser mode converters and transfer of orbital angular momentum,"
        Opt. Comm. **96**, 123-132 (1996).

[11]   V. Yu. Bazhenov, m.V. Vasnetsov, and M.S. Soskin, "Laser beams with screw
        dislocations in their wavefronts," Pis'ma Zh. Eksp. Teor. Fiz. **52**, 1037-1039
        (1990) [JETP Lett. **52**, 429-431 (1990)].

[12]   N.R. Heckenberg, R. McDuff, C.P. Smith, and A.G. White, "Generation of optical
        phase singularities by computer-generated holograms," Opt. Lett. **17**, 221-223
        (1992).

[13]   Z.S. Sacks, D. Rozas, and G.A. Swartzlander, Jr., "Holographic formation of

optical-vortex filaments," J.Opt. Soc. Am. B **15**, 2226-2234 (1998).

[14]   M.W. Beijersbergen, R.P.C. Coerwinkel, and J.P. Woerdman, "Helical-wavefront

laser beams produced by a spiral phase plate," Opt. Comm. **112**, 321-327 (1994).

[15]   F.B. Colstoun, G. Khitrova, A.V. Fedorov, T.R. Nelson, C. Lowery, T.M.

Brennan, B.G. Hammons, and P.D. Maker, "Transverse modes, vortices and

vertical-cavity surface-emitting lasers," Chaos, Solitons, & Fractals **4**, 1575-1596

(1995).

[16]   M.A.M. Van Hoek, "The spiral in British and Irish Neolithic rock art," Glasgow

Archeological Journal 18, 11-31 (1993).

[17]   Homer, *Chapman's Homer: The Odyssey*, (Princeton Press, Princeton 2000)

[18]   R.S. Scorer and L.J. Davenport, "Contrails and aircraft downwash," J. of Fluid

Mechanics **43**, 451-461 (1970).

[19]   T. Kambe, T. Takao, "Motion of distorted vortex rings," Journal of the Physical

Society of Japan **31**, 591 (1971).

[20]   M.L. White, "An asymmetrically rotating fluid disk with applications,"
        Astrophysics and Space Science **16**, 295-310 (1972).

[21]   A.G. Doroshkevich, "The origin of rotation of galaxies," Astrophys. Lett. **14**, 11-
        14 (1973).

[22]   S.I. Vainshtein and A.A. Ruzmaikin, "Relativistic vortex motion," Soviet
        Astronomy 17, 7-10 (1973) [S.I. Vainshtein and A.A. Ruzmaikin, "Relativistic
        vortex motion," Astronomicheskii Zhurnal **50**, 12-18 (1973)].

[23]   V.I. Korchagin and D. Ryabtsev, "Solitary vortices in galactic disk," Astrophysics
        and Space Science **126**, 1-7 (1986).

[24]   P.S. Wesson, "Vortex flow of matter around a singularity and a galactic
        hypothesis of Jeans," Astrophysics and Space Science **28**, 289-302 (1974).

[25]   F. Dowker, R. Gregory, and J. Traschen, "Euclidean black-hole vortices," Phys.
        Rev. D. **45**, 2762-2771 (1992).

[26]   P. Coullett, L. Gil, and F. Rocca, "Optical Vortices," Opt. Comm. 73, 403 (1989).

[27]   J.F. Nye and M. V. Berry, "Dislocations in wave trains," Proc. R. Soc. London
        Ser. A **336**, 165-190 (1974).

[28]   S. Ramo, J.R. Whinnery, and T. Van Duzer, *Fields and Waves in Communication
        Electronics*, (Wiley, New York, NY, 1965).

[29]   A.E. Siegman, *Lasers*, (University Science Books, Mill Valley, 1986).

[30]   E. Abramochkin and V. Volostnikov, "Spiral-Type Beams," Opt. Comm. **73**, 403
        (1989).

[31]   L.A. Lugiato, C. Oldano, and L.M. Narducci, "Cooperative frequency locking and
        stationary spatial structures in lasers," J. Opt. Soc. Am. B **5**, 879-888 (1988).

[32]   C. Tamm and C.O. Weiss, "Bistability and optical switching of spatial patterns in
        a laser," J. Opt. Soc. Am. B **7**, 1034-1038 (1990).

[33]   C.O. Weiss, C. Tamm, and P. Coullet, "Temporal and spatial laser instabilities,"
        J. Mod. Opt. **37**, 1825-1837 (1990).

[34]   M. Brambilla et al., "Transverse laser patterns. I. Phase singularity crystals,"
        Phys. Rev. A **43**, 5090-5113 (1991).

[35]   M. Brambilla et al., "Transverse laser patterns. I. Variational principle for pattern

        selection, spatial multistability and laser hydrodynamics," Phys. Rev. A **43**, 5114-

        5121 (1991).

[36]   M. Brambilla, G. Broggi, and F. Prati, "Spatiotemporal pattern formation and

        chaos in passive optical systems," Physica D **58**, 339-364 (1992).

[37]   M. Brambilla et al., "Dynamical transverse laser patterns. I. Theory," Phys. Rev.

        A **49**, 1427-1451 (1994).

[38]   M. Brambilla et al., "Dynamical transverse laser patterns. I. Experiment," Phys.

        Rev. A **49**, 1452-1467 (1994).

[39]   K. Staliunas and C.O. Weiss, "Nonstationary vortex lattices in large aperture class

        B lasers," J. Opt. Soc. Am. B **12**, 1142-1149 (1995).

[40]   J.W. Grantham, H.M. Gibbs, G. Khitrova, J.F. Valley, and X. Jianjin,

        "Kaleidoscopic Spatial Instability: Bifurcations of Optical Transverse Solitary

        Waves," Phys. Rev. Lett. **66**, 1422-1425 (1991).

[41]   G.L. Lippi, T. Ackemann, L.M. Hoffer, A. Gahl, and W. Lange, "Interplay of linear and nonlinear effects in the formation of optical vortices in a nonlinear resonator," Phys. Rev. A **48**, 4043-4046 (1993).

[42]   G. Indebetouw and D.R. Korwan, "Model of vortices nucleation in a photorefractive phase-conjugate resonator," J. Mod. Opt. **41**, 941-950 (1994).

[43]   G. Slekys, K. Staliunas, and C.O. Weiss, "Motion of phase singularities in a class-B laser," Opt. Comm. **119**, 433-446 (1995).

[44]   M. Vaupel and C.O. Weiss, "Circling optical vortices," Phys. Rev. A **51**, 4078-4085 (1995).

[45]   W.J. Firth and A. Lord, "Two-dimensional solitons in a Kerr cavity," J. Mod. Opt. **43**, 1071-1077 (1996).

[46]   N.R. Heckenberg, M. Vaupel, J.T. Malos, and C.O. Weiss, "Optical-vortex pair creation and annihilation and helical astigmatism of a nonplanar ring resonator," Phys. Rev. A **54**, 1-10 (1996).

[47]   D.Y. Tang, N.R. Heckenberg, and C.O. Weiss, "Phase dependent helical pattern formation in a laser," Opt. Comm. **114**, 95-100 (1995).

[48]   K. Staliunas, "Dynamics of optical vortices in a laser beam," Opt. Comm. **90**, 123-127 (1992).

[49]   K. Staliunas, "Optical vortices during three-way nonlinear coupling," Opt. Comm. **91**, 82-86 (1992).

[50]   C.O. Weiss, H.R. Telle, and K. Staliunas, "Restless optical vortex," Phys. Rev. A **47**, 1616-1619 (1993).

[51]   V.B. Taranenko, K. Staliunas, and C.O. Weiss, "Spatial soliton laser: Localized structures in a laser with a saturable absorber in a self-imaging resonator," Phys. Rev. A **56**, 1582-1591 (1997).

[52]   M.V. Berry, "Singularities in Waves and Rays," in Physics of defects, Les Houches Sessions XXXV, R. Balian, M. Kleman, and J.P Poirier, eds., (North Holland, Amsterdam, 1981), pp. 453-543.

[53]   J. Masajada and B. Dubik, "Optical vortex generation by three plane wave interference," Opt. Comm. **198**, 21-27 (2001).

[54]   N.B. Baranova, B. Ya. Zel'dovich, A.V. Mamaev, N.F. Pilipetski, and V.V. Shkunov, "Dislocations of the wavefront of a speckle-inhomogeneous field

(theory and experiment)," Pis'ma Zh. Eksp. Teor. Fiz., **33**, 206 (1981) [JETP Lett., **33**, 195 (1981)].

[55]   K. Staliunas, A. Berrzanskis, and V. Jarutis, "Vortex statistics in optical speckle fields," Opt. Comm. **120**, 23-28 (1995).

[56]   N.B. Baranova, A.V. Mamaev, N.F. Pilipetski, V.V. Shkunov, and B. Ya. Zel'dovich, "Wave-front dislocations:topological limitations for adaptive systems with phase conjugation," J. Opt. Soc. Am. **73**, 525-528 (1983).

[57]   I. Freund, N. Shvartsman, and V. Freilikher, "Optical Dislocation networks in highly random media," Opt. Comm. **101**, 247-264 (1993).

[58]   I. Freund, "Optical vortices in Gaussian random wave fields: statistical probability densities.," J. Opt. Soc. Am. A **11**, 1644-1652 (1994).

[59]   N. Shvartsman and I. Freund, "Vortices in Random Wave Fields: Nearest Neighbor Anticorrelations," Phys. Rev. Lett. **72**, 1008-1011 (1994).

[60]   I. Freund and N. Shvartsman, "Wave-field singularities: The sign principle," Phys. Rev. A **50**, 5164-5172 (1994).

[61]   N. Shvartsman and I. Freund, "Wave-field phase singularities: near-neighbor

corelations and anticorrelations," J. Opt. Soc. Am. A **11**, 2710-2718 (1994).

[62]   N. Shvartsman and I. Freund, "Speckle spots ride phase saddles sidesaddle," Opt.

Comm. **117**, 228-234 (1995).

[63]   I. Freund and N. Shvartsman, "Structural correlations in Gaussian random wave

fields," Phys. Rev. E **51**, 3770-3773 (1995).

[64]   I. Freund, "saddle, singularities, and extrema in random phase fields," Phys. Rev.

E **52**, 2348-2360 (1995).

[65]   I. Freund, "Intensity critical point correlation functions in random wave fields,"

Opt. Comm. **128**, 315-324 (1996).

[66]   I. Dana and I. Freund, "Vortex-lattice wave fields," Opt. Comm. **136**, 93-113

(1997).

[67]   I. Freund, "Critical-point level-crossing geometry in random wave fields," J. Opt.

Soc. Am. A **14**, 1911-1927 (1997).

[68]   I. Freund and M. Wilkinson, "Critical-point screening in random wave fields," H. Opt. Soc. A **15**, 2892-2902 (1998).

[69]   I. Freund, "Critical point explosions in two-dimensional wave fields," Opt. Comm. **159**, 99-117 (1999).

[70]   I. Freund and D.A. Kessler, "Critical point trajectory bundles in singular wave fields," Opt. Comm. **187**, 71-90 (2001).

[71]   T. Ackemann, E. Kriege, and W. Lange, "Phase singularities via nonlinear beam propagation in Sodium vapor," Opt. Comm. **115**, 339-346 (1995).

[72]   A.V. Ilyenkov, A.I. Khizhnyak, L.V. Kreminskaya, M.S. Soskin, and M.V. Vasnetsov, "Birth and evolution of wave-front dislocations in a laser beam passed through a photorefractive $LiNbo_3$:Fe crystal," Appl. Phys.B **62**, 465-471 (1996).

[73]   A.V. Ilyenkov, L.V. Kreminskaya, M.S. Soskin, and M.V. Vasnetsov, "Birth, evolution, and annihilation of phase singularities in the propagation of a laser beam passed through a self-focusing Strontium Barium Niobate crystal," Journal of Nonlinear Optical Physics and Materials **6**, 169-180 (1997).

[74]   L.V. Kreminskaya, M.S. Soskin, and A.I. Khizhnyak, "Gaussian lenses give birth
        to optical vortices in laser beams," Opt. Comm. **145**, 377-384 (1998).

[75]   L.V. Kreminskaya, M.S. Soskin, and A.I. Khizhnyak, "Gaussian lenses initiate
        optical vortices in laser beams during self-action in Kerr-like medium," Chaos,
        Solitons, & Fractals **10**, 737-744 (1999).

[76]   J.F. Nye, *Natural Focusing of Light*, (Institute of Physics Publishing, Bristol Uk
        and Philadelphia, U.S.A., 1999)

[77]   A.M. Deykoon, M.S. Soskin, and G.A. Swartzlander, "Nonlinear optical
        catastrophe from a smooth initial beam," Opt. Lett. **24**, 1224-1226 (1999).

[78]   G.A. Swartzlander Jr. and C.T. Law, "Optical Vortex Solitons Observed in Kerr
        Nonlinear Media," Phys. Rev. Lett. 69, 2503-2506 (1992).

[79]   C.T. Law and G.A. Swartzlander Jr., "Optical vortex solitons and the stability of
        dark soliton stripes," Opt. Lett. 18, 586-588 (1993).

[80]   A.V. Mamaev, M. Saffman, D.Z. Anderson, and A.A. Zozulya, "Propagation of
        light beams in anisotropic nonlinear media: From symmetry breaking to spatial
        turbulence," Phys. Rev. A 54 970-879 (1996).

[81]   A.V. Mamaev, M. Saffman, and A.A. Zozulya, "Propagation of Dark Strip Beams in Nonlinear Media: Snake Instability and Creation of Optical Vortices," Phys. Rev. Lett. 76, 2262-2265 (1996).

[82]   V. Tikhonenko, J. Christou, B. Luther-Davies, and Y.S. Kivshar, "Observation of vortex solitons created by the instability of dark soliton stripes," Opt. LEtt. 21, 1129-1131 (1996).

[83]   B. Luther-Davies, J. Christou, V. Tikhonenko, and Y.S. Kivshar, "Optical vortex solitons: experiment versus theory," J. Opt. Soc. Am. B 14, 3045-3053 (1997).

[84]   Yijiang-Chen and J. Atai, "Dynamics of optical-vortex solitons in perturbed nonlinear media," J. opt. Soc. Am. B 11, 2000-2003 (1994).

[85]   C.T. Law and G.A. Swartzlander Jr., "Polarized optical vortex solitons: instabilities and dynamics in Kerr nonlinear media," Chaos, Solitons, & Fractals 4, 1759-1766 (1994).

[86]   B. Luther-Davies, R. Powles, and V. Tikhonenko, "Nonlinear rotation of three-dimensional dark spatial solitons in a Gaussian laser beam," Opt. Lett. 19, 1816-1818 (1994).

[87]   Y.S. Kivshar and Xiaoping-Yang, "Dynamics of dark solitons," Chaos, Solitons, & Fractals 4, 1745-1758 (1994).

[88]   V. Tikhonenko, J. Christou, B. Luther-Davies, "Spiraling bright spatial solitons formed by the breakup of an optical vortex in a saturable self-focusing medium," J. Opt. Soc. Am. B 12, 2046-2052 (1995).

[89]   I. Velchev, A. Dreischuh, D. Neshev, S. Dinev, "Interactions of optical vortex solitons superimposed on different background beams," Opt. Comm. 130, 385-392 (1996).

[90]   J. Christou, V. Tikhonenko, Y.S. Kivshar, B. Luther-Davies, "Vortex soliton motion and steering," Opt. Lett. 21, 1649-1651 (1996).

[91]   Zhigang-Chen, M. Segev, D.W. Wilson, R.E. Muller, and P.D. Maker, "Self-trapping of an optical vortex by use of the bulk photovoltaic effect," Phys. Rev. Lett. 78, 2948-2951 (1997).

[92]   A.V. Mamaev, M. Saffman, A.A. Zozulya, "Time-dependent evolution of an optical vortex in photorefractive media," Phys. Rev. A 56, 1713-1716 (1997).

[93]   J. Herrmann, "Bistable dark soliton solutions in dispersive media with a linear and quadratic intensity-dependent refraction index change," Opt. Comm. 91, 337-340 (1992).

[94]   A.V. Buryak and Y.S. Kivshar, "Twin-hole dark solitons," Phys. Rev. A 51, 41-44 (1995).

[95]   G.A. Swartzlander Jr. et al., "Optical transistor effect using an optical vortex soliton," Laser-Physics 5, 704-709 (1995).

[96]   L.G. Gouy, "Sur une propriete nouvelle des ondes luminineuses," Compt. Rend. Acad. Sci. Paris **110**, 1251-1253 (1890).

[97]   L.G. Gouy, "Sur la propagation anomale des ondes," Ann. Chim. Phys. Ser. 6 **24**, 145-213 (1891).

[98]   F.S. Roux, "Dynamical behavior of optical vortices," J. Opt. Soc. Am. B **12**, 1215-1221 (1995).

[99]   D. Rozas, C.T. Law, and G.A. Swartzlander Jr., "Propagation dynamics of optical vortices," J. Opt. Soc. Am. B 14, 3054-3065 (1997).

[100]   I.V. Basistiy, V. Y. Bazhenov, M.S. Soskin, and M.V. Vasnetsov, "Optics of light beams with screw dislocations," Opt. Comm. 103, 422-328 (1993).

[101]   G. Idebetouw, "Optical vortices and their propagation," J. Mod. Opt. **40**, 73-87 (1993).

[102]   A.V. Volyar, T.A. Fadeeva, and S.N. Lapaeva, "the birth, annihilation, and evolution of nonparaxial optical vortices: 2. Topological dipole," Tech. Phys. Lett. **27**, 945-948 (2001).

[103]   A.V. Volyar and T.A. Fadeeva, "Dynamics of topological multipoles: II. Creation, annihilation, and evolution of nonparaxial optical vortices," Optics and Spectroscopy **92**, 253-262 (2002).

[104]   F.S. Roux, "Paraxial modal analysis technique for optical vortex trajectories," J. Opt. Soc. Am. B **20**, 1575-1580 (2003).

[105]   Guang-Hoon-Kim et al., "An array of phase singularities in a self-defocusing medium," Opt. Comm. **147**, 131-137 (1998).

[106]   M.D. Levenson et al. "Optical vortex masks for via levels," J. of Microlithography, Microfabrication, and Microsystems **3**, 293-304 (2004).

[107] D. Rozas, Z.S. Sacks, and G.A. Swartzlander Jr., "Experimental Observation of Fluidlike Motion of Optical Vortices," Phys. Rev. Lett. **79**, 3399-3402 (1997).

[108] D. Rozas and G.A. Swartzlander Jr., "Observed rotational enhancement of nonlinear optical vortices," Opt. Lett. **25**, 126-128 (2000).

[109] L. Allen, M.W. Beijersbergen, R.J.C. Spreeuw, and J.P. Woerdman, "Orbital angular momentum and the transformation of Laguerre-Gaussian modes," Phys. Rev. A **45**, 8185-8189 (1992).

[110] M. Padgett, J. Courtial, and L. Allen, "Light's Orbital Angular Momentum," Physics Today, 35-40 (May 2004).

[111] K. Dholokia et al. "Second-harmonic generation and the orbital angular momentum of light," Phys. Rev. A **54**, 3742-3745 (1996).

[112] A.Y. Bekshaev, M.S. Soskin, M.V. Vasnetsov, "Optical vortex symmetry breakdown and decomposition of the orbital angular momentum of light beams," J. Opt. Soc. Am. A **20**, 1635-1643 (2003).

[113] C.T. law, X. Zhang, and G.A. Swartzlander Jr., "Waveguiding properties of optical vortex solitons," Opt. Lett. 25, 55-57 (2000).

[114] K.T. Gahagan and G.A. Swartzlander Jr., "Optical Vortex Trapping of Particles,"

       Opt. Lett. 21, 827-829 (1996).

[115] K. Dholakia, J. Soneson, E.M. Wright, "Optical dipole traps and atomic

       waveguides based on Bessel light beams," Phys. Rev. A 63, art. # 063602 (2001).

[116] S.A. Tatarkova, A.E. Carruthers, K. Dholakia, "One-dimensional optically bound

       arrays of microscopic particles," Phys. Rev. Lett. 89, art. # 283901 (2002).

[117] G. Molina-Terriza, J. Recolons, L. Torner, "The curious arithmetic of optical

       vortices," Opt. Lett. 25, 1135-1137 (2000).

[118] I.D. Maleev and G.A. Swartzlander Jr., "Composite optical vortices," J. Opt. Soc.

       Am. B 20, 1169-1176 (2003).

[119] M. Born and E. Wolf, *Principles of Optics-corrected 7th ed.*, (Cambridge

       University Press, Cambridge, UK, 2002).

[120] R. Simon and G.S. Agarwal, "Wigner representation of Laguerre-Gaussian

       beams," Opt. Lett. 25, 1313-1315 (2000).

[121] S.A. Ponomarenko, "A class of partially coherent beams carrying optical

       vortices," J. Opt. Soc. Am. A **18**, 150-156 (2001).

[122] F. Gori et al., "Partially coherent sources with helicoidal modes," J. Mod. Opt.

       45, 539-554 (1998).

[123] S.R. Seshardri, "Partially coherent Gaussian Schell-model electromagnetic

       beams," opt. Soc. Am. A 16, 1373-1380 (1999).

[124] R. Simon and N. Mukunda, "Twisted Gaussian Schell-model beams," J. Opt. Soc.

       Am. A 10, 95-109 (1993).

[125] Z. Bouchal and J. Perina, "Non-diffracting beams with controlled spatial

       coherence," J. of Mod. Opt. **49**, 1673-1689 (2002).

[126] S.R. Seshadri, "Average characteristics of a partially coherent Bessel-Gauss

       optical beam," J. Opt. Soc. Am. A 16, 2917-2927 (1999).

[127] F. Gori, G. Guattari, and C. Padovani, "Modal expansion for j_0-correlated Schell-

       model sources," Opt. Comm. 64, 311-316 (1987).

[128]   G.V. Bogatyryova, et al., "Partially coherent vortex beams with a separable

        phase," Opt. Lett. **28**, 878-880 (2003).

[129]   B.J. Thompson and E. Wolf, J. Opt. Soc. Am. **47**, 895 (1957).

[130]   D. Palacios, I.M. Maleev, A.S. Marathay, and G.A. Swartzlander Jr., "Spatial

        Correlation Singularity of a Vortex Field," Phys. Rev. Lett. **92**, art. # 143905

        (2004).

[131]   G. Gbur and T.D. Visser, "Coherence vortices in partially coherent beams," Opt.

        Comm. **222**, 117 (2003).

[132]   H.F. Schouten, et al., "Phase singularities of the coherence functions in Young's

        interference pattern," Opt. Lett. **28**, 968-970 (2003).

[133]   I.M. Maleev, D.M Palacios, A.S. Marathay, and G.A. Swartzlander Jr., "Spatial

        Correlation Vortices: Theory", submitted to J. Opt. Soc. B.

[134]   I.M. Maleev, D.M Palacios, A.S. Marathay, and G.A. Swartzlander Jr., "Spatial

        Correlation Vortices: Detection", to be submitted to Opt. Lett.

[135]   I.M. Maleev, D.M Palacios, and G.A. Swartzlander Jr., "Spatial Correlation Vortices: propagation", to be submitted to Opt. Comm.

[136]   T.D. Visser, Gbur, E. Wolf, "Effect of the state of coherence on the three-dimensional spectral intensity distribution near focus," Opt. Comm. 213, 13-19 (2002).

[137]   G. Gbur, T.D. Visser, and E. Wolf, "Anomalous Behavior of Spectra near Phase Singularities of Focused Waves," Phys. Rev. Lett. 88, art. # 013901 (2002).

[138]   G. Popescu and A. Dogariu, "Spectral anomlies at wave-front dislocations," Phys. Rev. Lett. 88, art. # 183902 (2002).

[139]   G.A. Swartzlander Jr. and J. Schmidt, "Temporal Correlation Vortices and Topological Dispersion," submitted to Phys. Rev. Lett.

[140]   G.A. Swartzlander Jr., "Peering into darkness with a vortex spatial filter," Opt. Lett. **26**, 497 (2001).

[141]   David Palacios, David Rozas, and Grover A. Swartzlander Jr., "Observed Scattering into a Dark Optical Vortex Core," Phys. Rev. Lett. **88**, art. # 103902 (2002).

[142] I. Freund and V. Freilikher, "Parameterization of anisotropic vortices," J. Opt. Soc. Am. A 14, 1902-1910 (1997).

[143] I. Freund, "Vortex derivatives," Opt. Comm. 137, 118-126 (1997).

[144] J. Goodman, *Introduction to Fourier Optics 2nd ed.*, (McGraw Hill, U.S.A, 1996)

[145] P.A. Lynn and W. Fuerst, *Introductory Digital Signal Processing with Computer Applications 2nd ed.*, (John Wiley & Sons, UK, 1989).

[146] C. Gorecki, "Interferometric analysis using a Fourier transform method for automatic 3D surface measurement," Pure Appl. Opt. **1**, 103-110 (1992).

[147] The diffractive optical foundry was sponsored by DARPA in 1995-1996, in cooperation with Honeywell International, Inc. and George Mason University.

[148] J.R.P. Angel and N.J. Woolf, "An Image Nulling Interferometer to study Extrasolar Planets", The Astrophysical Journal, vol. 475, pp. 373-377, (1997).

[149] A.S. Marathay, *Elements of Optical Coherence Theory*, (Wiley and Son, New York, 1982).

[150]   J.W. Goodman, *Statistical Optics*, (John Wiley and Sons, New York, 1985).

[151]   L. Mertz, *Transformations in Optics*, (Wiley, New York, 1965).

[152]   A. Ishimaru, *Wave Propagation in Random Media*, the IEEE/OUP series on electromagnetic wave theory, (Academic Press, New York, NY, 1978).

[153]   Changhuei Yang et al., "Spatial coherence of forward-scattered light in a turbid medium, " J.Opt. Soc. Am. A, **16**, 866-871 (1999).

[154]   W. Grandy Jr., *Scattering of Waves from Large Spheres*, (Cambridge University Press, UK, 2000).

[155]   M.Z. Hanson, Applied Optics, **19**, 3441 (1980).

[156]   Joseph H. Koo and E. Dan Hirleman, Applied Optics, **31**, 2130 (1992).

[157]   L.G. Kazovsky and N.S. Kopeika, Applied Optics, **22**, 706 (1983).

[158]   D. Murphy, "Fundamentals of Light Microscopy and Electronic Imaging", (Wily-Liss, New York, 2001).

[159]   L. Mertz, "Excursions in Astronomical Optics", (Springer, New York, 1996).

[160]   R.A. Showengerdt, "Remote Sensing: Models and Methods for Image Processing", (Academic Press, 1997).

[161]   F. Yu, *Optical Pattern Recognition*, (Cambridge University Press, Cambridge, UK; New York, NY, USA, 1998).

[162]   Z. Zalersky, *Optical Superresolution*, (Springer, Tel Aviv; New York, 2004).

[163]   Beran, M.J. and G.B. Parrent, Jr. *Theory of Partial Coherence*, (Prentice-Hall, Englewood Cliffs, NJ, 1964).

Curriculum Vitae

David M. Palacios

office: (818) 393-1158

email: David.M.Palacios@jpl.nasa.gov

Objective   To secure a research and development position in either the field of

biomedical imaging, remote sensing, or a related advanced imaging field.

Education

June '04   University of Arizona, Optical Sciences Dept., Tucson, AZ

PhD Dissertation

May '01   Worcester Polytechnic Institute, Worcester, MA

Physics PhD Program

May '97   Florida Institute of Technology, Melbourne, FL

Awarded Bachelors of Science Degree in Physics (GPA 3.31)

Dissertation

An Optical Vortex Coherence Filter

Advisor: Grover A. Swartzlander Jr.

Research Interests

Optical coherence theory, phase measurement, phase retrieval, image reconstruction, low coherence imaging techniques, singular optics, remote sensing, diffractive optics, adaptive optics, nulling interferometry, optical tomography

Research Experience

Research Associate, The University of Arizona, Tucson, AZ, 6/01-present

∞ Simulated light beams containing phase defects in coherent and partially coherent systems using C++. Simulations included near-field and far-field propagation of both the field and the mutual coherence function.

∞ Constructed and used a novel wavefront-folding interferometer to measure the phase of various correlation functions for partially coherent systems. This technique is useful for phase retrieval in low coherence systems

∞ Made spectral measurements of light beams transmitted through a diffractive optical element.

∞ Programmed analysis software in C++ and Matlab.

GAAN Fellow, Worcester Polytechnic Institute, Worcester, MA, 6/99-5/01

∞ Designed and constructed a novel scatterometer using a coherence filtering technique based on a vortex diffractive mask.

∞ Measured low-angle forward scattered light with a vortex coherence filter

∞ Used an optical vortex coherence filter to image a low light level secondary source located near a brighter primary source. Thereby defeating the resolution limit.

∞ As a GAAN fellow I also continued as a teaching assistant for one term a year.

Research Assistant, Worcester Polytechnic Institute, Worcester, MA, 1/98-5/99

∞ Performed optical limiting experiments using a nonlinear liquid cell with a vortex phase mask interface.

∞ Responsible for acquisition of nonlinear liquids and maintenance of safety protocols.

∞ Reconstructed the phase map produced by a vortex diffractive optic by the method of Fourier fringe pattern analysis.

Teaching Experience

Teaching Assistant, Worcester Polytechnic Institute, Worcester, MA, 8/97-5/99

∞ Teaching Assistant duties included leading lab discussion, advising laboratory

   experiments, grading, maintaining regular office hours, and proctoring exams.

∞ Assisted with the Introductory Astronomy Course

∞ Taught the Modern Physics Lab,

∞ Taught the Electricity and Magnetism Lab

∞ Taught the Mechanics Lab

Lab Mentor, Worcester Polytechnic Institute, Worcester, MA, 5/99-12/99

∞ Mentored an undergraduate student with his senior thesis

∞ The thesis topic was on the optical trapping of micro-spheres by a diffracting

   aperture.

∞ Mentoring duties included: overseeing lab research, instructing the student in

   optics lab skills, aided in the design of the experiment and aided the student in

   data analysis.

Other Relevant Experience

∞ Aided in the construction of the Optical Vortex Laboratory at OSC. Duties

   included, purchasing of equipment, optical equipment installation, and

   interfacing with contractors. I designed the lab layout and performed a cost

   analysis for installation. I worked with contractors to install overhead

shelving, wall-mounted cabinets, computer tables, and optical tables. I also worked with the University of Arizona Plant Services to install electrical power and water for an Ion Argon laser and an NdYag laser.

∞   Certified in Laser Safety from the University of Arizona.

∞   Certified in Machine Shop Safety from the University Research Instrumentation Center.

Publications and Patents

Optical Vortex Spatial Filter for Coherent and Incoherent Detection of Electromagnetic Radiation, by Grover A. Swartzlander Jr. and David Palacios, provisional patent application submitted on April 12, 2002.

Observed Scattering into a Dark Optical Vortex Core, by David Palacios, David Rozas, and Grover A. Swartzlander Jr., Phys. Rev. Lett., vol. 88, #10, article # 103902 (2002).

Spatial Correlation Singularity of a Vortex Field, by D.M. Palacios, I.M. Maleev, A.S. Marathay, and G.A. Swartzlander Jr., accepted to Physical Review Letters 2/20/04

Spatial Correlation Vortices: Theory, by I.D. Maleev, D.M. Palacios, A.S. Marathay, and G.A. Swartzlander Jr., submitted to Journal of the Optical Society of America B 2/20/04.

An Achromatic Null in the Presence of Fractional Vortices, by D.M. Palacios and G.A. Swartzlander Jr., to be submitted to Journal of the Optical Society of America B.

Presentations

" Optical Vortices in Low Coherence Light" presented at:

The Optical Society of America Annual Meeting (October 2003)

" White Light Optical Vortices" presented at:

The Optical Society of America Annual Meeting (October 2002)

" Optical Vortex DOE- Scattering Application" presented at:

The Diffractive Optics and Micro-Optics Topical Meeting (June 2002)

" Scattering into Darkness" presented at:

The OSC Industrial Affiliates Workshop (February 2002)

" Optical Vortex Detection of Forward-Scattered Light" presented at:

The Optical Society of America Annual Meeting (October 2001)

" An Optical Vortex Spatial Filter" presented at:

Conference on Lasers and Electro-Optics (May 2001)

Honors and Awards

GAAN Fellow

Member of The Optical Society of America

Member of The American Physical Society

Senior Year award for excellence in physics

1997 Sigma Xi research paper competition- 1st place (unpublished papers)

Sigma Pi Sigma member (Physics Honor Society)

Selected Advanced Courses

Classical Electrodynamics   Optical Coherence Theory   Fourier Optics

Scattering Theory   Singular Optics   Nonlinear Optics